



저작자표시-비영리-동일조건변경허락 2.0 대한민국

이용자는 아래의 조건을 따르는 경우에 한하여 자유롭게

- 이 저작물을 복제, 배포, 전송, 전시, 공연 및 방송할 수 있습니다.
- 이차적 저작물을 작성할 수 있습니다.

다음과 같은 조건을 따라야 합니다:



저작자표시. 귀하는 원저작자를 표시하여야 합니다.



비영리. 귀하는 이 저작물을 영리 목적으로 이용할 수 없습니다.



동일조건변경허락. 귀하가 이 저작물을 개작, 변형 또는 가공했을 경우에는, 이 저작물과 동일한 이용허락조건하에서만 배포할 수 있습니다.

- 귀하는, 이 저작물의 재이용이나 배포의 경우, 이 저작물에 적용된 이용허락조건을 명확하게 나타내어야 합니다.
- 저작권자로부터 별도의 허가를 받으면 이러한 조건들은 적용되지 않습니다.

저작권법에 따른 이용자의 권리는 위의 내용에 의하여 영향을 받지 않습니다.

이것은 [이용허락규약\(Legal Code\)](#)을 이해하기 쉽게 요약한 것입니다.

[Disclaimer](#)

이학박사 학위논문

Synthesis of 2D Materials by
Chemical Vapor Deposition for
Smart Applications

화학기상증착법을 이용한 2차원 물질 합성과
스마트 응용

2018 년 02 월

서울대학교 대학원

화학부 물리화학 전공

강 상 민

화학기상증착법을 이용한 2차원 물질 합성과

스마트 응용

Synthesis of 2D Materials by Chemical Vapor Deposition for
Smart Applications

지도 교수 홍 병 희

이 논문을 이학박사 학위논문으로 제출함

2018 년 02 월

서울대학교 대학원

화학부 물리화학전공

강 상 민

강상민의 이학박사 학위논문을 인준함

2018 년 02 월

위 원 장 _____ 장두전 (인)

부위원장 _____ 홍병희 (인)

위 원 _____ 이정호 (인)

위 원 _____ 조성표 (인)

위 원 _____ 박중보 (인)

A Ph.D. Dissertation

Synthesis of 2D Materials by Chemical Vapor
Deposition for Smart Applications

Supervisor : Professor Byung Hee Hong

Major : Physical Chemistry

By Sangmin Kang

Department of Chemistry

Graduate School of Seoul National University

2018. 02

Abstract

Synthesis of 2D Materials by Chemical Vapor Deposition for Smart Applications

Sangmin Kang
Department of Chemistry
The Graduate School Seoul National University

Two-dimensional (2D) materials, which exist in layered structure, have been explosively researched over the last few years since graphene was firstly mechanically exfoliated. Although mechanical exfoliation provides high quality 2D materials, their micro-scale crystals limit their practical applications. Chemical vapor deposition (CVD) provides an answer for the scalable and reliable production. Currently the growth and development of the CVD based synthesis methods are the basis for industrial application of 2D materials. Among these practical applications, 2D materials show promising prospect in fields of electromagnetic interference (EMI) shielding and electrochemical catalysts because of their ultra-thin thickness and large surface area. Many world-wide groups have published reports on the synthesis of CVD based 2D materials for EMI shielding and electrochemical applications. We also summarize our experimental results related to these new materials and future applications.

First, we demonstrate heat generation originated from the

unique electromagnetic (EM) wave absorption synthesized by low pressure chemical vapor deposition (LPCVD). The EM wave induces an oscillating magnetic moment generated by the orbital motion of moving electrons, which efficiently absorbs the EM energy and dissipate it as a thermal energy. In this case, the mobility of electron is more important than the conductivity, because the EM-induced diamagnetic moment is directly proportional to the speed of electron in an orbital motion. We expect that the efficient and fast heating of graphene films by EM waves can be utilized for smart heating windows and defogging windshields.

In addition, we report the graphene based highly conducting contact lens platform that reduces the exposure to EM waves and dehydration. The EM wave shielding function of the graphene-coated contact lens was tested on egg whites exposed to strong EM waves inside a microwave oven. We also demonstrated the enhanced dehydration protection effects of the graphene-coated lens by monitoring the change in water evaporation rate from the vial capped with the contact lens. Thus, we believe that the graphene-coated contact lens would provide a healthcare and bionic platform for wearable technologies in the future.

Second, we focus on the electrochemical application of beyond graphene materials. We devise a simple strategy to use conventional laser printer toner materials as precursors

for graphitic carbon electrodes. The toner was laser-printed on metal foils, followed by thermal annealing in hydrogen environment, finally resulting in the patterned thin graphene-graphitic carbon electrodes for supercapacitors. The electrochemical cells made of the graphene-graphitic carbon electrodes show remarkable higher energy and power performance compared to conventional supercapacitors.

Finally, we demonstrate that metal organic chemical vapor deposition (MOCVD) and UV-ozone treatment on bilayer MoS₂ could introduce more active sites and increased conductivity via the small grain size and oxygen doping, leading to a high density of exposed edges and a significant improvement of the hydrogen evolution activity. The mechanisms of increased electrochemical hydrogen evolutions are explained by enhanced photoluminescence (PL) and extended exciton life times. Our approach can be used directly to increase the hydrogen production activity in electrochemical reaction of 2D materials, and help to understand the catalytic effects and mechanisms of 2D materials.

Keyword : low pressure chemical vapor deposition (LPCVD), metal organic chemical vapor deposition (MOCVD), graphene, MoS₂, electromagnetic interference (EMI), electrochemistry.

Student Number : 2014-21229

Table of Contents

Abstract	1
Contents	4
List of Figures	7
List of Tables	25
Chapter 1. Introduction.....	26
1.1. Classification of 2D materials synthesis methods	
1.1.1. Mechanical exfoliation	
1.1.2. Liquid exfoliation	
1.1.3. Chemical vapor deposition (CVD)	
1.2. EMI shielding properties of 2D materials	
1.3. Electrochemical properties of 2D materials	
1.4. References	
Chapter 2. EMI shielding application of graphene.....	46
2.1. Efficient heat generation in large-area graphene films by electromagnetic wave absorption	
2.1.1. Introduction	
2.1.2. Experimental	

2.1.3. Results and discussion

2.1.4. Conclusions

2.1.5. References

2.2. Smart contact lenses with graphene coating for EMI shielding and dehydration protection

2.2.1. Introduction

2.2.2. Experimental

2.2.3. Results and discussion

2.2.4. Conclusions

2.2.5. References

Chapter 3. Electrochemical application of graphene and beyond graphene materials..... 100

3.1. Roll-to-roll laser-printed graphene-graphitic carbon electrodes for high performance supercapacitors

3.1.1. Introduction

3.1.2. Experimental

3.1.3. Results and discussion

3.1.4. Conclusions

3.1.5. References

3.2. UV-ozone engineered MoS₂ synthesized by MOCVD for improved hydrogen evolution

3.2.1. Introduction

3.2.2. Experimental

3.2.3. Results and discussion

3.2.4. Conclusions

3.2.5. References

Abstract in Korean.....172

Appendix175

Acknowledgement.....177

List of Figures

Figure 1. An illustrative procedure of the mechanical exfoliation.

Single-layer graphene is exfoliated from HOPG using commercial Scotch tape technique.35

Figure 2. Schematic illustration of the main liquid exfoliation mechanisms. (a) Ion intercalation. Ions are intercalated

between the layers in liquid environment and their agitations could separate the layers, (b) Ion exchange. Some layered compounds contain ions, which can be exchanged in a liquid environment for other. Then, their agitation provides an exfoliated dispersion. (C) Sonication assisted exfoliation. The layered crystal is sonicated in a solvent, resulting in exfoliation and formation of nanosheets.36

Figure 3. Large-area synthesis of high-quality and uniform graphene films on copper foils using LPCVD. (a,b) SEM image

of graphene on a copper foil synthesized by LPCVD (c,d) Using conventional wet transfer, graphene films transferred onto a SiO₂/Si substrate and a glass plate, respectively.37

Figure 4. Wafer-scale synthesis of high-quality and uniform TMDC films synthesized by MOCVD. (a,b) Photographs of monolayer MoS₂ and WS₂, respectively. (c) Photograph of patterned single-layer MoS₂ film on a 4-inch SiO₂/Si wafer. (d) Optical absorption spectra of monolayer MoS₂ (red line) and WS₂ (orange line) films. (e,f) Raman and photoluminescence (PL) spectra of monolayer MoS₂ (red line) and WS₂ (orange line) films. (g) Scanning electron microscopy (SEM) and PL image of monolayer MoS₂. (h,i) Optical images of MoS₂ and WS₂, respectively. The inset show PL images at 1.9 eV. All scale bar in above images is 10 μm38

Figure 5. Proposed EMI shielding mechanisms of 2D materials. Oscillating external electromagnetic (EM) waves strike the surface of 2D materials. Because reflection occurs before absorption, some parts of the EM waves is immediately reflected from the surface (blue arrow). On the other hand, induced local dipoles contribute absorption of the incident waves penetrating the 2D layer structure (dashed blue

arrows). Transmitted waves with less energy are then subjected to the same mechanisms when they encounter the inner layers, generating multiple internal reflections (dashed black arrows). The energy of EM waves is substantially decreased, resulting in an attenuation or elimination.39

Figure 6. Schematic illustration of 2D materials based planar supercapacitors. (a) Schematic illustration of the flexible planar supercapacitor, using gel electrolyte and a flexible PET substrate. (b) Ion migration in a planar supercapacitors, which have two symmetric working electrodes. (c) The layered structure of 2D materials based supercapacitors. (d) Schematic illustration of 2D planar ion transport.40

Figure 7. Schematics of catalysis or active sites for 2D materials. (a) Defects and edges for active sites. (b) Doping atoms for active sites. (c) Functional groups and metal clusters for active sites. (d) Electron transfer from metal to 2D materials for catalytic activity. (e) Catalysis in the empty space between a metal electrode and 2D materials. (f) Catalytic activity from hetero-structure stacked by various

2D materials.....41

Figure 8. Schematic illustration of the mechanism of a graphene heater by EM waves. Graphene absorbs the energy of EM waves due to its strong diamagnetic response to EM, and dissipates the EM energy as heat energy, which can be utilized for fast and efficient heaters for various applications..49

Figure 9. Comparison of sheet resistance depending on substrates.....54

Figure 10. A schematic illustration of graphene stacking process through dry transfer method using PSAF. First, graphene covered by PSAF on copper was etched to remove metal catalyst and dried. After the roll-to-roll process, PSAF was peeled off. Through this process replication on target substrate, multiple layers graphene film was produced.62

Figure 11. Comparison of heat generation between dry transfer and wet transfer. (a) An actual image of graphene films transferred on a slide glass. (b,c) Infrared images of graphene heater applying microwave during 10second transferred by

wet transfer and dry transfer, respectively.63

Figure 12. The graphene films transferred on target substrates.

(a) An infrared scanning of the graphene heater transferred on quartz, while applying microwave during 10 seconds. The insets show an actual image of the graphene film. Scale bars, 1 cm. (b) The temperature variation of graphene heater transferred on target substrates. (c) Temperature profile comparison of Joule heating and EM heating at power 70 W on 4 layers of graphene films. (d) Saturation temperature uniformity of Joule heating and EM heating depending on number of graphene layers.64

Figure 13. Comparison of graphene heater transferred on various substrates.

(a,c,e) Infrared scanning images of the graphene heaters transferred on Si_3N_4 , PET, sapphire and Si wafers, respectively. The inset images are actual images. Scale bars are all the same, 1 cm. (b,d,f) Temperature variation of graphene films depending of stacking layers transferred on each substrates.65

Figure 14. Comparison of Joule heating and EM heating. (a) A

schematic structure of conventional Joule heating based graphene heater. (b) Temperature distribution of Joule-heating based heater made of 4 layers graphene films working at power 70 W. (c) Temperature distribution of EM-heating based heater made of 4 layers graphene films working at power 70 W. Samples shown for saturation temperature uniformity in Figure 2d were measured with the same methods indicated in figure 7b, c.66

Figure 15. The heat distribution depending on charge mobility.

(a) An infrared scanning of graphene heaters on SAMs irradiated by microwave during 10 seconds. Scale bar, 1 cm. (b) FET characteristics of graphene films depending on kinds of SAMs. (c) The temperature variation immediately measured after device fabrication. (d) The temperature variation measured after 7 days and annealing process.67

Figure 16. Optical and IR photographs showing the EM-induced defogging of graphene coated vials.

(a) The photograph before applying EM waves. Left is the graphene-coated bottle and right is the none-coated bottle. (b) The photograph after

r applying microwave during 5 seconds. (c) An infrared picture immediately obtained after microwave irradiation. Scale bars, 1 cm.68

Figure 17. Optical and IR photographs showing the Joule heating process. (a) The photograph before applying Joule heating. The monolayer graphene film is transferred on PET films. Scale bars, 2cm. (b) An infrared picture before applying Joule heating. (c) An infrared picture after applying Joule heating at saturated temperature using 70 W power. Scale bars, 1 cm.69

Figure 18. Raman spectra characteristics of the graphene heater by EM waves. (a) Variation of the G and 2D bands with irradiation time. (b) I_{2D}/I_G as functions of irradiation time. (c) A_{2D}/A_G as a function of the G peak shift. A_{2D} and A_G are the integral value of 2D peak and G peak respectively. (d) Position of the 2D peak as a function of the G peak shift (red line: p-doping effect, blue line: tensile/compressive stress following the arrow).70

Figure 19. Schematic working principle of a graphene-coated

contact lens and its fabrication process. (a) Electromagnetic (EM) wave passes through contact lens and absorbed by an eyeball, possibly causing heat damage inside. (b) EM energy is absorbed by graphene and dissipated as a heat before reaching the interior of the eye. (c–d) Dehydration of a contact lens can be reduced due to the gas–impermeability of graphene (e) The fabrication process of the graphene–coated contact lens.84

Figure 20. Optical and electrical properties of graphene films.

(a) Optical and SEM images of graphene samples transferred on a SiO₂ substrate. (b) Raman spectrum of graphene showing monolayer thickness and low defect density. (c) Transmittance of a bare contact lens and a graphene–coated contact lens. Scale bar: 1cm. (d–f) Evaluation of electrical properties of graphene samples, including 4–point sheet resistance measurement and *I–V* characteristics.....87

Figure 21. EMI shielding effect of the graphene–coated contact lens tested in a microwave oven. (a) Sample preparation for the microwave oven test. Egg whites on a Si wafer are covered

with the contact lenses with and without graphene coating, respectively. (b) A microwave oven test showing the excellent EMI shielding effect of the graphene-coated contact lens. The egg white protected by graphene shows less thermal denaturalization. (c) IR camera images showing the the elevated temperature of the graphene-coated lens inside a microwave oven, indicating the EM energy is efficiently absorbed and dissipated as heat.....89

Figure 22. Enhanced dehydration protection by a graphene coated contact lens. (a) Schematic of the experimental setup to measure the water evaporation rate through contact lenses. (b) Weight loss measured with time on a hot plate at 38°C. (c) Water vapor transmission rate (WVTR) values of the contact lenses without and with graphene coating, derived from (b). The dehydration protection performance has been enhanced by ~30%.....91

Figure 23. Demonstration of a light emitting diode (LED) fabricated on a graphene-coated contact lens with electrode patterns. (a) A schematic view of the fabrication processes

including the patterning of graphene by photolithography and O₂ plasma etching. (b–c) Optical and (d) SEM images of the patterned graphene on a contact lens. (e) Raman spectra of the patterned graphene on target substrates. (f) An assembled LED/graphene contact lens. (g) On/Off images of LED graphene lens operating voltage at 9 V.....93

Figure 24. Schematic illustration of the synthesis process of graphene–graphitic carbon supercapacitors by a common laser printer. The laser toner powder as a carbon source is pre-patterned on a metal foil. After annealing process, the graphene–graphitic carbon films on a metal foil is directly used as supercapacitors without additional treatment.....107

Figure 25. Binding materials in laser printing toner powders and their changes in Raman spectra before and after annealing. (a) Molecular structures of the binding materials in the laser printing toner excluding carbon powder and pigments. (b, c) Raman spectra of the toners with different colours laser-printed on a copper foil before and after annealing process..108

Figure 26. (a) A schematic illustration the synthesis of graphene-graphitic carbon layers. A laser-printed copper foil was placed in the cold zone of the quartz tube with flowing 50 sccm H₂ and 500 sccm Ar (section 1). When the centre of the furnace reached 800 °C, the furnace was moved to the position of the copper foil for annealing (section 2). After 30 min, the furnace was moved back to the cold zone, and the sample was rapidly cooled down to room temperature (section 3). (b) A temperature-time plot for the synthesis of graphene-graphitic carbon layers, corresponding to a... ..109

Figure 27. Photographic and microscopic images of the graphene-graphitic carbon materials formed by laser-printing and annealing. (a) Optical microscope images of the graphene-graphitic carbon devices before/after the annealing process. (b) SEM images of the non-patterned (left) and patterned area (right) after annealing. (c) A cross-sectional SEM image of graphene-graphitic carbon films after annealing. The inset shows a cross-sectional SEM image before annealing. (d) A high-resolution TEM image of the

graphene-graphitic carbon. The inset shows the corresponding diffraction pattern. (e) A photograph of the laser-printed finger patterns with various scales.....112

Figure 28. Mechanical, chemical stability tests and spectroscopic analyses. (a) Peeling-off test of the graphene-graphitic carbon electrodes using a commercial Scotch tape (left) and rubbing test (right). (b) Chemical stability test in organic electrolytes (1M LiPF₆ in EC/DMC and 1M LiTFSI in TEGDME). (c, d) Raman spectra and FT-IR spectra of the graphene-graphitic carbon electrodes before/after annealing. The peak at 1629 cm⁻¹ is originated from the sp² hybridization of carbon-carbon double bonding in plane stretching. (e, f) C 1s and O 1s XPS spectra before/after annealing. The O 1s peak for C=O bonding at (~532.0 eV) is shifted to the peak for C-O bonding (~533.0 eV).....116

Figure 29. Chemical stability test in various solvents. Negligible weight loss in various organic solvents (*i.e.* water, ethanol, isopropanol, and acetone) also exhibits the excellent chemical stability of graphene-graphitic carbon electrode.117

Figure 30. Transfer characteristics of graphene-graphitic carbon measured at $V_{ds} = 0.01V$. Graphene-graphitic carbon shows ambipolar behavior with a Dirac cone at $V_g \sim -50V$.118

Figure 31. Microscopic and spectroscopic analyses of the graphene-graphitic carbon formed on a nickel foil. (a) A photograph of the laser-patterned graphene-graphitic carbon layers on a nickel foil after annealing process. (b) SEM images of the laser-patterned (upper) and the non-patterned area (lower) on the nickel foil after annealing. (c) A cross-sectional SEM image of the graphene-graphitic carbon film on the nickel foil after annealing. (d) Raman spectra of the graphene-graphitic carbon electrode after annealing (e,f) C 1s and O 1s XPS spectra of the laser-printed graphene-graphitic carbon electrode before/after annealing on a nickel foil.....119

Figure 32. Electrochemical performance of graphene-graphitic carbon materials. (a) Typical charge/discharge profiles of materials before (sky blue) and after (dark blue) synthesis. (b) Charge/discharge profile with time vs. voltage. (c) Rate

capability of the electrodes with current density of 0.05–5 A g⁻¹. (d) Comparison of gravimetric power and gravimetric energy. (e) Cyclic voltammetry measurement and its plot in terms of log (scan rate) vs. log (peak current). (g) Cycle stability of the electrode. (h) Charge/discharge profile and (i) cycle stability of full cell consisting of graphene–graphitic carbon materials and activated carbon.....124

Figure 33. Electrochemical performance of the graphene–graphitic carbon materials laser–printed and annealed on a nickel foil. (a) Typical charge/discharge profiles of materials. (b) Charge/discharge profiles in time vs. Voltage. (c) Rate capability of the electrodes with current density of 0.05–5 A g⁻¹. (d) Cycle stability of the electrode. (e) Charge/discharge profiles and (f) cycle stability of full cell comprised of graphene–graphitic carbon materials and activated carbon.125

Figure 34. Schematic illustration of the entire process and bilayer MoS₂ films characterization. (a) Schematic illustration of UV–Ozone engineered bilayer MoS₂ films synthesized by

MOCVD. (b) Raman spectra and of bilayer MoS₂. (c) AFM image of MOCVD grown bilayer MoS₂ with a thickness of ~ 1.4 nm, as measured along the yellow line in inset profile. (d,e) CS-TEM image of bilayer MoS₂ shows its hexagonal planar lattice: the inset shows a fast Fourier transform (FFT).
143

Figure 35. A photograph and SEM image of MOCVD-grown monolayer MoS₂ on a sapphire substrate. Not only SiO₂/Si wafer but also sapphire could be also used as a growth substrate. Triangular crystal shape, which size is below 250 nm, is confirmed at 60 min growth time.144

Figure 36. TEM image and EDS spectrum of the pristine bilayer MoS₂ films. (a) TEM image of the bilayer MoS₂ on a conventional lacey copper grid. (b) EDS spectrum of the bilayer MoS₂ films at white square in (a).....145

Figure 37. XPS spectra for MoS₂ bilayer grown by our method. (a) Mo 3d 5/2, 3/2 and S 2s state. (b) S 2p 3/2 and 1/2...146

Figure 38. A photograph and PL measurement of the pristine

bilayer MoS₂ on SiO₂/Si wafer. (a) Optical microscope image of the bilayer MoS₂ synthesized by our MOCVD on SiO₂/Si wafer. (b) PL spectrum of the bilayer MoS₂ obtained at (a) compared with a bare SiO₂/Si wafer. (c) PL mapping of the bilayer MoS₂ obtained at (a).....147

Figure 39. Characterization of bilayer MoS₂ films after UV-ozone treatments. (a) Raman spectrum of bilayer MoS₂ films under UV-ozone. (b) PL spectra of the bilayer MoS₂ under UV-ozone. (c) PL peak wavelength as a function of UV-ozone exposure time. (d) CS-STEM HAADF images after UV-ozone: the inset shows a FFT which converts to hexagonal pattern. (e) EELS spectrum of pristine bilayer MoS₂ and after UV-ozone treatments. (f-h) XPS spectra of pristine bilayer MoS₂ and after UV-ozone treatments for Mo 3d, S 2p, O 1s and C 1s, separately.....152

Figure 40. CS-TEM analysis after UV-ozone treatment on the bilayer MoS₂. (a,c,f) CS-STEM HAADF images after UV-ozone treatment at various locations. (b,d,f) EELS spectrum at line profile in (a), (c) and (e), respectively.....153

Figure 41. PL intensity variation depending on laser exposure time and exciton life-time measurement. (a,b) PL intensity variation of UV–ozone treated bilayer MoS₂ depending on 473 nm laser exposure time. (c) The ratio of in–situ PL intensity to initial PL intensity after laser 125 sec exposure. (d) Exciton life–time spectra of bilayer MoS₂ synthesized by MOCVD depending on UV–ozone process time.156

Figure 42. HER properties of bilayer MoS₂ synthesized by MOCVD before and after UV–ozone treatment. (a) polarized CV curves show the cathodic sweep of the first cycle. Enhanced activity is observed after UV–ozone treatment. (b) Tafel plots show the improved electrochemical activity of the bilayer MoS₂ catalyst with UV–ozone treatment. (c) Stability test for bilayer MoS₂ on glassy carbon. (d) The mechanism illustration of UV–ozone treated MoS₂ HER compared of pristine MoS₂.161

Figure 43. HER overpotential performance comparison. HER overpotential values of MoS₂ electrocatalysts at 5 mA/cm² are compared. References were focused on film types excluding

mulilayers MoS₂ derived from chemical exfoliation or
composites with other materials.....162

List of Tables

Table 1. Exciton life-time values depending on UV-ozone exposure time. Computational DFT theory and exfoliation experimental values are studied in previously report.157

Table 2. HER performance compairson. References were focused on pure film types excluding chemically exfoliated MoS2 combined with other materials and functional groups.163

Chapter 1. *Introduction*

1.1. Classification of 2D materials synthesis methods

1.1.1. Mechanical exfoliation

The first appearance of 2D materials is attributed to the graphene cleavage from highly ordered pyrolytic graphite (HOPG) in 2004.¹ The experimental method of mechanical exfoliation is presented in Figure 1 using commercial Scotch tapes.² A normal force (or adhesion force) between Scotch tape and the surface layers of 2D materials overcome the van der Waals attraction between their adjacent layers. Through numerous repetitions, single layer is appeared. This method provides high-quality 2D materials on a target substrate compared with other synthesis methods. However, the yield of this technique is too minuscule and not suitable for scalable and industrial application. In addition, sample preparations are extremely hard working and time consuming. Although these

drawbacks are found in the mechanical exfoliation, this discovery has significant science value.

1.1.2. Liquid exfoliation

Liquid exfoliation could improve the realistic problems of mechanical exfoliation. This techniques give large quantities of dispersed 2D materials and a possibility for their industrial applications. In this chapter, we briefly summarize main liquid exfoliation methods and their limits, as shown in Figure 2.³

Actually, the Scotch tape method is not the first attempt to observe a monolayer materials. Before the mechanical exfoliation, bulk layered materials like graphite are commonly treated with oxidation and subsequent sonication into appropriate solvents.⁴ The results are lots of production of homogenously atomic thin flakes (5~20 layers) dispersed in a solvent. However, the flakes have various dangling bonds like hydroxyl, carbonyl, carboxyl and *etc.* Although these dangling bonds are removed by reduction or heat treatment, remained structural defects could degrade electrical, optical and thermal properties.

Liquid exfoliation also uses ionic species to intercalate the layer spacing or exchange the cationic counterions in layered bulk materials like transition metal dichalcogenides (TMDC).^{5,6} Intercalation and subsequent sonication increases the layer spacing, resulting in 2D dispersed nanosheets. Nevertheless, ionic intercalation or exchange process inevitably grips with physical or chemical absorption of the ions at the surface, which damage the intrinsic properties. The electrical and optical properties of the layers synthesized by this method show comparable that of the mechanical exfoliated layers. There

1.1.3. Chemical vapor deposition

Chemical vapor deposition (CVD) breaks fresh ground for large-area synthesis of 2D materials and its industrial applications. First, graphene is synthesized by low pressure CVD (LPCVD) method using methane gas and transition metal catalysts at high temperature, as shown in Figure 3.⁷⁻⁹ Taking this discovery, various doping and transfer methods have been explosively studied.^{10,11} The LPCVD method has also been utilized to the synthesis of TMDC materials as well as graphene, using their solid or gas phase precursors.

However, the LPCVD based TMDC synthesis has difficulty in controlling precise flow of the precursor in a reaction chamber and often provide inhomogeneous layers on target substrates. Recently, metal organic CVD (MOCVD) demonstrates layer by layer uniform growth of the TMDC, as shown in Figure 4.¹² Therefore, we believe that MOCVD based 2D materials synthesis would provide a platform for industrial and practical technologies in the future.

In our study, we introduce LPCVD based graphene synthesis for EMI shielding and smart contact lens application. Furthermore, we demonstrate graphene-graphitic carbon synthesis for electrochemical application, using roll-to-roll laser printing techniques. Finally, we develop MOCVD based MoS₂ synthesis as a catalyst for hydrogen evolution reaction.

1.2. EMI shielding properties of 2D materials

Recently, flexible, wearable and wireless network electronic devices are widespread throughout the developed world and future society is even more so. However, these devices can have harmful impacts on device performance, surrounding environments and even human body.¹³ Conducting materials, whose charge carriers could interact with electromagnetic fields, have been used as main components for commercial EMI shielding application.^{14,15}

Light-weight and very thin shielding materials are necessarily needed by the minute with advances in electronic device. Figure 5 shows that 2D materials are proper alternatives for conventional metal based shielding materials, because they have atomic thickness and superior conductivity for EMI shielding.¹⁶ Especially, graphene, planar honeycomb lattice of sp² hybridized carbon, is promising for transparent EMI shielding and absorbing material. The electromagnetic

loss characterization of graphene, which is normalized to the film thickness, shows at least two orders of magnitude higher than that of conventional EMI shielding and absorbing materials.¹⁷

In our study, we demonstrate heat generation of graphene films by electromagnetic absorption. Furthermore, we introduce graphene coated smart contact lenses for EMI shielding and dehydration protection. We believe that our study could pave the way for EMI shielding application of 2D materials.

1.3. Electrochemical properties of 2D materials

Energy emergency is one of the greatest problems for solution in our modern societies. Two dimensional materials have been recognized as a promising material in the field of electrochemical catalysts and energy storage devices due to their own superior properties like flexibility, light-weight, environment friendly and *etc.*¹⁸

In case of energy storage applications, graphite is a frequently used anode materials for lithium ion batteries.^{19,20} Recently, other 2D materials have been also explosively studied as batteries or supercapacitor applications.²¹⁻²⁴ Their layered structure allow ions or electrons to migrate, showing considerable mechanical and chemical stability, as shown in Figure 6.²⁵ The developments of 2D materials and their hetero-structure give a possibility to overcome the challenges substantially owned by energy needs.

Considering aspects of electrochemical catalysts, 2D

materials also have many advantages for improving the conventional efficiency. In particular, many previous research have focused on the electrochemical production of hydrogen at various 2D materials based catalysts.²⁶⁻²⁹ There are two main efforts to increase the catalyst effect of 2D materials; i) providing more hydrogen evolution reaction (HER) active sites, ii) increasing the intrinsic catalytic activity of 2D materials and their conductivity, as shown in Figure 7.³⁰

In our research, we devise a new method to synthesize graphene-graphitic carbon hetero-structure for high efficiency supercapacitors, using commercial roll-to-roll based laser printing. In addition, we develop the catalytic effects of basal plane and increase the edge sites in MoS₂ synthesized by MOCVD and UV-ozone treatment.

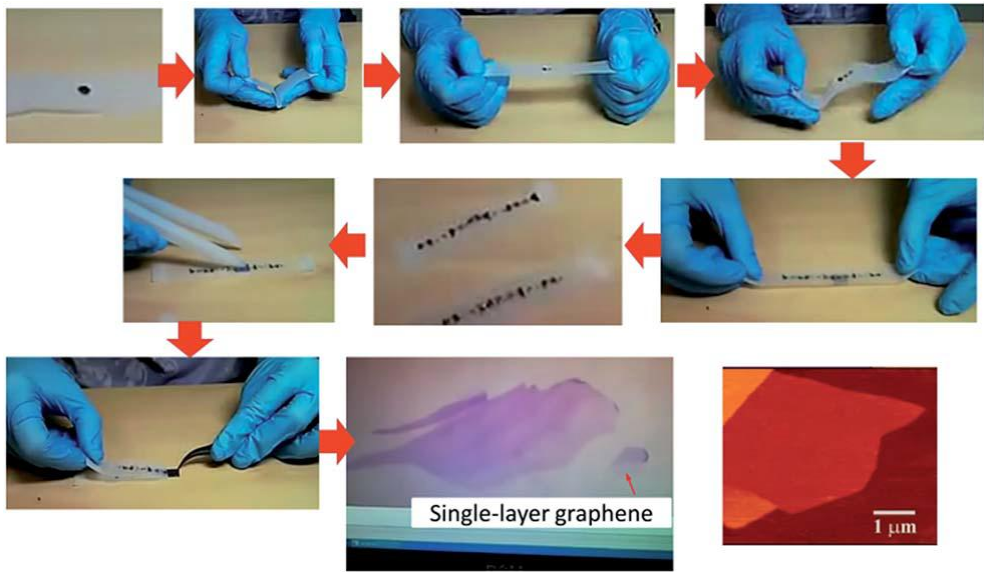


Figure 1. An illustrative procedure of the mechanical exfoliation.² Single-layer graphene is exfoliated from HOPG using commercial Scotch tape technique.

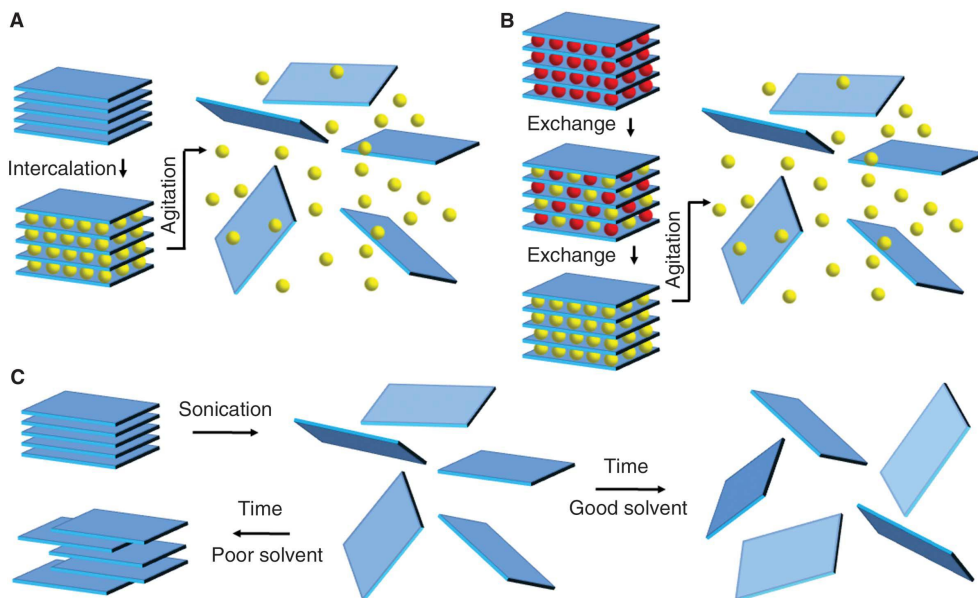


Figure 2. Schematic illustration of the main liquid exfoliation mechanisms.³ (a) Ion intercalation. Ions are intercalated between the layers in liquid environment and their agitations could separate the layers, (b) Ion exchange. Some layered compounds contain ions, which can be exchanged in a liquid environment for other. Then, their agitation provides an exfoliated dispersion. (C) Sonication assisted exfoliation. The layered crystal is sonicated in a solvent, resulting in exfoliation and formation of nanosheets.

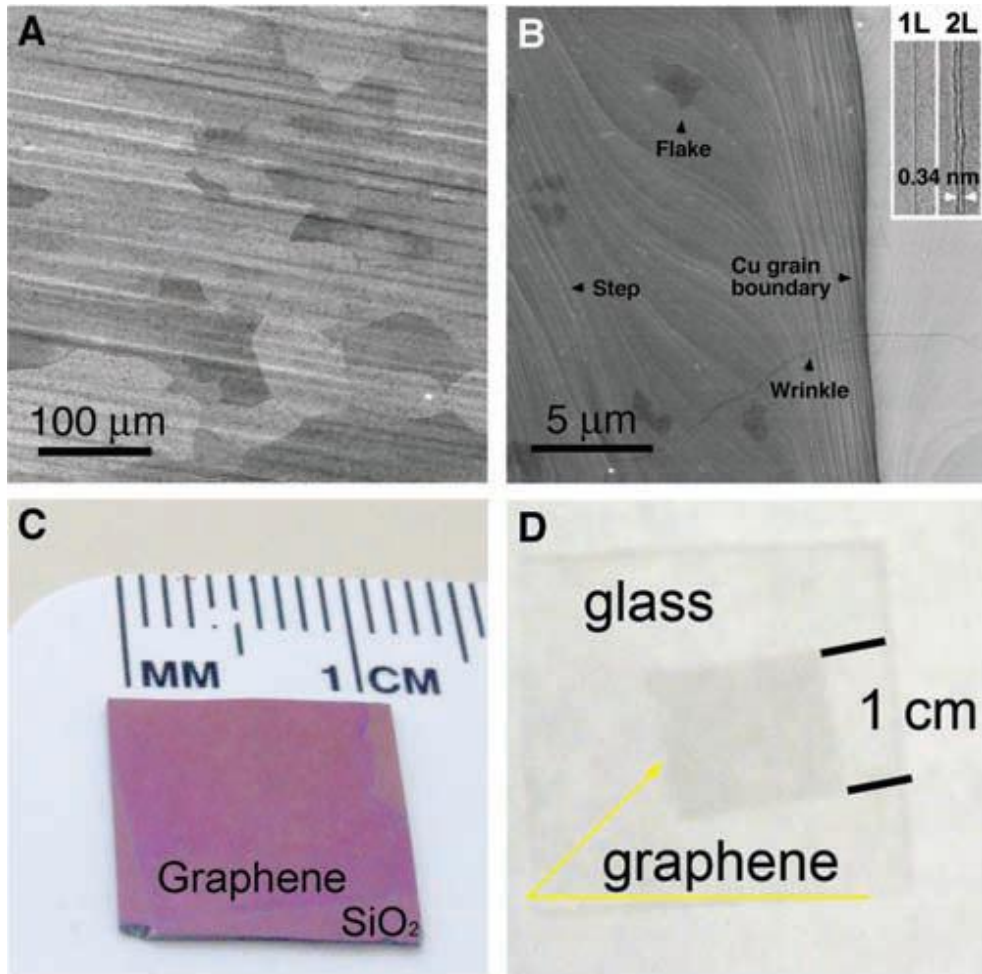


Figure 3. Large-area synthesis of high-quality and uniform graphene films on copper foils using LPCVD.⁷ (a,b) SEM image of graphene on a copper foil synthesized by LPCVD (c,d) Using conventional wet transfer, graphene films transferred onto a SiO₂/Si substrate and a glass plate, respectively.

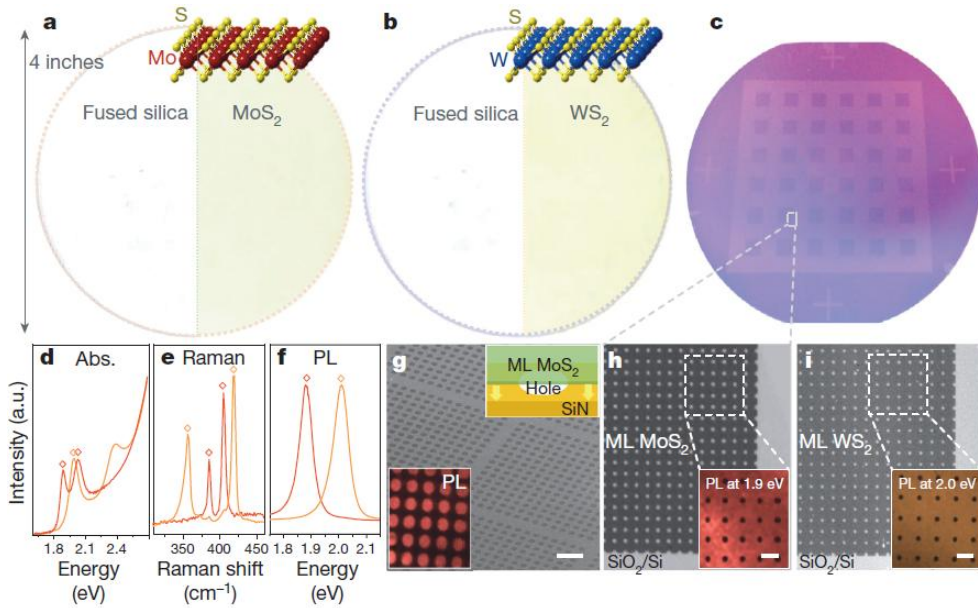


Figure 4. Wafer-scale synthesis of high-quality and uniform TMDC films synthesized by MOCVD.¹² (a,b) Photographs of monolayer MoS₂ and WS₂, respectively. (c) Photograph of patterned single-layer MoS₂ film on a 4-inch SiO₂/Si wafer. (d) Optical absorption spectra of monolayer MoS₂ (red line) and WS₂ (orange line) films. (e,f) Raman and photoluminescence (PL) spectra of monolayer MoS₂ (red line) and WS₂ (orange line) films. (g) Scanning electron microscopy (SEM) and PL image of monolayer MoS₂. (h,i) Optical images of MoS₂ and WS₂, respectively. The insets show PL images at 1.9 eV. All scale bars in the above images are 10 μm.

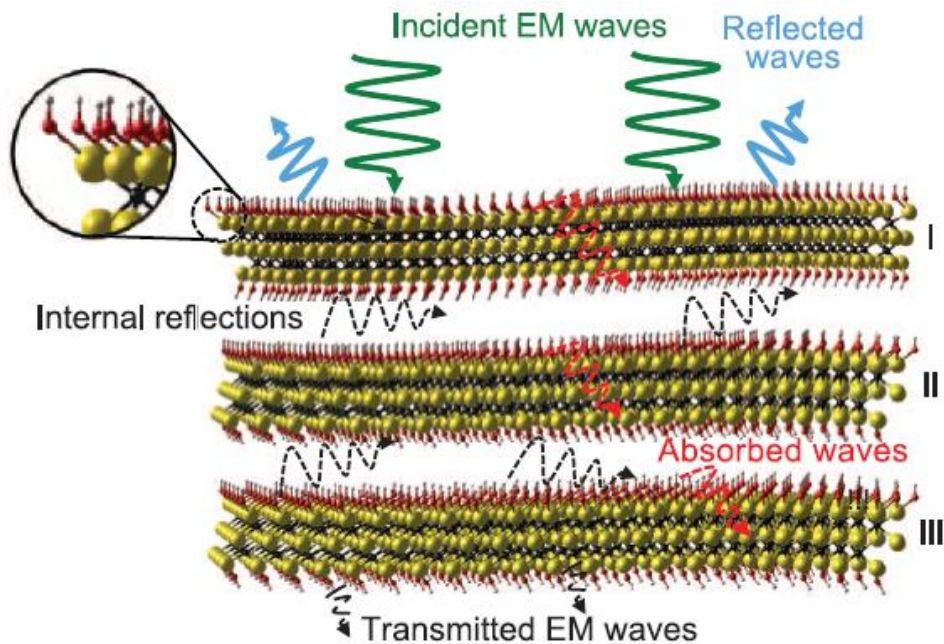


Figure 5. Proposed EMI shielding mechanisms of 2D materials.¹⁶ Oscillating external electromagnetic (EM) waves strike the surface of 2D materials. Because reflection occurs before absorption, some parts of the EM waves are immediately reflected from the surface (blue arrow). On the other hand, induced local dipoles contribute to the absorption of the incident waves penetrating the 2D layer structure (dashed blue arrows). Transmitted waves with less energy are then subjected to the same mechanisms when they encounter the inner layers, generating multiple internal reflections (dashed black arrows). The energy of EM waves is substantially decreased, resulting in an attenuation or elimination.

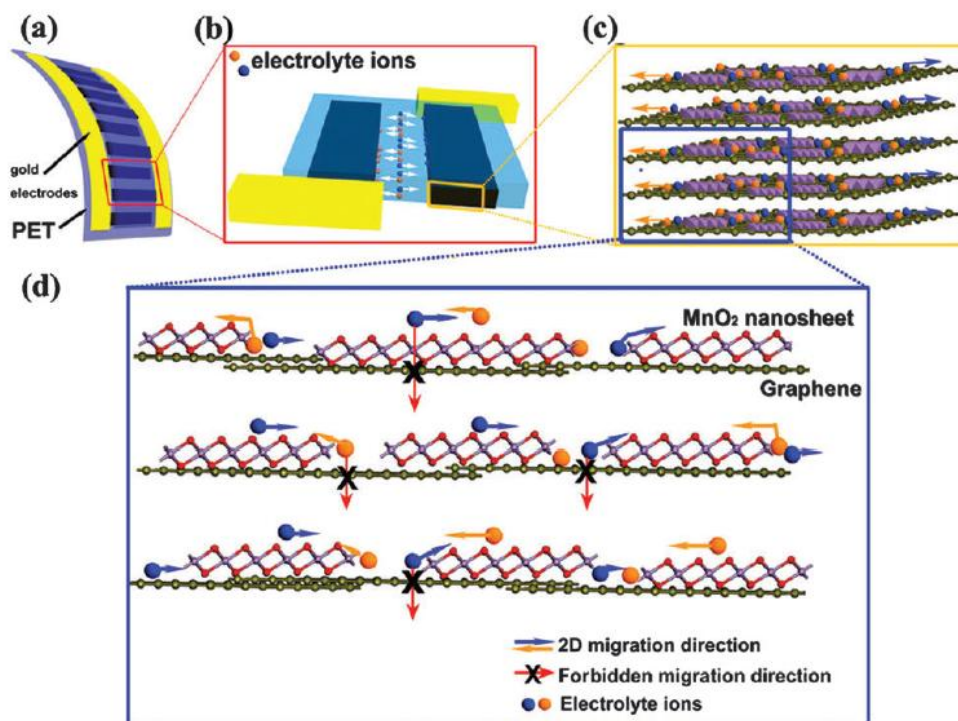


Figure 6. Schematic illustration of 2D materials based planar supercapacitors.²⁵ (a) Schematic illustration of the flexible planar supercapacitor, using gel electrolyte and a flexible PET substrate. (b) Ion migration in a planar supercapacitors, which have two symmetric working electrodes. (c) The layered structure of 2D materials based supercapacitors. (d) Schematic illustration of 2D planar ion transport.

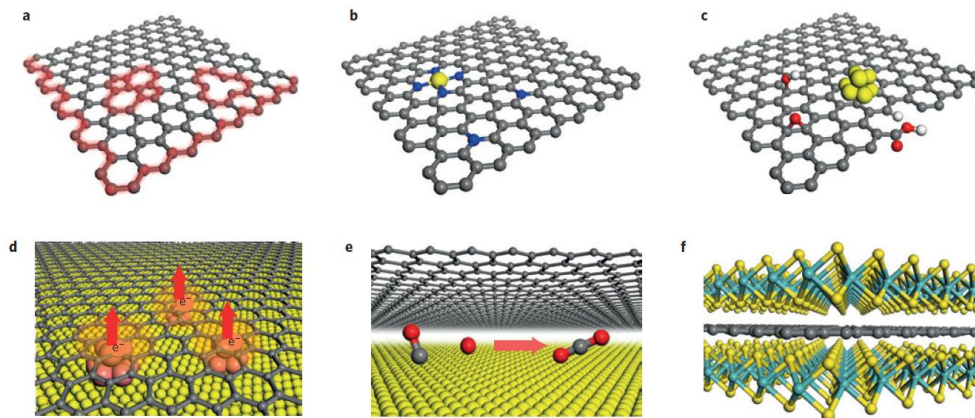


Figure 7. Schematics of catalysis or active sites for 2D materials.³⁰ (a) Defects and edges for active sites. (b) Doping atoms for active sites. (c) Functional groups and metal clusters for active sites. (d) Electron transfer from metal to 2D materials for catalytic activity. (e) Catalysis in the empty space between a metal electrode and 2D materials. (f) Catalytic activity from hetero-structure stacked by various 2D materials.

1.4. References

1. Novoselov, K. S.; Geim, A. K.; Morozov, S. V.; Jiang, D.; Zhang, Y.; Dubonos, S. V.; Grigorieva, I. V.; Firsov, A. A. *Science* **2004**, 306, 666.
2. Yi, M.; Shen, Z. *J. Mater. Chem. A* **2015**, 3, 11700–11715.
3. Valeria, N.; Manish, C.; Mercouri G. K.; Michael, S. S.; Jonathan, N. C. *Science* **2013**, 340, 1420–1439.
4. Dreyer, D. R.; Park, S.; Bielawski C. W.; Ruoff R. S. *Chem. Soc. Rev.* **2010**, 39, 228–240.
5. Ma, R.; Sasaki, T. *Adv. Mater.* **2010**, 22(45), 5082–5104.
6. Eda, G.; Yamaguchi, H.; Voiry, D.; Fujita, T.; Chen, M.; Chhowalla, M. *Nano Lett.* **2011**, 11(12), 5111–5116.
7. Li, X. S.; Cai, W. W.; An, J. H.; Kim, S.; Nah, J.; Yang, D. X.; Piner, R.; Velamakanni, A.; Jung, I.; Tutuc, E.; Banerjee, S. K.; Colombo, L.; Ruoff, R. S. *Science* **2009**, 324 (5932), 1312–1314.
8. Kim, K. S.; Zhao, Y.; Jang, H.; Lee, S. Y.; Kim, J. M.; Kim, K. S.; Ahn, J. H.; Kim, P.; Choi, J. Y.; Hong, B. H. *Nature* **2009**, 457, 706.

9. Bae, S.; Kim, H.; Lee, Y.; Xu, X. F.; Park, J. S.; Zheng, Y.; Balakrishnan, J.; Lei, T.; Kim, H. R.; Song, Y. I.; Kim, Y. J.; Kim, K. S.; Ozyilmaz, B.; Ahn, J. H.; Hong, B. H.; Iijima, S. *Nat. Nanotech.* **2010**, *5*, 574.
10. Liu, H.; Liu, Y.; Zhu, D. *J. Mater. Chem.* **2011**, *21*, 3335–3345.
11. Kang, J.; Shin, D.; Bae, S.; Hong, B. H. *Nanoscale* **2012**, *4*, 5527–5537.
12. Kang, K.; Xie, S. E.; Huang, L. J.; Han, Y. M.; Huang, P. Y.; Mak, K. F.; Kim, C. J.; Muller, D.; Park, J. *Nature* **2015**, *520*(7549), 656–660.
13. Chen, Z.; Xu, C.; Ma, C.; Ren, W.; Cheng, H. M. *Adv. Mater.* **2013**, *25*, 1296–300.
14. Yang, S. M.; Chang, Y. Y.; Hsieh, Y. C.; Lee, Y. J. *J. Appl. Polym. Sci.* **2008**, *110*, 1403–10.
15. Chung, D. D. L. *Carbon* **2001**, *39*, 279–85.
16. Shahzad, F.; Alhabeb, M.; Hatter, C. B.; Anasori, B.; Hong, S. M.; Koo, C. M.; Gogotsi, Y. *Science* **2016**, *353*(6304), 1137–1140.
17. Kang, J.; Kim, D.; Kim, Y.; Choi, J-B.; Hong, B. H.; Kim, S.

- W. *2D Mater.* **2017**, *4*, 025003.
18. Chia, X.; Eng, A. Y.; Ambrosi, A.; Tan, S. M.; Pumera, M. *Chem. Rev.* **2015**, *115*, 11941–11966.
19. Endo, M.; Kim, C.; Nishimura, K.; Fujino, T.; Miyashita, K. *Carbon* **2000**, *38*, 183.
20. Komaba, S.; Itabashi, T.; Kaplan, B.; Groult, H.; Kumagai, N. *Electrochem. Commun.* **2003**, *5*, 962.
21. Zhao, Y. Y.; Kuai, L.; Liu, Y. G.; Wang, P. P.; Arandiyan, H.; Cao, S. F.; Zhang, J.; Li, Y.; Wang, Q.; Geng, B. Y.; Sun, H. Y. *Sci. Rep.* **2015**, *5*, 8722.
22. Weng, Q. H.; Wang, X.; Wang, X. B.; Zhang, C.; Jiang, X. F.; Bando, Y.; Golberg, D. *J. Mater. Chem. A* **2015**, *3*, 3097.
23. Huang, Y.; Liang, J. J.; Chen, Y. S. *Small* **2012**, *8*, 1805.
24. Acerce, M.; Voiry, D.; Chhowalla, M. *Nat. Nanotechnol.* **2015**, *10*, 313.
25. Peng, L.; Peng, X.; Liu, B.; Wu, C.; Xie, Y.; Yu, G. *Nano Lett.* **2013**, *13*, 2151–2157.
26. Jaramillo, T F.; Jorgensen, K. P.; Bonde, J.; Nielsen, J. H.; Horch, S.; Chorkendorff, I. *Science* **2007**, *317*, 100–102.
27. Chia, X.; Ambrosi, A.; Sofer, Z.; Luxa, J.; Pumera, M. *ACS*

Nano **2015**, *9*, 5164–5179.

28. Chhowalla, M.; Shin, H. S.; Eda, G.; Li, L.-J.; Loh, K. P.;

Zhang, H. *Nat. Chem.* **2013**, *5*, 263–275.

29. Lukowski, M. A.; Daniel, A. S.; Meng, F.; Forticaux, A.; Li,

L. S.; Jin, S. *J. Am. Chem. Soc.* **2013**, *135*, 10274–10277.

30. Deng, D.; Novoselov, K. S.; Fu, Q.; Zheng, N.; Tian, Z.;

Bao, X. *Nat. Nanotechnol.* **2016**, *11*, 218–230.

Chapter 2. *EMI shielding application of graphene*

2.1. Efficient heat generation in large-area graphene films by electromagnetic wave absorption

2.1.1. Introduction

Graphene has intrigued the interest of world-wide researchers due to its extraordinary electrical¹⁻³, mechanical^{4,5}, optical^{6,7} and chemical^{8,9} properties. In particular, the superior thermal conductivity of graphene lead many researchers into using graphene as core materials in heating applications.^{10,11} Through the development of chemical vapor deposition (CVD)¹² and roll-to-roll process for large size graphene film synthesis¹³, graphene received much attention as a flexible and transparent material in heater application¹⁴ and even considered as an alternative to indium tin oxide (ITO)-based heaters.^{15,16} The general heat generation

mechanism of carbon materials is known to be Joule heating.^{10,17} Joule heating is the process by which the movement of current through a conductor releases heat due to its resistance. However, the heating rate and efficiency of the graphene-based heater arising from Joule heating was limited by the conductivity of graphene which is related to the restraint of sheet resistance.^{18,19}

Here we report a novel method to generate heat on a large-area graphene film by applying the unique electromagnetic (EM) wave absorption property²⁰ of graphene materials. The EM wave induces an oscillating magnetic moment generated by the orbital motion of moving electrons in graphene, which efficiently absorbs the EM energy and dissipates it as a thermal energy (Figure 8). In this case, we can expect that the electron mobility is important than the conductivity of graphene, because the diamagnetic moment is directly proportional to the speed of electron in an orbital motion. Thus, we tried to control the carrier concentration of graphene by functionalizing substrates with self-assembled monolayers (SAM), and found that the graphene film that

shows the Dirac voltage close to zero can be more efficiently heated by EM waves. In addition, the temperature gradient also depends on the number of graphene layers due to the increased accumulation of diamagnetism. This heating method would be advantageous for sensing of EM waves, defogging smart windows, highly efficient and quick heating, etc.

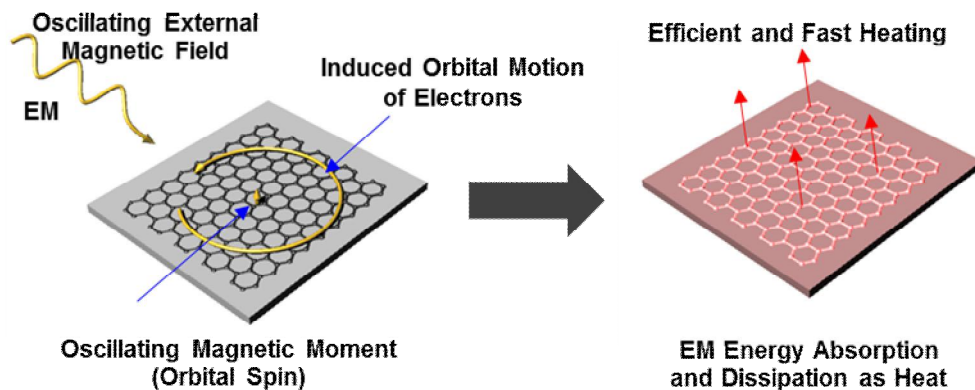


Figure 8. Schematic illustration of the mechanism of a graphene heater by EM waves. Graphene absorbs the energy of EM waves due to its strong diamagnetic response to EM, and dissipates the EM energy as heat energy, which can be utilized for fast and efficient heaters for various applications.

2.1.2. Experimental

Graphene synthesis and transfer. Graphene film was synthesized by chemical vapor deposition. Monolayer graphene was produced on a 25 μm thick Cu foil (Alfa Aesar, 99.999%) with 70 mTorr H_2 (4 sccm) and 650 mTorr CH_4 (35 sccm) gas flow rate at 1000 $^\circ\text{C}$. The synthesized graphene on Cu was coated by Pressure Sensitive Adhesive Films (PSAF) and followed by Cu catalyst etching using 0.1M ammonium persulfate (APS) solution. The graphene films on the PSAF was rinsed with distilled water and conserved in dehydrated condition for dry transfer. The graphene on the PSAF was affixed to the target substrates by weak pressing or roll to roll process. The comparison of multilayer graphene heaters can be fabricated by conventional wet transfer method and repeatedly transferring these graphene onto the same substrate.

EM heating and Joule heating comparison. We used a microwave oven manufactured by SAMSUNG electronics, as the source of microwaves (frequency = 2.45 GHz). The power of EM heating can be manipulated from 50 W to 700 W

with this equipment. To calculate the power of Joule heating of each substrates, Van der Pauw method was utilized to measure the sheet resistance. (Figure 9)

$$P = VI = V^2/R$$

$$R = \rho (L/A) = \rho (L/\delta W)$$

The power of Joule heating was controlled by the equation above. The distance between cu electrode that supplies the voltage was L, the thickness of graphene film (0.334 nm) was δ , and the width of graphene heater was W. The resistivity was calculated by multiplying the modification factor 4.5324 to sheet resistance.

Device Fabrication functionalizing substrates with self-assembled monolayers(SAMs). Highly p-doped Si substrates covered with a 300 nm thick Si₃N₄ were used for the electrical measurement of graphene field effect devices. After treating piranha and rinsing the substrates with DI water, the substrates were placed in a reaction flask. A 20 mL of toluene was added to the reaction flask as well as the silane coupling

agent(10 mM). We used two kinds of silanes : γ -aminopropyltriethoxysilane(APS) and octadecyltrichlorosilane (OTS) for controlling dirac-points. The reaction was performed under an argon atmosphere for 2 hours. After reaction was completed, the substrate was baked at 120 °C for 10 min, weakly sonicated for 3 min, cleaned with toluene and then dried under vacuum medium. The graphene film on PSAF was transferred to the prepared substrates and PSAF was carefully pilled off from the graphene film. Cr/Au (5 nm/ 30 nm) electrode were thermally deposited using pre-patterned stensile mask. Graphene channels were isolated through electron beam lithography and O₂ plasma. Before measuring the electrical properties of the graphene device, thermal annealing was carried out at 300 °C for 1h under Ar/H₂ gas to remove the unnecessary impurities on graphene surface.

Characterization. An infrared camera (FLIR T650sc) was used to measure the temperature gradient of the graphene films. The sheet resistance was measured using a 4-probe with a nanovoltmeter (Keithley 6221, 2182A) and the Van der Pauw method was applied. The electrical properties were measured

by Agilent 2602. Constant 10 mV voltage was applied from source to drain during the measurement. The Raman spectra were recorded using Renishaw Invia Raman Microscope with 1mW 514nm Ar laser with the spot size of 2 μm .

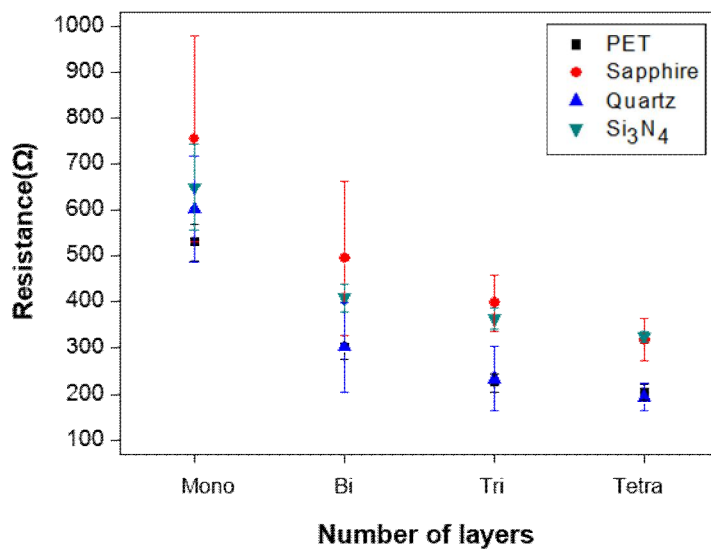


Figure 9. Comparison of sheet resistance depending on substrates.

2.1.3. Results and Discussion

First, a large scale graphene film was synthesized by CVD on a high purity Cu foil and dry transferred to a target substrate. The conventional wet transfer method produces unnecessary dipoles between graphene and substrates by the interference of water droplets causing increase in heat generation. In addition, unwanted doping effects on graphene film are produced by metal etching solution and polymer residues.²¹ Recently dry transfer using pressure sensitive adhesive films (PSAF) instead of wet transfer using a supporting polymer was developed to avoid these problems.²² Therefore, in order to accurately analyze the heating mechanism of graphene by EM waves, the dry transfer method is inevitable (Figure 10, 11).

Figure 12a,b shows infrared (IR) scanning of graphene surface on quartz substrates irradiated by EM wave at 2.45 GHz. The reason why we chose microwave spectra in these experiments is due to the frequent use of microwave in our everyday life. Unlike natural quartz, graphene film coated

quartz plate generates heat depending on the number of stacked layers. The reason that the heat generation increases with number of graphene layers is due to not only Joule heating between the graphene layers but also the accumulated diamagnetism proportional to the increment of layers. Except quartz, various substrates coated by graphene films show heat gradient by EM waves (Figure 13). Figure 12c represents the comparison of time consumed for Joule heating and EM heating to reach the saturation temperature. The typical Joule heating occurs from electron scattering on defect sites of graphene film. So the heat is generated initially at the defect site and diffuses to the entire film as form of additional electron scattering and lattice vibration.¹⁴ Therefore, Joule heating process requires adequate amount of time. In case of EM heating the entire graphene film absorbs electromagnetic wave, therefore, it shows faster increase in temperature compared to the Joule heating. This difference also affects the temperature uniformity after the saturation temperature. The power control of EM heating and joule heating will be further elaborated on method section. Figure 12d, for Joule heating in

monolayer graphene, indicates the local generation of heat due to the difficulty in achieving uniform sheet resistance. But as graphene films are stacked in layers their sheet resistance becomes more uniform, and uniform temperature distribution can be observed at four layer stacked graphene. Whereas in EM heating, the entire surface of film absorbs electromagnetic wave as mentioned above, so even in monolayer graphene uniform temperature distribution is detected. The uniformity of saturation temperature also increases proportionally to the stacked layers of graphene films in EM heating. This phenomena in EM heating is related to the Joule heating occurring at mismatch lattices between layers and also due to the increase in electromagnetic absorption following multiple stacked graphene layers.²³ Detailed comparison experiment with Joule heating is described in Figure 14.

To understand the mechanism of the heat generation by the absorption of EM waves, we describe experimental results obtained from changing the temperature of the graphene film on the Si_3N_4 substrates under the different Dirac-voltage and charge carrier mobility. The ordered close-packed structure

of self-assembled monolayers (SAMs) can suppress the substrate-induced doping on graphene, thereby the Dirac-voltage and work-function of the graphene could be tuned by SAMs.^{24,25} Thus, we functionalized the substrates with SAMs to control the Dirac-voltage and mobility.

Figure 15a,b demonstrate that the graphene which shows the Dirac-voltage close to zero can be more efficiently heated by EM waves. Two types of silanes move the Dirac-voltage of pristine graphene close to zero, and the γ -aminopropyltriethoxysilane (APS) brought the gradient closer to zero than that of octadecyltrichlorosilane (OTS). As Dirac-voltage approached to zero, graphene devices showed increasing electron mobility of 633 ± 108 (pristine), 1123 ± 232 (OTS), and 1568 ± 461 (APS) $\text{cm}^2\text{V}^{-1}\text{s}^{-1}$ respectively. The differences of heat generation has such tendency, the diamagnetic properties were directly proportional to the electron mobility in graphene film. The relative permittivities remain the same, because the comparatively long chains of the two silanes produce very weak dipole and the SAMs functions to subtly reduce the effect of substrates. Therefore, the heat

distribution of graphene films immediately measured after device fabrication in Figure 15c was originated from differences of mobility. Interpreting the following phenomena with the conventional Joule heating mechanism, the temperature in samples functionalized with OTS SAMs should increase higher as they show better conductivity in FET measurement compared to those functionalized with APS SAMs. However, in this experiment APS SAMs functionalized samples showed superior heat generation and this can be explained with the increased diamagnetism due to electron mobility in EM heating. The adsorption of impurities such as dust, water and oxygen is inevitable during FET sample preparation and measurement. When these impurities are exposed to EM waves, the temperature of the FET sample will be more increased due to dipole vibration. To insure the elimination of impurities, post annealing process is necessary. Therefore, we performed annealing process in Ar/He circumstance at 300 °C after 7 days to remove these additional dipole factors and confirmed that the heat distribution originated from the relative mobility differences

(Figure 15d).

Figure 16a shows the contrast of frost and steam on the non-coated glass bottle and the graphene-coated glass bottle. The graphene films can be applied to curved surface by dry transfer and EM waves even without electrodes to generate the Joule-heating. Irradiated by microwave for 5 seconds, the graphene-coated glass bottle was completely clear compared to the non-coated glass bottle (Figure 16b,c). This result shows apparent contrast with regular Joule heating which requires at least 30seconds to reach the intended saturation gradient. Also heating on curved surface via Joule heating is difficult as additional electrodes are needed. (Figure 17) This suggests that the graphene heater by EM waves is applicable to smart windows and EM wave detectors.

The EM waves can give P-doping effect to graphene film²⁶ and may reduce the efficiency as a practical heater. Figure 5a shows the variation of Raman spectrum during the time of irradiated electromagnetic wave in graphene films. P-doping effects were confirmed via the ratio of intensity and area of G peak and 2D peak. (Figure 18) Convincingly in

Figure 18d, analyzing the 2D peak shift following the G peak shift, the graphene film exposed to electromagnetic wave showed P-doping effects to some degree. However as indicated previously, less than 1 minute is need to reach the desired saturation temperature, thus practical P-doping followed by electromagnetic wave is not obtainable due to time limitation. Thus, the quick heat generation and stability of graphene films by EM waves can be applied to produce transparent and flexible heaters.

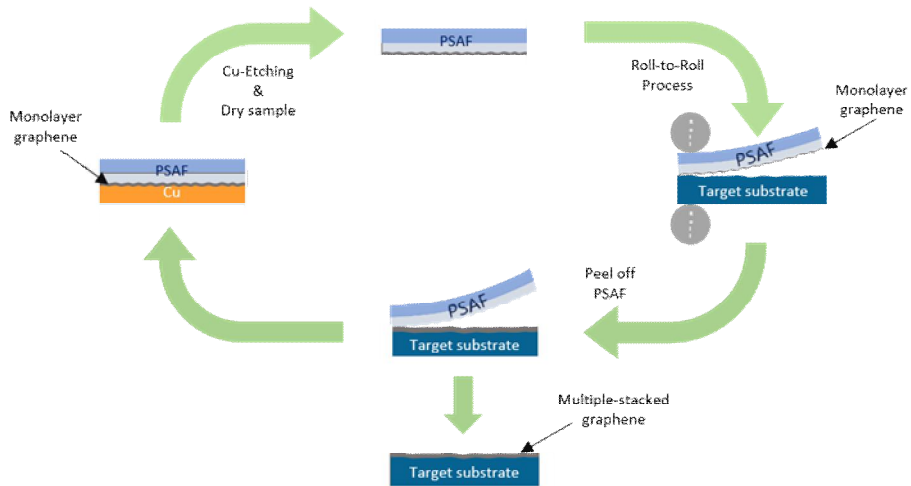


Figure 10. A schematic illustration of graphene stacking process through dry transfer method using PSAF. First, graphene covered by PSAF on copper was etched to remove metal catalyst and dried. After the roll-to-roll process, PSAF was peeled off. Through this process reputation on target substrate, multiple layers graphene film was produced.

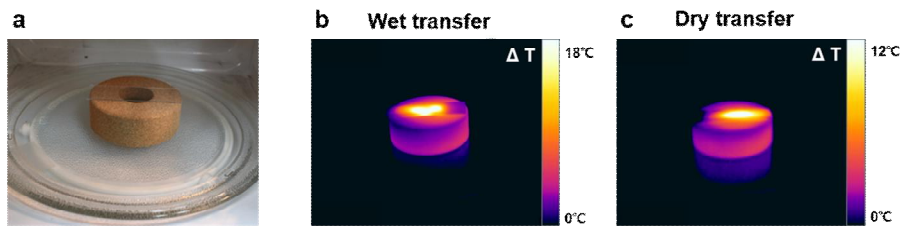


Figure 11. Comparison of heat generation between dry transfer and wet transfer. (a) An actual image of graphene films transferred on a slide glass. (b,c) Infrared images of graphene heater applying microwave during 10second transferred by wet transfer and dry transfer, respectively.

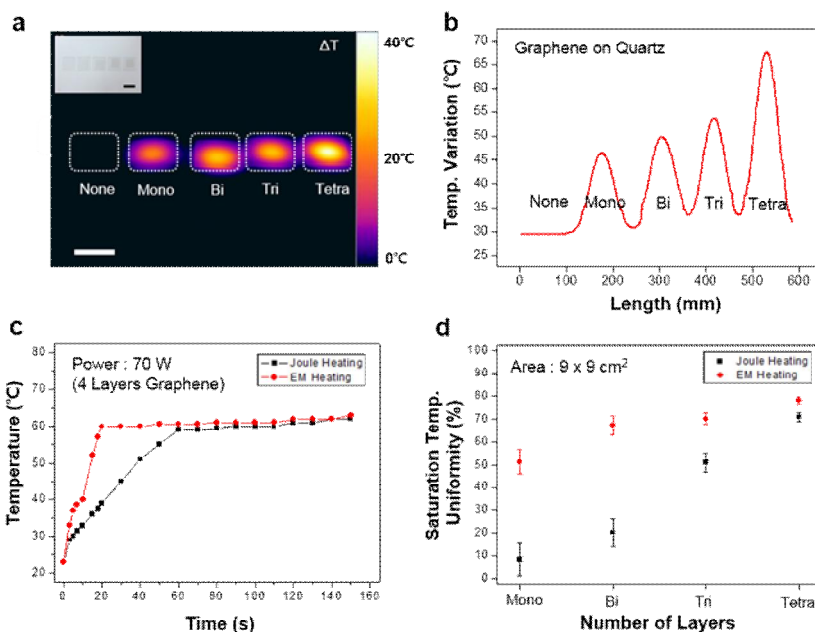


Figure 12. The graphene films transferred on target substrates.

(a) An infrared scanning of the graphene heater transferred on quartz, while applying microwave during 10 seconds. The insets show an actual image of the graphene film. Scale bars, 1 cm. (b) The temperature variation of graphene heater transferred on target substrates. (c) Temperature profile comparison of Joule heating and EM heating at power 70 W on 4 layers of graphene films. (d) Saturation temperature uniformity of Joule heating and EM heating depending on number of graphene layers.

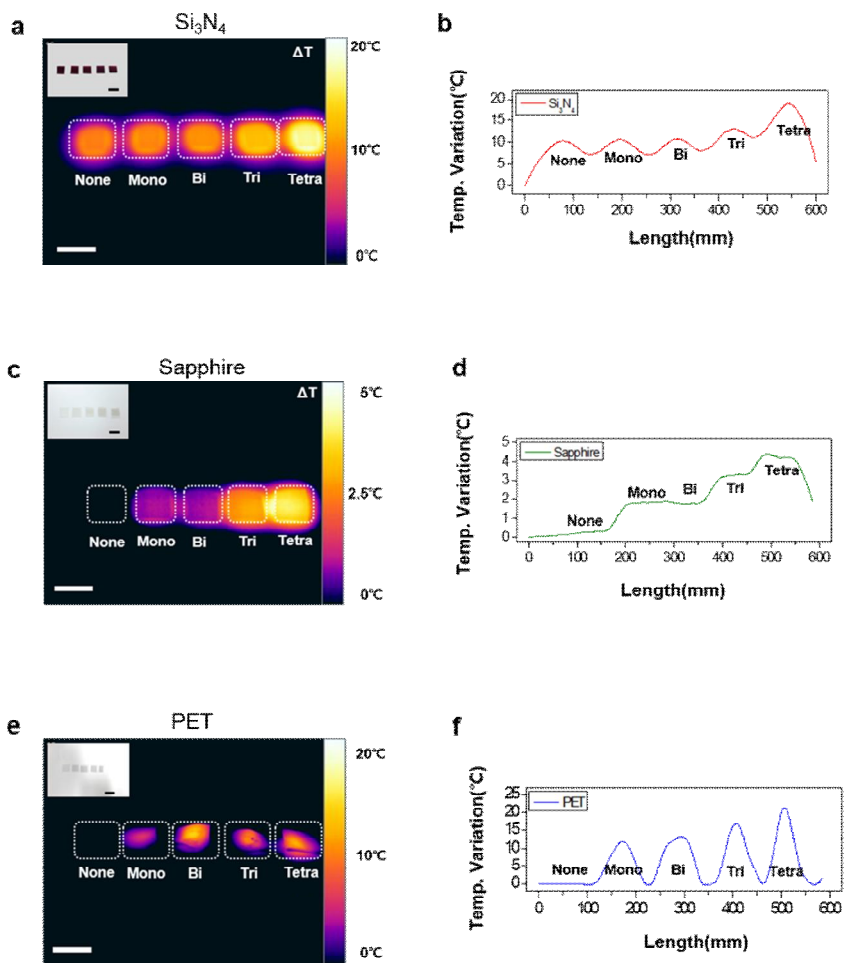


Figure 13. Comparison of graphene heater transferred on various substrates. (a,c,e) Infrared scanning images of the graphene heaters transferred on Si_3N_4 , PET, sapphire and Si wafers, respectively. The inset images are actual images. Scale bars are all the same, 1 cm. (b,d,f) Temperature variation of graphene films depending of stacking layers transferred on each substrates.

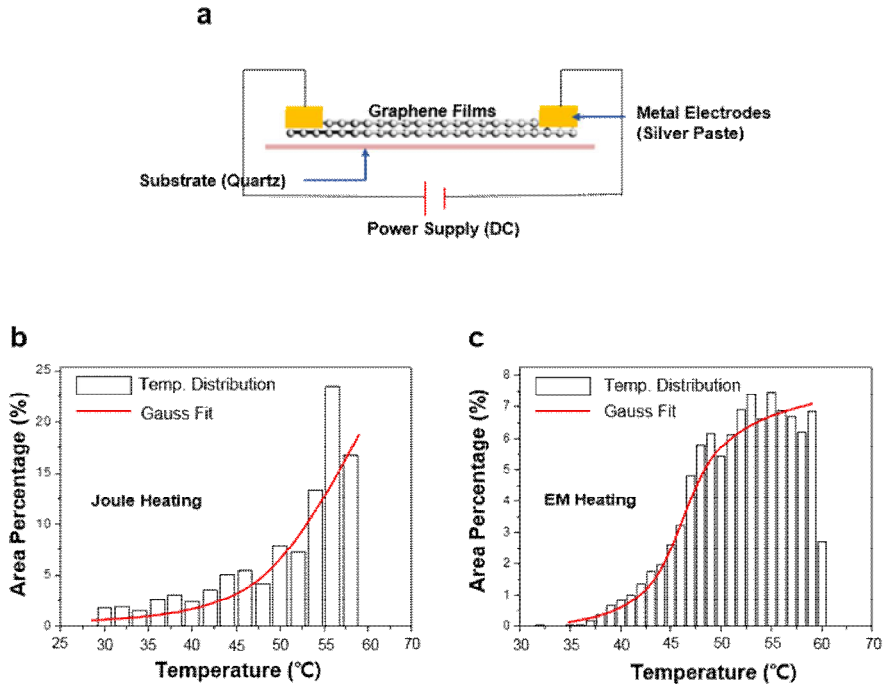


Figure 14. Comparison of Joule heating and EM heating. (a) A schematic structure of conventional Joule heating based graphene heater. (b) Temperature distribution of Joule–heating based heater made of 4 layers graphene films working at power 70 W. (c) Temperature distribution of EM–heating based heater made of 4 layers graphene films working at power 70 W. Samples shown for saturation temperature uniformity in Figure 5d were measured with the same methods indicated in Figure 7b, c.

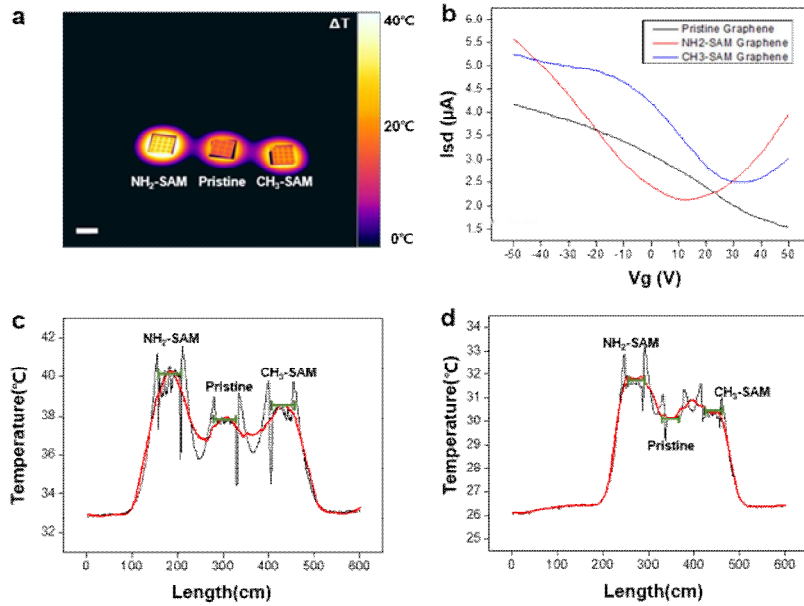


Figure 15. The heat distribution depending on charge mobility.

(a) An infrared scanning of graphene heaters on SAMs irradiated by microwave during 10 seconds. Scale bar, 1 cm.

(b) FET characteristics of graphene films depending on kinds of SAMs. (c) The temperature variation immediately measured after device fabrication. (d) The temperature variation measured after 7 days and annealing process.



Figure 16. Optical and IR photographs showing the EM-induced defogging of graphene coated vials. (a) The photograph before applying EM waves. Left is the graphene-coated bottle and right is the none-coated bottle. (b) The photograph after applying microwave during 5 seconds. (c) An infrared picture immediately obtained after microwave irradiation. Scale bars, 1 cm.

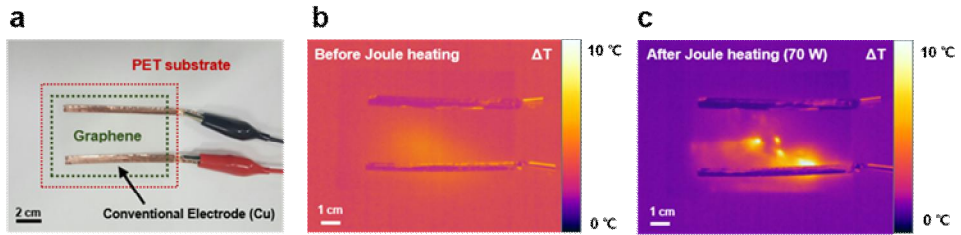


Figure 17. Optical and IR photographs showing the Joule heating process. (a) The photograph before applying Joule heating. The monolayer graphene film is transferred on PET films. Scale bars, 2cm. (b) An infrared picture before applying Joule heating. (c) An infrared picture after applying Joule heating at saturated temperature using 70 W power. Scale bars, 1 cm.

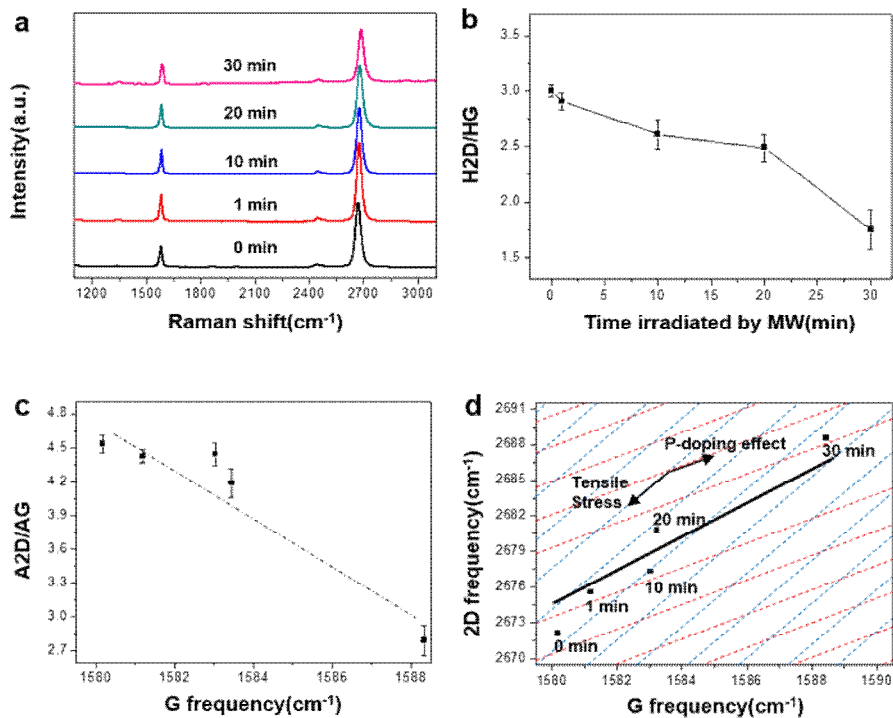


Figure 18. Raman spectra characteristics of the graphene heater by EM waves. (a) Variation of the G and 2D bands with irradiation time. (b) H2D/HG as functions of irradiation time. (c) A2D/AG as a function of the G peak shift. A2D and AG are the integral value of 2D peak and G peak respectively. (d) Position of the 2D peak as a function of the G peak shift (red line: p-doping effect, blue line: tensile/compressive stress following the arrow).

2.1.4. Conclusion

In conclusion, we have successfully demonstrated a graphene-based heater which can be triggered by EM waves and proved the mechanism of heat generation. We found that EM wave absorption phenomena is related to the diamagnetic properties of the graphene, which was confirmed by the heating efficiency that is inversely proportional to the electron mobility of graphene. The temperature response and heat distribution results show that the performance of EM waves-based heater is superior to that of the conventional Joule heating-based heaters. In particular, the EM-based graphene heaters can be easily fabricated without the additional equipment such as electrode and electric wires. Therefore, this allows graphene heater to be used widely in fields of automobile defogging/deicing systems, smart heating windows and EM-wave detecting sensors.

2.1.5. References

1. Novoselov, K. S.; Geim, A. K.; Morozov, S. V.; Jiang, D.; Zhang, Y.; Dubonos, S. V.; Grigorieva, I. V.; Firsov, A. A. *Science* **2004**, 306, 666.
2. Geim, A. K.; Novoselov, K. S. *Nat. Mater.* **2007**, 6, 183.
3. Bolotin, K. I.; Sikes, K. J.; Jiang, Z.; Klima, M.; Fudenberg, G.; Hone, J.; Kim, P.; Stormer, H. L. *Solid State Comm.* **2008**, 146, 351.
4. Lee, C.; Wei, X. D.; Kysar, J. W.; Hone, J. *Science* **2008**, 321, 385.
5. Lee, Y.; Bae, S.; Jang, H.; Jang, S.; Zhu, S. E.; Sim, S. H.; Song, Y. I.; Hong, B. H.; Ahn, J. H. *Nano Lett.* **2010**, 10, 490.
6. Bao, Q. L.; Loh, K. P. *ACS Nano* **2012**, 6, 3677.
7. Kim, Y. D.; Kim, H.; Cho, Y.; Ryoo, J. H.; Park, C. H.; Kim, P.; Kim, Y. S.; Lee, S.; Li, Y. L.; Park, S. N.; Yoo, Y. S.; Yoon, D.; Dorgan, V. E.; Pop, E.; Heinz, T. F.; Hone, J.; Chun, S. H.; Cheong, H.; Lee, S. W.; Bae, M. H.; Park, Y. D. *Nat. Nanotech.* **2015**, 10, 676.
8. Elias, D. C.; Nair, R. R.; Mohiuddin, T. M. G.; Morozov, S.

- V.; Blake, P.; Halsall, M. P.; Ferrari, A. C.; Boukhvalov, D. W.; Katsnelson, M. I.; Geim, A. K.; Novoselov, K. S. *Science* **2009**, 323, 610.
9. Wang, X. R.; Li, X. L.; Zhang, L.; Yoon, Y.; Weber, P. K.; Wang, H. L.; Guo, J.; Dai, H. J. *Science* **2009**, 324, 768.
10. Seol, J. H.; Jo, I.; Moore, A. L.; Lindsay, L.; Aitken, Z. H.; Pettes, M. T.; Li, X. S.; Yao, Z.; Huang, R.; Broido, D.; Mingo, N.; Ruoff, R. S.; Shi, L. *Science* **2010**, 328, 213.
11. Balandin, A. A. *Nat. Mater.* **2011**, 10, 569.
12. Kim, K. S.; Zhao, Y.; Jang, H.; Lee, S. Y.; Kim, J. M.; Kim, K. S.; Ahn, J. H.; Kim, P.; Choi, J. Y.; Hong, B. H. *Nature* **2009**, 457, 706.
13. Bae, S.; Kim, H.; Lee, Y.; Xu, X. F.; Park, J. S.; Zheng, Y.; Balakrishnan, J.; Lei, T.; Kim, H. R.; Song, Y. I.; Kim, Y. J.; Kim, K. S.; Ozyilmaz, B.; Ahn, J. H.; Hong, B. H.; Iijima, S. *Nat. Nanotech.* **2010**, 5, 574.
14. Kang, J.; Kim, H.; Kim, K. S.; Lee, S. K.; Bae, S.; Ahn, J. H.; Kim, Y. J.; Choi, J. B.; Hong, B. H. *Nano Lett.* **2011**, 11, 5154.
15. Kumar, A.; Zhou, C. W. *ACS Nano* **2010**, 4, 11.

16. Hecht, D. S.; Hu, L. B.; Irvin, G. *Adv. Mater.* **2011**, *23*, 1482.
17. Yoon, Y. H.; Song, J. W.; Kim, D.; Kim, J.; Park, J. K.; Oh, S. K.; Han, C. S. *Adv. Mater.* **2007**, *19*, 4284.
18. De, S.; Coleman, J. N. *ACS Nano* **2010**, *4*, 2713.
19. Xia, F. N.; Perebeinos, V.; Lin, Y. M.; Wu, Y. Q.; Avouris, P. *Nat, Nanotech*, **2011**, *6*, 179.
20. Hong, S. K.; Kim, K. Y.; Kim, T. Y.; Kim, J. H.; Park, S. W.; Kim, J. H.; Cho, B. J. *Nanotechnology* **2012**, *23*, 455704.
21. Levendorf, M. P.; Ruiz–Vargas, C. S.; Garg, S.; Park, J. *Nano Lett*, **2009**, *9*, 4479.
22. Kim, S. J.; Choi, T.; Lee, B.; Lee, S.; Choi, K.; Park, J. B.; Yoo, J. M.; Choi, Y. S.; Ryu, J.; Kim, P.; Hone, J.; Hong, B. H. *Nano Lett.* **2015**, *15*, 3236.
23. Kim, K. H.; Cho, K. M.; Kim, D. W.; Kim, S. J.; Choi, J.; Bae, S. J.; Park, S.; Jung, H. T. *ACS Appl. Mater. Interfaces* **2016**, *8*, 5556
24. Park, J.; Lee, W. H.; Huh, S.; Sim, S. H.; Kim, S. B.; Cho, K.; Hong, B. H.; Kim, K. S. *J Phys. Chem. Lett.* **2011**, *2*, 841.

25. Lee, W. H.; Park, J.; Kim, Y.; Kim, K. S.; Hong, B. H.; Cho, K. *Adv. Mater.* **2011**, *23*, 3460.
26. Kim, Y.; Cho, D. H.; Ryu, S.; Lee, C. *Carbon* **2014**, *67*, 673.

2.2. Smart contact lenses with graphene coating for EMI shielding and dehydration protection

2.2.1. Introduction

Graphene, two dimensional hexagonal lattice structure of carbon atom, has been widely studied on various fields because of its remarkable electrical, mechanical, chemical properties since its first discovery by the mechanical exfoliation of graphite crystals.¹⁻⁵ Among its unique properties, outstanding electromagnetic wave absorption property and gas-impermeability have provided potentials to use graphene for electromagnetic interference (EMI) shielding and/or diffusion barriers.^{6,7} It has been reported that graphene consists of only carbon atoms is much more effective, stable, light in weight EMI shielding materials than typical metal based materials, while the use of conventional EMI shielding materials based on metallic or magnetic

materials has been limited by heavy weight and corrosion problems.⁸⁻¹⁴ The recent advances in chemical vapor deposition (CVD) growth of large-area high-quality graphene is expected to enable the practical applications of graphene in our daily lives.^{15-19, 24, 25}

Recently, with advances in electronics, micro/nanofabrication and information technology, wearable devices have been emerged and studied for the past few years. Contact lens type wearable devices also have been developed for various purposes including the diagnosis of glaucoma or diabetes by measuring intra ocular pressure or glucose composition of tears, where RF technologies using electromagnetic (EM) waves can be employed for power supply or signal.²⁰⁻²³ However, in this case, there is a possibility of low temperature burn or dehydration, because the exposure to EM waves is very continuous and close to eyes, even though electromagnetic wave interference (EMI) level generated from the device is considered relatively weak. Likewise, as a variety of wireless devices are connected to the internet of things (IoT) technologies, the exposure of our

eyes to environmental EM waves will be steadily increasing. Thus, the EMI shielding function of the smart contact lenses is of great importance. In addition, it is known that wearing contact lenses for a long period of time possibly causes dry eye syndrome, which needs to be protected by keeping eye moisture as much as possible using a diffusion barrier. We believe that the CVD graphene is a suitable material for the EMI shielding and dehydration protection of contact lenses, because it has outstanding electrical properties as well as gas-impermeability along with high optical transmittance, mechanical flexibility, and environmental stability.

2.1.2. Experimental

Sample preparation. Monolayer graphene was synthesized on a high purity Cu foil (Alfa Aesar, 99.99%) utilizing 8 inch quartz tube CVD. The Cu foil was heated up to 1000 °C for 1 hour under a 15 sccm H₂ flow, and then 150 sccm CH₄ was inserted to grow graphene over 30 min at 1000°C. Then, the furnace was rapidly cooled down to room temperature under a 15 sccm H₂ flow. For the supporting and protecting of graphene, the PMMA solution was applied onto the graphene/Cu foil by a spin-coater. The Cu foil was etched away using 0.1 M ammonium persulfate ((NH₂)₄S₂O₈) over 5 hours. After rinsed with DI water, the floating graphene layer and the PMMA support film were transferred onto the target substrate (Si wafer, PET, contact lens). Si wafer with oxidation of 300nm and commercial contact lens (INTEROJO, 1Day Clalen) were used as substrate. To make encapsulation between contact lens and vial in water vapor transmittance rate test,

we used 3M, Scotch AD6007 for the adhesive.

Fabrication of Graphene Lens with micro-LEDs. Single-layer graphene was transferred on a silicon wafer by PMMA-assisted wet-transfer. The micro-patterns of graphene (Width = 15 μm , Length = 50 ~ 200 μm) was generated by a typical photolithography process using a photoresist (AZ GXR-601, thickness = 1.5 μm). To transfer the micro-patterned graphene onto a contact lens, the PMMA supporting layer was coated on the patterned graphene again, and then, the silicon oxide layer was etched by 4 M potassium hydroxide (KOH) solution at 90 °C. After rinsing with DI water, the floating graphene layers was transferred onto a contact lens by same method mentioned above. Finally, the pre-wired micro-LEDs (0402 SMD LED Green) was connected on the patterned graphene lens by silver paste.

Characterization. Optical microscopy was performed by Nikon ECLIPSE LV100ND, and the Raman spectra were recorded by a Raman spectrometer (RM 1000-Invia, Renishaw, 514nm). The sheet resistance was measured with 4-point probe nanovoltmeter (Keithley 6221) and DASOL FPP-40K. The

current–voltage curve was measured by Agilent B2912A. We used a microwave oven of SAMSUNG Electronics (frequency = 2.45 GHz, Maximum output power = 700 W). An IR camera (FLIR T650sc) was used to monitor temperature change of samples. For the water vapor transmittance rate test, we used precision electronic scale with METTLER TOLEDO MS105DU. The SEM images were obtained by field–emission scanning electron microscopy (FESEM, AURIGA Carl Zeiss).

2.2.3. Results and Discussion

Schematic working principle of the EMI shielding graphene contact lenses is shown in Figure 19a~d. Without graphene, the electromagnetic (EM) wave passes through the contact lens and directly absorbed by eyeballs, possibly causing a thermal damage potentially related to cataracts. In the case of using graphene, the EM wave is partially absorbed by the graphene layer on the contact lens, which reduces the EM energy delivered to the inner eyeballs (Figure 19a, b). When wearing contact lenses, tears play a role as lubricant, but the dehydration of the eyes may cause xerophthalmia (Figure 19c). The dehydration process can be prolonged by the graphene coating (Figure 19d).

Reliable graphene coating on the contact lens with a thin and soft hemispherical feature is a key for the experiment. For the conformal and durable coating of graphene on the lens, we used a template with same radius curvature of a contact

lens. Overall fabrication processes are shown in Figure 19e. We synthesized the continuous monolayer graphene on a high purity Cu foil (99.99 %) using a typical chemical vapor deposition method with flowing 150 sccm methane and 15 sccm hydrogen gases at 1,000 °C in an 8-inch quartz tube, followed by coating with PMMA.¹⁶ After etching away the Cu foil with 0.1 M ammonium persulfate ((NH₂)₄S₂O₈) aqueous solution and rinsing graphene in DI water, PMMA/Graphene was transferred on contact lens naturally attached on the template by surface tension of lens, steadily maintaining its feature during transfer process. After baking for 30 minutes at 80 °C on a hot plate, the PMMA was removed by acetone. Here, the contact lens can be protected from acetone by the graphene layer on top. Finally, the graphene coating on the contact lens is completed by isolating the lens from the template using a sharp tip.

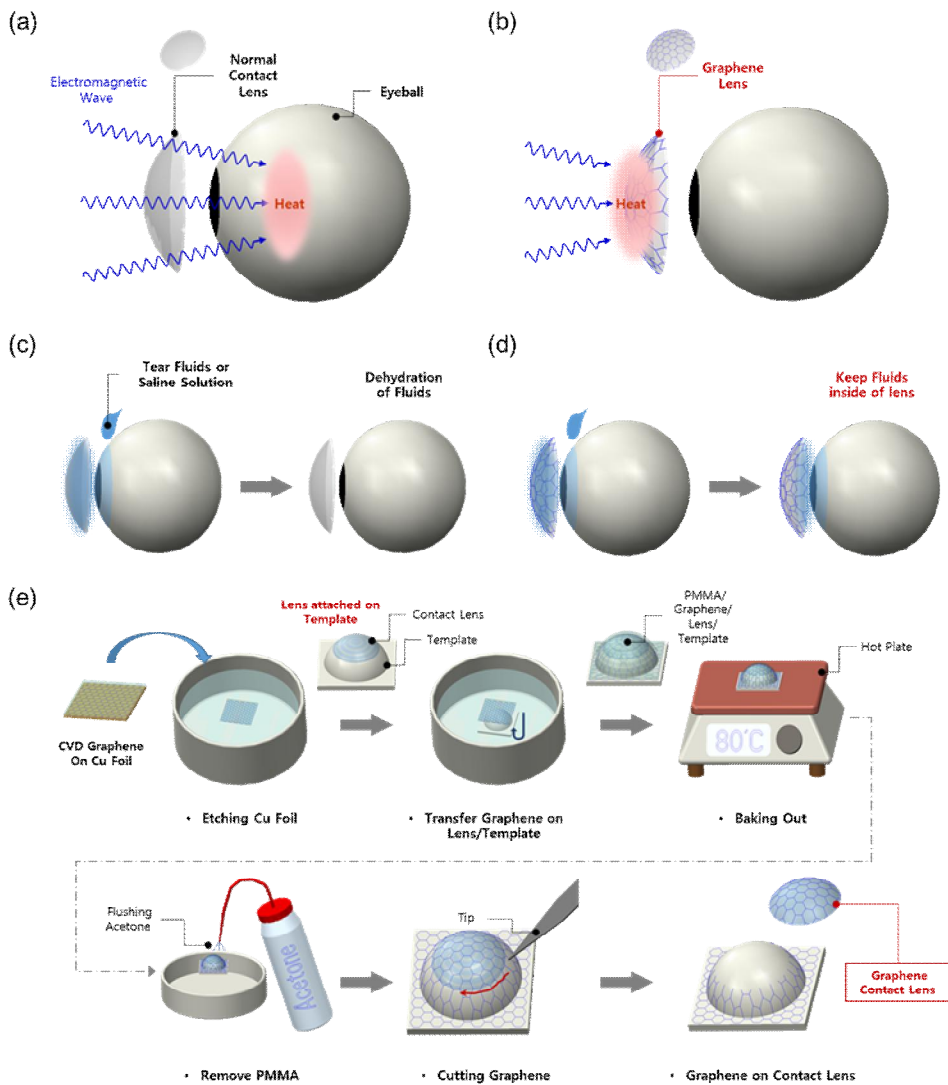


Figure 19. Schematic working principle of a graphene-coated contact lens and its fabrication process. (a) Electromagnetic (EM) wave passes through contact lens and absorbed by an eyeball, possibly causing heat damage inside. (b) EM energy

is absorbed by graphene and dissipated as a heat before reaching the interior of the eye. (c-d) Dehydration of a contact lens can be reduced due to the gas-impermeability of graphene (e) The fabrication process of the graphene-coated contact lens.

Graphene lens was being crinkled up immediately after the process because it was exposed to air during the process, proceeding dehydration of lens. However, lens had been recovered its original feature by dipping in the saline solution for a while. A slight fall-off of transmittance, assumed 2.3 % at 550 nm, was found in graphene lens comparing with normal lens, but it was hard to recognize that difference (Figure 20c), suggesting that graphene lens could give us clear vision in wearing.¹⁶ Electrical property of graphene lens has been investigated using 4 probe point measurement. PET sample coated with graphene (graphene PET) was also measured for the reference (Figure 20d). For the electrode, silver paste was formed on samples at intervals of 5 mm. To evaluate variation, 5 individual graphene lenses and 9 points in a graphene/PET sample were measured. Figure 20e is $I-V$ plot of graphene lens with the resistance range of $199 \Omega \sim 240 \Omega$, similar value with graphene PET. The sheet resistance of the graphene on the contact lens was calculated to be as low as

593 Ω/sq ($\pm 9.3\%$), as shown in Figure 20f.

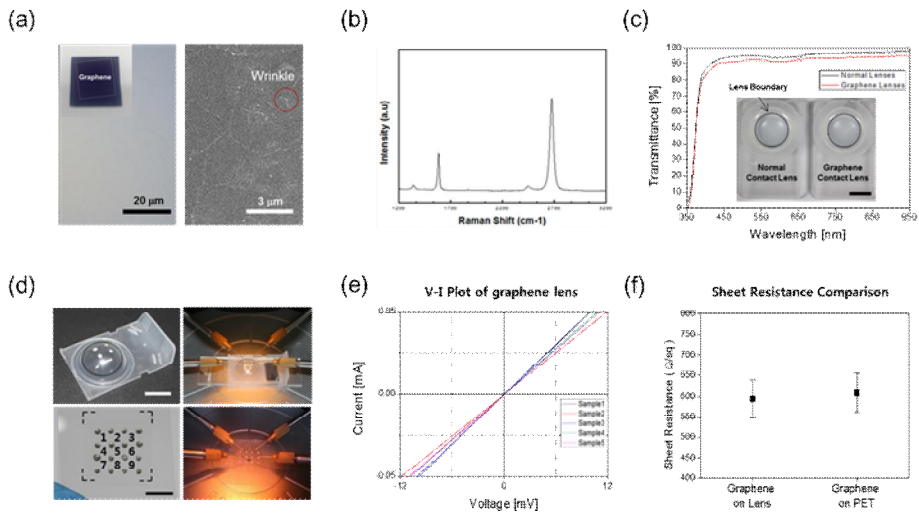


Figure 20. Optical and electrical properties of graphene films.

(a) Optical and SEM images of graphene samples transferred on a SiO₂ substrate. (b) Raman spectrum of graphene showing monolayer thickness and low defect density. (c) Transmittance of a bare contact lens and a graphene-coated contact lens. Scale bar: 1cm. (d–f) Evaluation of electrical properties of graphene samples, including 4-point sheet resistance measurement and I – V characteristics.

To confirm the actual EMI-shielding effect of the graphene-coated contact lens, we irradiated a strong EM waves (120 W for 50 sec.) on to egg whites inside a microwave oven that has similar wavelength ranges with 4G LTE and Bluetooth (2.45 GHz) as shown in Figure 21. The results show that the thermal denaturalization, *i.e.* color change of the graphene-protected egg is considerably less than the case without graphene that protects EM waves.¹⁰

When the graphene is exposed to EM waves, the electrons in orbital motion induce oscillating magnetic moments in response to external magnetic field, which efficiently absorbs the EM energy and dissipates it as thermal energy. Therefore, the EM absorption efficiency can be evaluated by monitoring the heat generation from the graphene-coated contact lens. An IR camera was used to get thermal infrared images after applying EM radiation (120 W) on the samples inside a microwave oven for 20 seconds (Figure 21c). The results show that the temperature of the graphene-coated contact lens was rapidly increased above

~45 °C, while the normal lens remained almost unchanged.

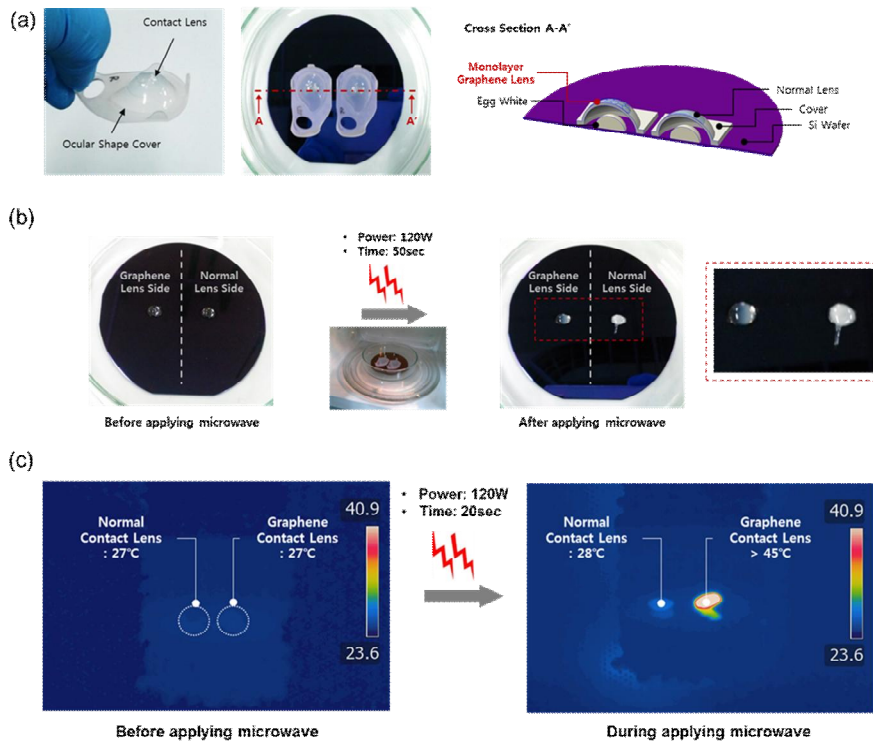


Figure 21. EMI shielding effect of the graphene-coated contact lens tested in a microwave oven. (a) Sample preparation for the microwave oven test. Egg whites on a Si wafer are covered with the contact lenses with and without graphene coating, respectively. (b) A microwave oven test showing the excellent EMI shielding effect of the graphene-coated contact lens. The egg white protected by graphene shows less thermal denaturalization. (c) IR camera images showing the elevated temperature of the graphene-coated lens inside a microwave oven, indicating the EM energy is efficiently

absorbed and dissipated as heat.

To demonstrate the dehydration protection of graphene lens, we measured the water vaporization rate of water-filled vials capped with the contact lenses. The vial samples were placed on a hot plate at 38 °C, and the mass loss was measured on an electronic scale (Figure 22).⁶ After 7 days, the weights of the normal and graphene-coated lenses were decreased by 0.8268 g and 0.5535 g, respectively (Figure 22c). The water vapor transmission rates (WVTRs) were estimated by considering the size of the lens, which has been reduced by 30 % (Figure 22d). We expect that the further improvement can be made by minimizing the defects on graphene during transfer and fabrication processes or by stacking multilayers of graphene.⁷

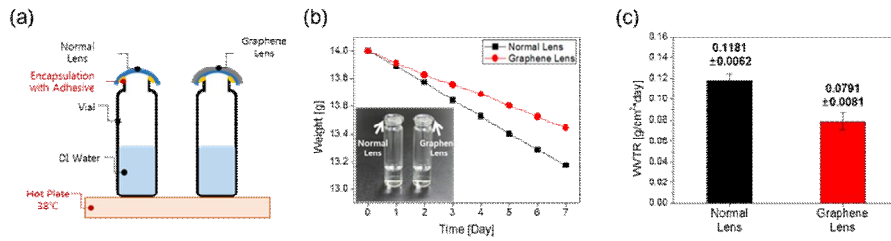


Figure 22. Enhanced dehydration protection by a graphene coated contact lens. (a) Schematic of the experimental setup to measure the water evaporation rate through contact lenses. (b) Weight loss measured with time on a hot plate at 38°C. (c) Water vapor transmission rate (WVTR) values of the contact lenses without and with graphene coating, derived from (b). The dehydration protection performance has been enhanced by ~30%.

Finally, we demonstrated a simple micro-scale light emitting diode (LED) device fabricated on a contact lens with graphene electrodes. Figure 23a shows the fabrication processes of graphene electrodes by a conventional photolithography techniques.²⁴⁻²⁵ The graphene was patterned on a SiO₂ substrate and transferred onto a contact lens by using PMMA as a supporting layer (Figure 23b, c). The negligible I(D)/I(G) ratio in Raman spectra indicate that no defect has been generated after patterning and transfer (Figure 23e). No meaningful change has been observed for high level EM exposure (~ 1 m from 100 W source) for more than 200 hrs. The pre-wired micro-LED was successfully working at ~ 9 V, implying that the graphene pattern on the contact lens is electrically continuous and robust enough to be used as an electrode (Figure 23g).

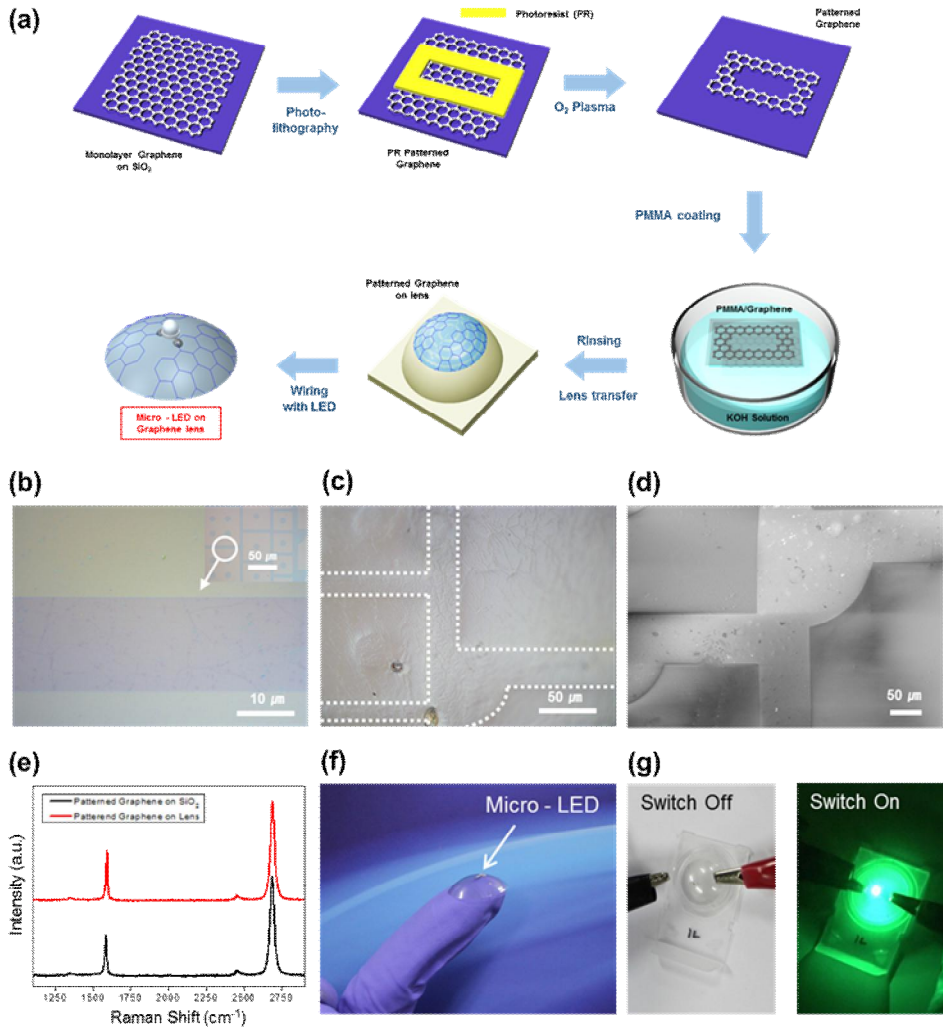


Figure 23. Demonstration of a light emitting diode (LED) fabricated on a graphene-coated contact lens with electrode patterns. (a) A schematic view of the fabrication processes including the patterning of graphene by photolithography and O_2 plasma etching. (b–c) Optical and (d) SEM images of the patterned graphene on a contact lens. (e) Raman spectra of

the patterned graphene on target substrates. (f) An assembled LED/graphene contact lens. (g) On/Off images of LED graphene lens operating voltage at 9 V.

2.2.4. Conclusion

In conclusion, we demonstrated the conformal coating of a soft contact lens with CVD graphene and its application to EMI shielding and dehydration protection. The sheet resistance of $\sim 593 \text{ } \Omega/\text{sq.}$ and the LED operation at 9 V indicate that the electrical properties of graphene can be maintained even after transfer and patterning. The EM wave shielding function of the graphene-coated contact lens was tested on egg whites exposed to strong EM waves inside a microwave oven. The results show that the EM energy absorbed by the graphene is released in the form of thermal radiation so that the damage on the egg whites can be minimized. We also demonstrated the enhanced dehydration protection effect of the graphene-coated lens by monitoring the change in water evaporation rate from the vial capped with the contact lens. Thus, we believe that the graphene-coated contact lens would provide a healthcare and bionic platform for wearable technologies in the future.

2.2.5. References

1. Novoselov, K. S.; Geim, A. K.; Morozov, S. V.; Jiang, D.; Zhang, Y.; Dubonos, S. V.; Grigorieva, I. V.; Firsov, A. A. *Science* **2004**, 306, 666–669.
2. Geim, A. K.; Novoselov, K. S. *Nat. Mater.* **2007**, 6, 183–191.
3. Bolotin, K. I.; Sikes, K. J.; Jiang, Z.; Klima, M.; Fudenberg, G.; Hone, J.; Kim, P.; Stormer, H. L. *Solid State Commun.* **2008**, 146, 351–355.
4. Lee, C.; Wei, X.; Kysar, J. W.; Hone, J. Measurement of the Elastic Properties and Intrinsic Strength of Monolayer Graphene. *Science* **2008**, 321, 385–388.
5. Bunch, J. S.; Verbridge, S. S.; Alden, J. S.; van der Zande, A. M.; Parpia, J. M.; Craighead, H. G.; McEuen, P. L. *Nano Lett.* **2008**, 8, 2458–2462.
6. Nair, R. R.; Wu, H. A.; Jayaram, P. N.; Grigorieva, I. V.; Geim, A. K. *Science* **2012**, 335, 442–444.
7. Choi, K.; Nam, S.; Lee, Y.; Lee, M.; Jang, J.; Kim, S. J.;

- Jeong, Y. J.; Kim, H.; Bae, S.; Yoo, J.-B.; Cho, S. M.; Choi, J.-B.; Chung, H. K.; Ahn, J.-H.; Park, C. E.; Hong, B. H. *ACS Nano* **2015**, 9, 5818–5824.
8. Chung, D. D. L. *Carbon* **2001**, 39, (2), 279–285.
9. Chung, D. D. L. *J. Mater. Eng. Perform.* **2000**, 9, 350–354.
10. Hong, S. K.; Kim, K. Y.; Kim, T. Y.; Kim, J. H.; Park, S. W.; Kim, J. H.; Cho, B. J. *Nanotechnology* **2012**, 23, 455704.
11. Liang, J.; Wang, Y.; Huang, Y.; Ma, Y.; Liu, Z.; Cai, J.; Zhang, C.; Gao, H.; Chen, Y. *Carbon* **2009**, 47, 922–925.
12. Chen, Z.; Xu, C.; Ma, C.; Ren, W.; Cheng, H. M. *Adv. Mater.* **2013**, 25, 1296–1300.
13. Wang, C.; Han, X.; Xu, P.; Zhang, X.; Du, Y.; Hu, S.; Wang, J.; Wang, X. *Appl. Phys. Lett.* **2011**, 98, 072906.
14. Cao, M.-S.; Wang, X.-X.; Cao, W.-Q.; Yuan, J. *J. Mater. Chem. C* **2015**, 3, 6589–6599.
15. Kim, K. S.; Zhao, Y.; Jang, H.; Lee, S. Y.; Kim, J. M.; Kim, K. S.; Ahn, J. H.; Kim, P.; Choi, J. Y.; Hong, B. H. *Nature* **2009**, 457, 706–710.
16. Bae, S.; Kim, H.; Lee, Y.; Xu, X.; Park, J. S.; Zheng, Y.; Balakrishnan, J.; Lei, T.; Kim, H. R.; Song, Y. I.; Kim, Y. J.;

- Kim, K. S.; Ozyilmaz, B.; Ahn, J. H.; Hong, B. H.; Iijima, S.
Nat. Nanotechnol. **2010**, 5, 574–578.
17. Bae, S.; Kim, S. J.; Shin, D.; Ahn, J.-H.; Hong, B. H.
Physica Scripta **2012**, T146, 014024.
18. Han, T.-H.; Lee, Y.; Choi, M.-R.; Woo, S.-H.; Bae, S.-H.;
Hong, B. H.; Ahn, J.-H.; Lee, T.-W. *Nat. Photonics* **2012**,
6, 105–110.
19. Kang, J.; Kim, H.; Kim, K. S.; Lee, S. K.; Bae, S.; Ahn, J.
H.; Kim, Y. J.; Choi, J. B.; Hong, B. H. *Nano Lett.* **2011**, 11,
5154–5158.
20. Leonardi, M.; Pitchon, E. M.; Bertsch, A.; Renaud, P.;
Mermoud, A. *Acta Ophthalmol.* **2009**, 87, 433–437.
21. Yao, H.; Shum, A. J.; Cowan, M.; Lahdesmaki, I.; Parviz, B.
A. Biosens. Bioelectron. **2011**, 26, 3290–3296.
22. Chen, G.-Z.; Chan, I.-S.; Lam, D. C. C. *Sens. Actuators A:*
Phys. **2013**, 203, 112–118.
23. Farandos, N. M.; Yetisen, A. K.; Monteiro, M. J.; Lowe, C.
R.; Yun, S. H. *Adv. Healthc. Mater.* **2015**, 4, 792–810.
24. Park, J. U.; Nam, S. W.; Lee, M. S.; Lieber, C. M. *Nat.*
Mater. **2012**, 11, 120–125.

25. Lee, M. S.; Lee, K.; Kim, S. Y.; Lee, H.; Park, J.; Choi, K. H.; Kim, H. K.; Kim, D. G.; Lee, D. Y.; Nam, S. W., Park, J. U. *Nano Lett.* **2013**, 13, 2814–2821.

Chapter 3. *Electrochemical application of graphene and beyond graphene materials*

3.1. Roll-to-roll laser-printed graphene-graphitic carbon electrodes for high performance supercapacitors

3.1.1. Introduction

Recently, there have been intensive studies on the large-area fabrication of various patterned electrodes essential for flexible displays^{1,2}, chemical sensors³, transparent heaters^{4,5}, *etc.* In particular, flexible energy devices require various patterning techniques with different shapes^{6,7}, for example, to fabricate supercapacitor electrodes with uniform finger distances and larger surface areas for higher efficiency.⁸ However, conventional patterning methods based on the use of pre-patterned masks^{9,10} or complicated lithography techniques¹¹ are costly and time-consuming. On the other

hand, a laser printing technique is expected to provide a very simple and cheap route to generate various patterns, but it has not been utilized for the fabrication of energy or display electrodes.

Carbon materials have been widely used in modern technologies,¹²⁻¹⁴ and among them, graphene has been most studied as an electrode material particularly useful for energy storage applications^{15,16} thanks to its large surface area (theoretically 2,630 m²/g)¹⁶, high electrical mobility (~ 14,000 cm²/Vs)¹⁷, mechanical flexibility (Young's modulus ~ 1 TPa)¹⁸ and superior chemical stability.¹⁹ Electro-spraying²⁰ and laser-scribing in a DVD writer^{21,22} were used to pattern the graphene-like materials, but the size and speed of fabrication has been limited for practical applications. Ink-jet printing enabled the large-area fabrication of carbon electrodes.^{23,24} However, it is very hard to prepare printable graphene-based ink materials with uniform size and dispersion. Otherwise, a residual deposition on the nozzle disturbs a delicate patterning and often results in the blockage of nozzles. Thus, we present a new strategy to fabricate

graphene-graphitic carbon-based supercapacitors using a commercially available standard laser printer and its toner material as a carbon source in a continuous way. This roll-to-roll process enables a quick fabrication of densely patterned supercapacitor electrodes on a large-area substrate with a flexible and scalable design by simple printing software. The fabricated supercapacitor devices are expected to exhibit high performance with outstanding mechanical flexibility and chemical stability.

3.1.2. Experimental

Preparation and fabrication of graphene-graphitic carbon supercapacitors. Patterned graphene-graphitic carbon supercapacitors were produced by the direct laser writing using a consumer-grade standard laser printer and toner (FUJI XEROX CP405 d). High purity copper foils (Alfa Aesar, 99.999%) were used instead of conventional papers. The patterned carbon powder on the copper foils was placed in the cold zone of annealing chamber flowing with flowing 50 sccm H₂ and 500 sccm Ar gas. When the centre of the furnace reached 800 °C, the samples were moved to the hot zone of the furnace. After 30 min, the samples were left to cool down to room temperature in argon circumstance for protection gas.

Characterization and measurements. The microstructures and morphologies of laser printed patterns were investigated by field-emission scanning electron microscopy (FESEM, AURIGA Carl Zeiss) and tunneling electron microscopy (TEM, JEOL JEM-2100). The Raman spectra were obtained by a

Raman spectrometer (RM 1000–Invia, Renishaw, 514 nm). Structure bonding in the structure is analyzed by FT–IR and XPS; The FT–IR spectra were obtained by using a Thermo Scientific Nicolet 6700 spectrometer and XPS analysis was carried out with a KRATOS AXIS–HSi model in Research Institute of Advanced materials.

Electrochemical measurements. The prepared graphene–graphitic carbon on copper foil were directly adopted as an electrode without any additional treatment. Test cells were assembled in a glove box into a two–electrode configuration with a Li metal counter electrode and 1M LiPF₆ in EC/DMC (1:1 vol %) as an electrolyte. A separator of grade GF/F (Whatman, USA) was sonicated in acetone and dried 180 °C. Electrochemical profiles were obtained with a voltage range of 3 V to 0.01 V using a multichannel potentio–galvanostat (WonATech).

Characterization. An infrared camera (FLIR T650sc) was used to measure the temperature gradient of the graphene films. The sheet resistance was measured using a 4–probe with a nanovoltmeter (Keithley 6221, 2182A) and the Van der Pauw

method was applied. The electrical properties were measured by Agilent 2602. Constant 10 mV voltage was applied from source to drain during the measurement. The Raman spectra were recorded using Renishaw Invia Raman Microscope with 1mW 514nm Ar laser with the spot size of 2 μm .

3.1.3. Results and Discussion

The general laser printer toner which contains carbon powders, pigments and organic binders (except iron oxide) is injected into a clean cartridge and printed on a metallic foil (Cu or Ni) through a roll-to-roll process (Figure 24, 25). Then, the printed metallic foil is annealed in a quartz tube with flowing 150 sccm Ar and 50 sccm H₂ at 700~1,000 ° C, where the metallic surface catalyses the formation of graphene or graphitic carbon layers (Figure 26).^{25,26} We find that non-carbon impurities in pigments, organic binders and iron oxides are removed, and only carbon-based materials are obtained after the annealing (Figure 25). The synthesized graphene-graphitic carbon materials on a metallic foil can be used directly as supercapacitor electrodes without any additional process to attach binders and current collectors. It was possible to fabricate more than 500 supercapacitor electrode cells on a A4-sized metallic foil.

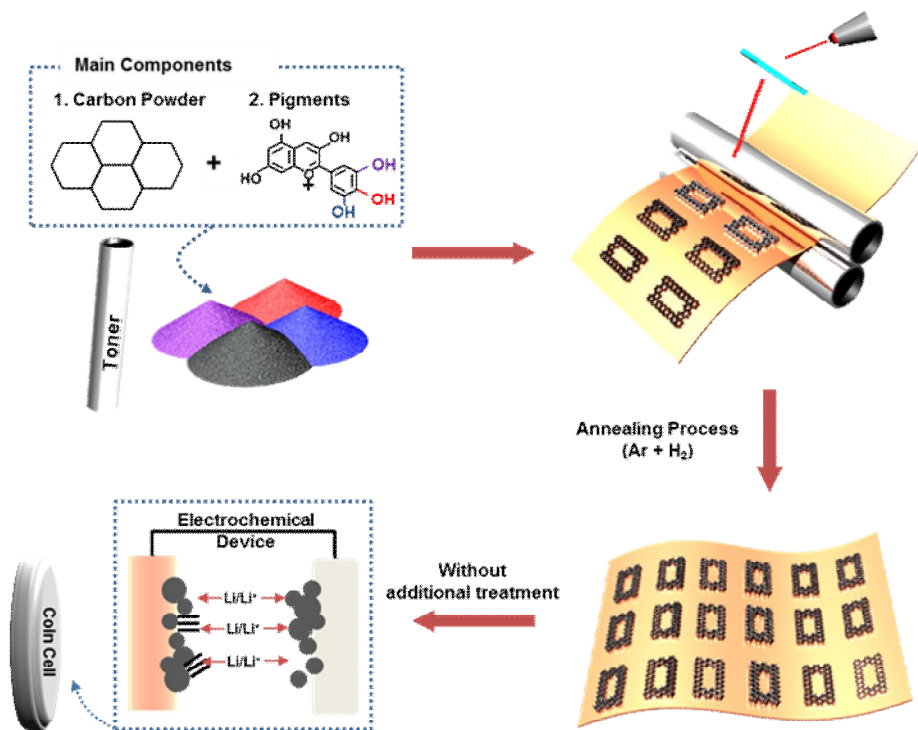


Figure 24. Schematic illustration of the synthesis process of graphene-graphitic carbon supercapacitors by a common laser printer. The laser toner powder as a carbon source is pre-patterned on a metal foil. After annealing process, the graphene-graphitic carbon films on a metal foil is directly used as supercapacitors without additional treatment.

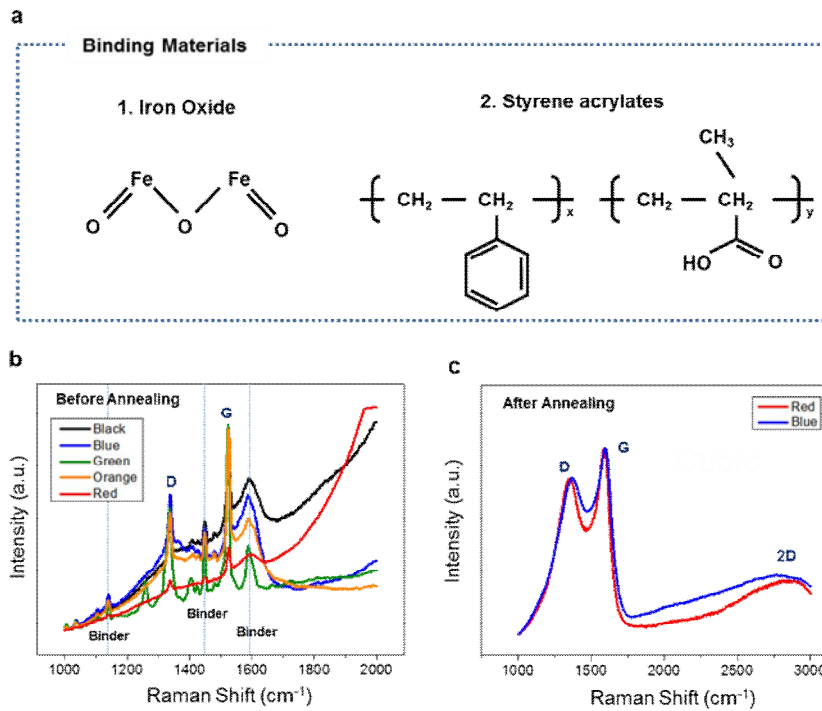


Figure 25. Binding materials in laser printing toner powders and their changes in Raman spectra before and after annealing.

(a) Molecular structures of the binding materials in the laser printing toner excluding carbon powder and pigments. (b, c) Raman spectra of the toners with different colours laser-printed on a copper foil before and after annealing process.

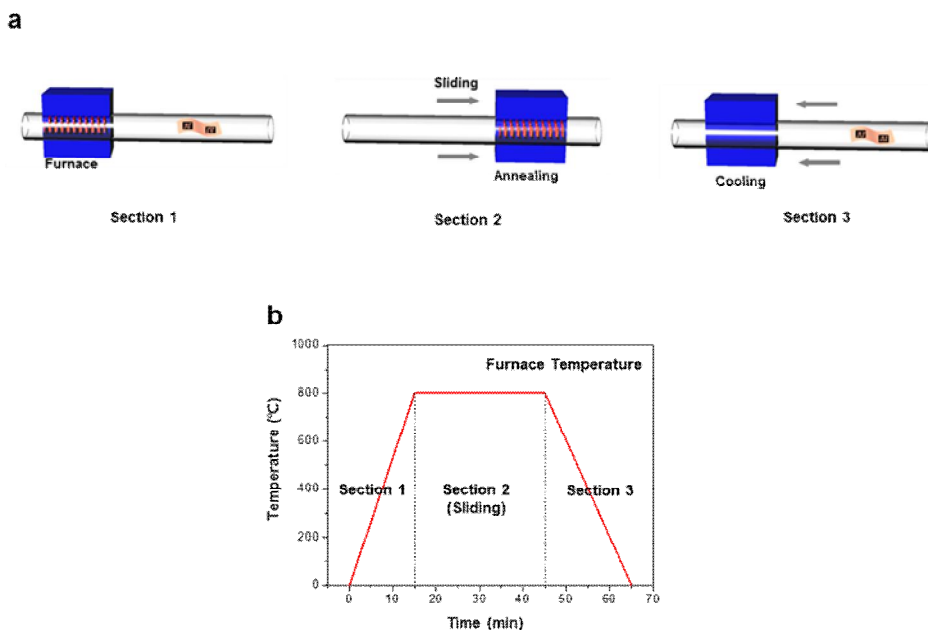


Figure 26. (a) A schematic illustration the synthesis of graphene-graphitic carbon layers. A laser-printed copper foil was placed in the cold zone of the quartz tube with flowing 50 sccm H_2 and 500 sccm Ar (section 1). When the centre of the furnace reached 800 °C, the furnace was moved to the position of the copper foil for annealing (section 2). After 30 min, the furnace was moved back to the cold zone, and the sample was rapidly cooled down to room temperature (section 3). (b) A temperature-time plot for the synthesis of graphene-graphitic carbon layers, corresponding to a.

Figure 27a shows the photographs of a copper foil with laser-printed patterns before and after annealing process, showing that continuous and well-defined graphitic carbon structures. The scanning electron microscope (SEM) images in Figure 27b shows the comparison between non-patterned and patterned carbon structures on a copper foil after annealing. We suppose that the formation of spherical particles maximizes the surface area of the carbon electrodes, which enhances electrochemical reactivity.

The cross-section SEM images in Figure 27c demonstrate that the thickness of the graphitic carbon electrode is decreased from $\sim 7\mu\text{m}$ to $\sim 4\mu\text{m}$ as the non-carbon impurities in the toner are removed at the high temperature. The transmission electron microscope (TEM) images in Figure 27d indicates that few layer graphene films are formed at the boundary between the copper foil and the graphitic carbon material, implying that the catalytic effect to form graphene layers is available near the metallic surface although the excessive carbon source exists. As a result, the graphene-graphitic carbon hybrid structures are formed. The

graphitic carbon with high surface area is advantageous for electrochemical reaction, while the graphene with strong bonding to the metallic substrate improves the chemical stability and conductivity. To demonstrate the flexibility in design, the finger electrode patterns with various scales are laser-printed and annealed as shown in Figure 27e.

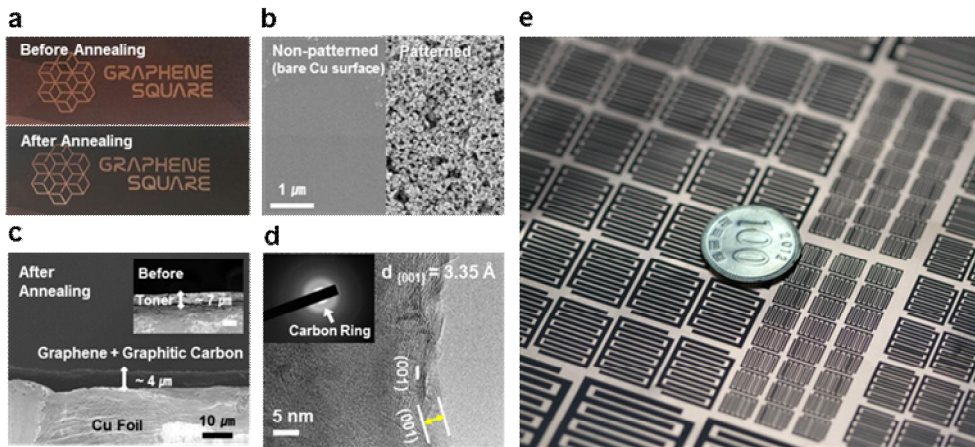


Figure 27. Optical and electrical properties of graphene films.

(a) Optical and SEM images of graphene samples transferred on a SiO₂ substrate. (b) Raman spectrum of graphene showing monolayer thickness and low defect density. (c) Transmittance of a bare contact lens and a graphene-coated contact lens. Scale bar: 1cm. (d–f) Evaluation of electrical properties of graphene samples, including 4-point sheet resistance measurement and $I-V$ characteristics.

The resulting graphene–graphitic carbon electrode has excellent adhesion property on a metallic foil even with the absence of conventional polymeric binders such as polyvinylidene fluoride (PVdF). The peeling–off and rubbing tests in Figure 28a show the excellent adhesion stability. The chemical stability of graphene–graphitic carbon electrode withstanding in (*i.e.* 1M LiPF₆ in EC/DMC and 1M LiTFSI in TEGDME) organic solvents exhibits no net weight loss. Additional chemical stability test was conducted to prove its stability in variety of solvents (Figure 29). These results show potential feasibility for electrochemical device application in multiple electrolyte settings.

The Raman analysis in Figure 28c shows a typical spectrum of carbon–based graphene materials. After the annealing process, the intensity of D and G band is considerably increased, implying that the graphitic carbon structures are formed. Furthermore, we measured transfer characteristics of FETs from graphene/graphitic carbon on SiO₂ using conventional PMMA transfer methods (Figure 30). The Dirac point demonstrate graphene–graphitic carbon

hybrid structure, as we mentioned above. The electrical properties need to be further studied and optimized through following studies. The colour of the toner powder depends on the number of hydroxyl groups in pigments and the ratio between pigments and carbon powders, which turns out to be negligible for the crystallinity and the defect density of the graphitic carbon electrodes for supercapacitors (Figure 25). Before annealing, the laser toner powder shows multiple FT-IR peaks related to the complicated structures of pigments, which is mostly disappeared during the graphitization process except C-O peaks (Figure 28d). The C 1s and O 1s peaks in the XPS spectra also indicate that the carbon layers are mostly sp^2 carbons that are slightly oxidized with stable C-O groups, which are chemically inert enough against harsh electrochemical reactions in a supercapacitor.

The same experiment is also conducted on a nickel foil to use it as a counter electrode (Figure 31). Due to the higher carbon solubility of Ni than Cu, thicker and higher-quality graphene-graphitic carbon layers are formed, which implies that a wider range of applications is possible with the laser-

printed graphene–graphitic carbon electrodes on different metal foils with enhanced catalytic and electrochemical properties.

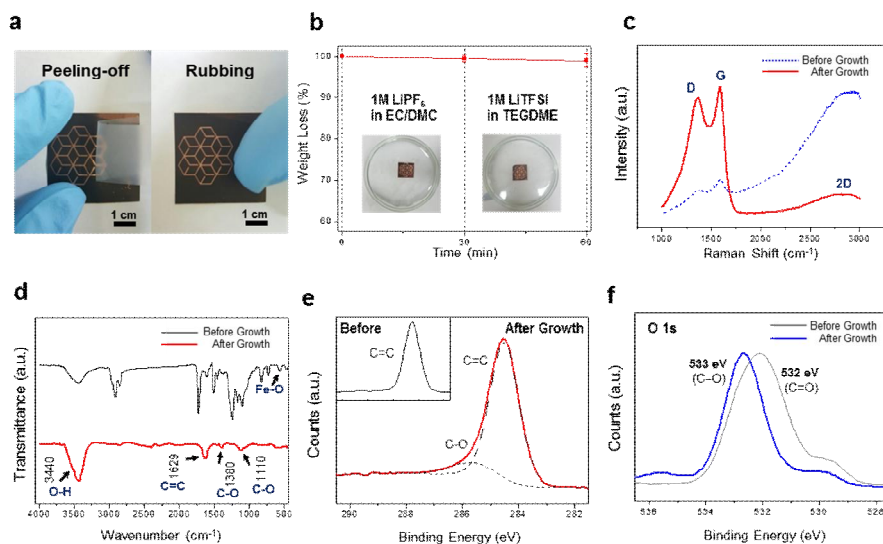


Figure 28. Mechanical, chemical stability tests and spectroscopic analyses. (a) Peeling-off test of the graphene-graphitic carbon electrodes using a commercial Scotch tape (left) and rubbing test (right). (b) Chemical stability test in organic electrolytes (1M LiPF₆ in EC/DMC and 1M LiTFSI in TEGDME). (c, d) Raman spectra and FT-IR spectra of the graphene-graphitic carbon electrodes before/after annealing. The peak at 1629 cm⁻¹ is originated from the sp² hybridization of carbon-carbon double bonding in plane stretching. (e, f) C 1s and O 1s XPS spectra before/after annealing. The O 1s peak for C=O bonding at (~532.0 eV) is shifted to the peak for C-O bonding (~533.0 eV).

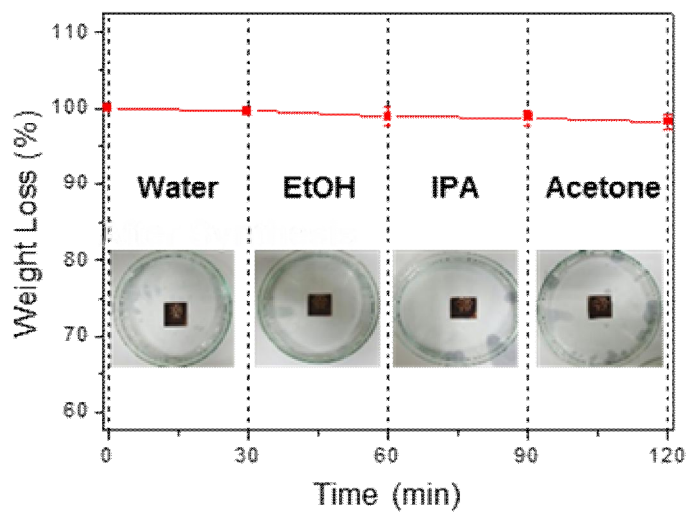


Figure 30. Chemical stability test in various solvents. Negligible weight loss in various organic solvents (i.e. water, ethanol, isopropanol, and acetone) also exhibits the excellent chemical stability of graphene-graphitic carbon electrode.

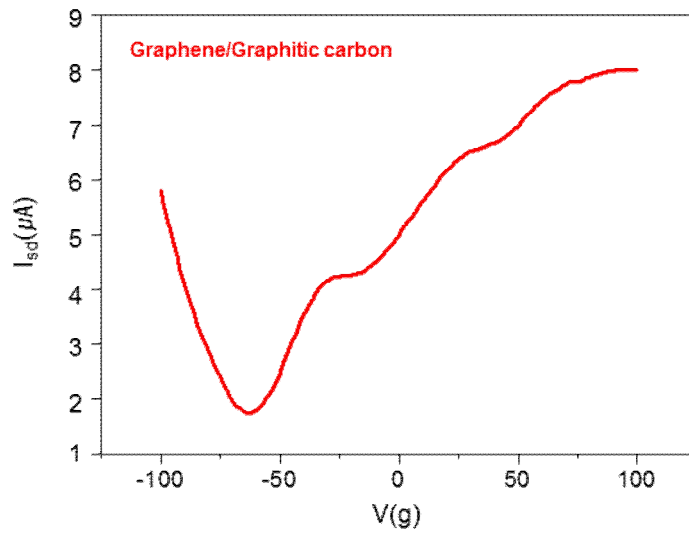


Figure 30. Transfer characteristics of graphene-graphitic carbon measured at $V_{ds} = 0.01V$. Graphene-graphitic carbon shows ambipolar behavior with a Dirac cone at $V_g \sim -50V$.

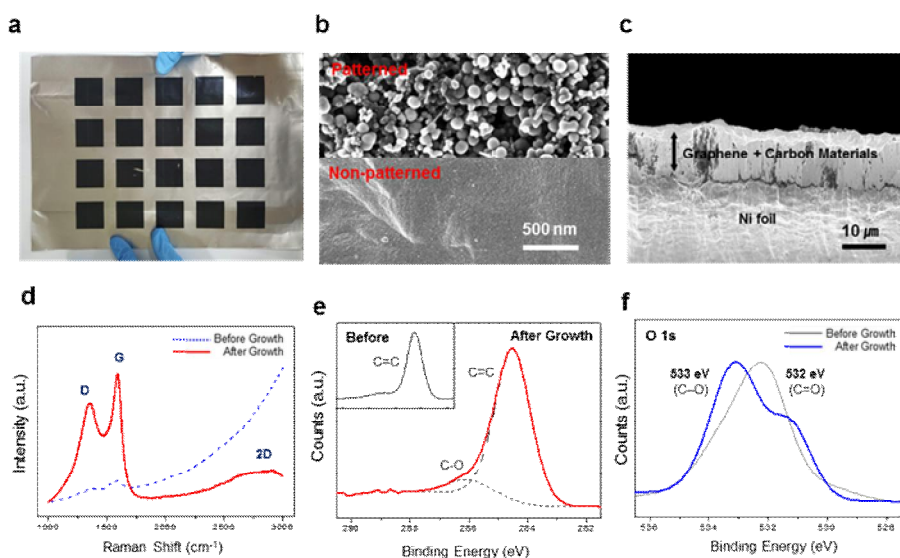


Figure 31. Microscopic and spectroscopic analyses of the graphene-graphitic carbon formed on a nickel foil. (a) A photograph of the laser-patterned graphene-graphitic carbon layers on a nickel foil after annealing process. (b) SEM images of the laser-patterned (upper) and the non-patterned area (lower) on the nickel foil after annealing. (c) A cross-sectional SEM image of the graphene-graphitic carbon film on the nickel foil after annealing. (d) Raman spectra of the graphene-graphitic carbon electrode after annealing (e,f) C 1s and O 1s XPS spectra of the laser-printed graphene-graphitic carbon electrode before/after annealing on a nickel foil.

We evaluated the electrochemical performance of synthesized graphene-graphitic carbon on copper foil as the electrode for lithium-ion cells. Note that the synthesized material was directly adopted to electrochemical cells as electrodes without any additional treatments. The galvanostatic measurement shows that the electrode exhibits a specific capacity of 100 mAh g^{-1} which is comparable to the commercial electrochemical supercapacitors such as activated carbon (Figure 32a).^{27,28} Figure 32b shows the rate performance of graphene-graphitic carbon materials, retaining approximately 55% of its capacity at the current density of 5 A g^{-1} , which corresponds to 40 seconds of charge and discharge (Figure 32c). This outstanding performance of graphene-graphitic carbon electrode excels other previously reported carbon-based supercapacitors as shown in Ragone plots (Figure 32d) in comparison with other supercapacitors such as hierarchical porous graphitic carbon²⁹, small-pore carbon³⁰, pistachio nustshell-derived microporous carbon³¹, and activated carbon³².

To better understand the energy storage mechanism of the graphene-graphitic carbon electrode, we conducted cyclic voltammetry (CV) test with various voltage scan rates (0.1–10 mV s⁻¹) (Figure 32e). Assuming that the current obeys a power-law equation as follows:

$$i = av^b$$

where i is a measured peak current, v is a voltage sweep rate, a and b are adjustable parameters.^{33,34} The b value of 1.0 generally indicates a surface-limited (capacitive) reaction whereas the b value of 0.5 represents a diffusion-controlled reaction such as intercalation.^{33,35} The CV results of graphene-graphitic carbon show two distinctive peaks at ~1.1 V vs. Li/Li⁺ and ~0.1 V vs. Li/Li⁺. When they are plotted as log(scan rate) vs. log(peak current), each peak corresponds to the slopes of 0.95 and 0.78, respectively. (Figure 32f). The values of the slope indicate that capacitive contribution is dominant in the first redox peak (~1.1 V vs. Li/Li⁺), and the following peak (~0.1 V vs. Li/Li⁺) exhibits not only capacitive

reaction but also diffusion-controlled intercalation. This CV results are consistent with the previous characterization of the material in Figure 27d, which showed that the material consists of amorphous carbon as well as crystalline graphite. Amorphous part having large surface area and defects would act as an active site for the capacitive charge storage, while the crystalline part would serve a host for Li^+ intercalation. This can also be supported by the fact that Li^+ intercalation in graphite occurs at approximately 0.1 V vs. Li/Li^+ which corresponds to the second peak position. The electrode could exhibit high stability during the operation with nearly 100% of the capacity retention after 3,000 cycles (Figure 32g). For more practical feasibility, we constructed a full cell comprised of the synthesized material as an anode and commercial activated carbon (MSP-20) as a cathode. Note that the cathode contains excessive amount of activated carbon so that the voltage of cathode was assumed to be constant during the electrochemical operation. The results show that graphene-graphitic carbon material exhibits a comparable capacity of 100 mAh g^{-1} in full cells (Figure 32h) and stably operate for

over 100 cycles (Figure 32i). Additionally, electrochemical performance of synthesized material on nickel foil was also tested, showing comparable capacity, rate capability, and cycle stability (Figure 33).

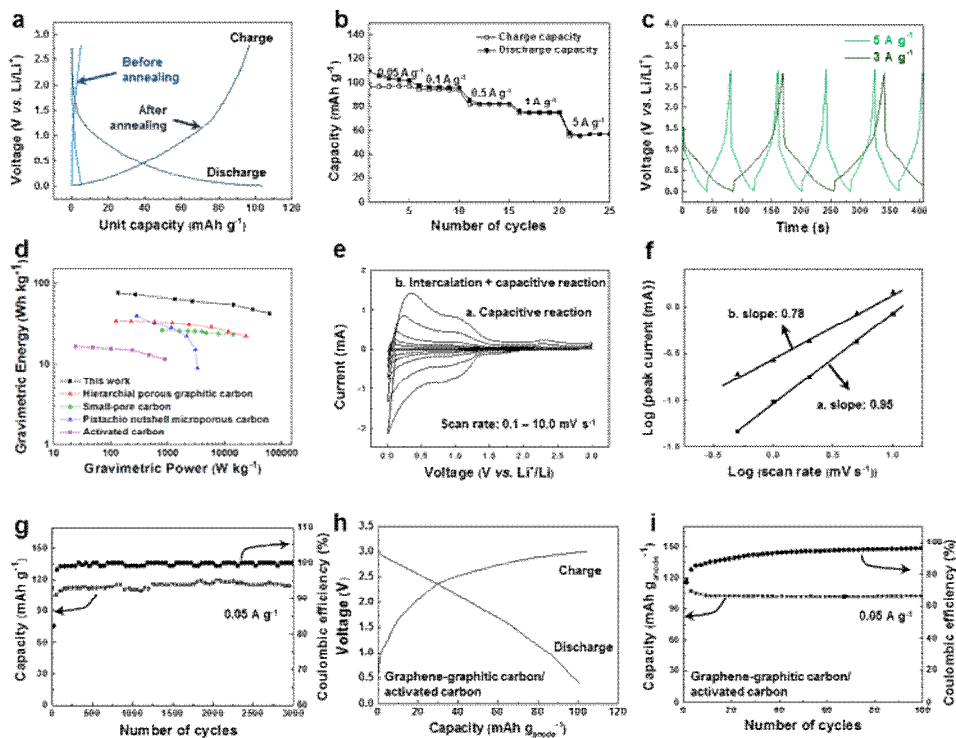


Figure 32. Electrochemical performance of graphene-graphitic carbon materials. (a) Typical charge/discharge profiles of materials before (sky blue) and after (dark blue) synthesis. (b) Charge/discharge profile with time vs. voltage. (c) Rate capability of the electrodes with current density of 0.05–5 Ag⁻¹. (d) Comparison of gravimetric power and gravimetric energy. (e) Cyclic voltammetry measurement and its plot in terms of log (scan rate) vs. log (peak current). (g) Cycle stability of the electrode. (h) Charge/discharge profile and (i) cycle stability of full cell consisting of graphene-graphitic carbon materials and activated carbon.

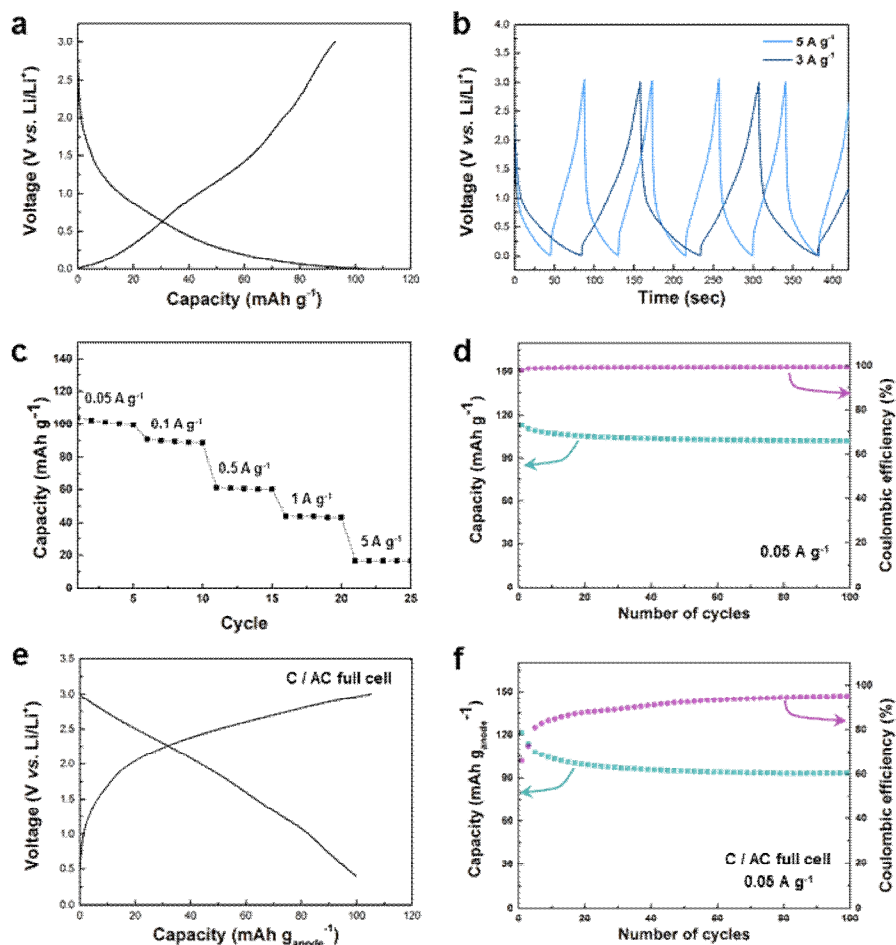


Figure 33. Electrochemical performance of the graphene-graphitic carbon materials laser-printed and annealed on a nickel foil. (a) Typical charge/discharge profiles of materials. (b) Charge/discharge profiles in time vs. Voltage. (c) Rate capability of the electrodes with current density of 0.05–5 A g⁻¹. (d) Cycle stability of the electrode. (e) Charge/discharge profiles and (f) cycle stability of full cell comprised of graphene-graphitic carbon materials and activated carbon.

3.1.4. Conclusion

The graphene-graphitic carbon materials were easily synthesized by simple printing on metal foils with the consumer-grade laser toner followed by annealing process. The new type materials look like typical printed letters, as their shapes or images are commonly found in documents. These synthesized materials were adopted as electrochemical supercapacitors and showed significantly high electrochemical performance compared to the commercial carbon materials. It is remarkable that the fabrication process described here removes the complicated lithography processes which are very expensive and time consuming, while enhancing the yield and efficiency of compactly patterned supercapacitors on the large surface. In addition, this technique enables graphene-graphitic carbon on metal foils to be used as supercapacitors without any additional treatment such as making slurry with binders, conductive additives and current collectors that are usually required in producing commercial supercapacitors. Thus, our new technique holds the key to produce low-cost

supercapacitors in a large scale for a short time. Furthermore, graphene-graphitic carbon composites show superior mechanical, chemical and cycling stability. This is notable when compared with micro-patterned electrochemical devices whose finite lifetime and instability could be major problems especially when they have to be inserted in forthcoming flexible and wearable electronics. Due to the simplicity and scalability, future studies and findings will be utilized for extending the applications of the laser printed power sources to other various storage fields such as active radio frequency identification tags, flexible electronics embedded into clothing and roll-up portable large area displays.

3.1.5. References

1. Kim, D. H.; Ahn, J. H.; Choi, W. M.; Kim, H. S.; Kim, T. H.; Song, J. Z.; Huang, Y. G. Y.; Liu, Z. J.; Lu, C.; Rogers, J. A. *Science* **2008**, 320 (5875), 507–511.
2. Sekitani, T.; Noguchi, Y.; Hata, K.; Fukushima, T.; Aida, T.; Someya, T. *Science* **2008**, 321 (5895), 1468–1472.
3. McAlpine, M. C.; Ahmad, H.; Wang, D. W.; Heath, J. R. *Nat. Mater.* **2007**, 6 (5), 379–384.
4. Yoon, Y. H.; Song, J. W.; Kim, D.; Kim, J.; Park, J. K.; Oh, S. K.; Han, C. S. *Adv. Mater.* **2007**, 19 (23), 4284–+.
5. Kang, J.; Kim, H.; Kim, K. S.; Lee, S. K.; Bae, S.; Ahn, J. H.; Kim, Y. J.; Choi, J. B.; Hong, B. H. *Nano Lett.* **2011**, 11 (12), 5154–5158.
6. Chmiola, J.; Largeot, C.; Taberna, P. L.; Simon, P.; Gogotsi, Y. *Science* **2010**, 328 (5977), 480–483.
7. Pech, D.; Brunet, M.; Durou, H.; Huang, P. H.; Mochalin, V.; Gogotsi, Y.; Taberna, P. L.; Simon, P. *Nat. Nanotech.* **2010**, 5 (9), 651–654.
8. Sung, J. H.; Kim, S. J.; Lee, K. H. *J. Power Sources* **2003**,

124 (1), 343–350.

9. Wu, Z. S.; Parvez, K.; Feng, X. L.; Mullen, K. *Nat. Comm.* **2013**, 4.
10. Niu, Z. Q.; Zhang, L.; Liu, L.; Zhu, B. W.; Dong, H. B.; Chen, X. D. *Adv. Mater.* **2013**, 25 (29), 4035–4042.
11. Pech, D.; Brunet, M.; Dinh, T. M.; Armstrong, K.; Gaudet, J.; Guay, D. *J. Power Sources* **2013**, 230, 230–235.
12. Pech, D.; Brunet, M.; Taberna, P. L.; Simon, P.; Fabre, N.; Mesnilgrete, F.; Conedera, V.; Durou, H. *J. Power Sources* **2010**, 195 (4), 1266–1269.
13. Chen, W.; Beidaghi, M.; Penmatsa, V.; Bechtold, K.; Kumari, L.; Li, W. Z.; Wang, C. L. *Ieee T. Nanotech.* **2010**, 9 (6), 734–740.
14. Heon, M.; Lofland, S.; Applegate, J.; Nolte, R.; Cortes, E.; Hettinger, J. D.; Taberna, P. L.; Simon, P.; Huang, P. H.; Brunet, M.; Gogotsi, Y. *Energy Environ. Sci.* **2011**, 4 (1), 135–138.
15. Zhu, Y. W.; Murali, S.; Stoller, M. D.; Ganesh, K. J.; Cai, W. W.; Ferreira, P. J.; Pirkle, A.; Wallace, R. M.; Cychoz, K. A.; Thommes, M.; Su, D.; Stach, E. A.; Ruoff, R. S. *Science*

- 2011, 332 (6037), 1537–1541.
16. Miller, J. R.; Outlaw, R. A.; Holloway, B. C. *Science* **2010**, 329 (5999), 1637–1639.
17. Novoselov, K. S.; Geim, A. K.; Morozov, S. V.; Jiang, D.; Zhang, Y.; Dubonos, S. V.; Grigorieva, I. V.; Firsov, A. A. *Science* **2004**, 306 (5696), 666–669.
18. Lee, C.; Wei, X. D.; Kysar, J. W.; Hone, J. *Science* **2008**, 321 (5887), 385–388.
19. Elias, D. C.; Nair, R. R.; Mohiuddin, T. M. G.; Morozov, S. V.; Blake, P.; Halsall, M. P.; Ferrari, A. C.; Boukhvalov, D. W.; Katsnelson, M. I.; Geim, A. K.; Novoselov, K. S. *Science* **2009**, 323 (5914), 610–613.
20. Beidaghi, M.; Wang, C. L. *Adv. Func. Mater.* **2012**, 22 (21), 4501–4510.
21. El-Kady, M. F.; Strong, V.; Dubin, S.; Kaner, R. B. *Science* **2012**, 335 (6074), 1326–1330.
22. El-Kady, M. F.; Kaner, R. B. *Nat. Comm.* **2013**, 4.
23. Kamyshny, A.; Magdassi, S. *Small* **2014**, 10 (17), 3515–3535.
24. Choi, K. H.; Yoo, J.; Lee, C. K.; Lee, S. Y. *Energy Environ.*

- Sci.* **2016**, 9 (9), 2812–2821.
25. Kim, K. S.; Zhao, Y.; Jang, H.; Lee, S. Y.; Kim, J. M.; Kim, K. S.; Ahn, J. H.; Kim, P.; Choi, J. Y.; Hong, B. H. *Nature* **2009**, 457 (7230), 706–710.
26. Li, X. S.; Cai, W. W.; An, J. H.; Kim, S.; Nah, J.; Yang, D. X.; Piner, R.; Velamakanni, A.; Jung, I.; Tutuc, E.; Banerjee, S. K.; Colombo, L.; Ruoff, R. S. *Science* **2009**, 324 (5932), 1312–1314.
27. Kim, H.; Cho, M. Y.; Kim, M. H.; Park, K. Y.; Gwon, H.; Lee, Y.; Roh, K. C.; Kang, K. *Adv. Energy Mater.* **2013**, 3 (11), 1500–1506.
28. Kim, H.; Park, K. Y.; Cho, M. Y.; Kim, M. H.; Hong, J.; Jung, S. K.; Roh, K. C.; Kang, K. *Chem. Electro. Chem.* **2014**, 1 (1), 125–130.
29. Wang, D. W.; Li, F.; Liu, M.; Lu, G. Q.; Cheng, H. M. *Angew. Chem.* **2008**, 47 (2), 373–376.
30. Chmiola, J.; Yushin, G.; Gogotsi, Y.; Portet, C.; Simon, P.; Taberna, P. L. *Science* **2006**, 313 (5794), 1760–1763
31. Xu, J. D.; Gao, Q. M.; Zhang, Y. L.; Tan, Y. L.; Tian, W. Q.; Zhu, L. H.; Jiang, L. *Sci. Reports* **2014**, 4.

32. Frackowiak, E.; Lota, G.; Pernak, J. *Appl. Phys. Lett.* **2005**, 86 (16).
33. Wang, J.; Polleux, J.; Lim, J.; Dunn, B. *J. Phys. Chem. C* **2007**, 111 (40), 14925–14931.
34. Lindstrom, H.; Sodergren, S.; Solbrand, A.; Rensmo, H.; Hjelm, J.; Hagfeldt, A.; Lindquist, S. E. *J. Phys. Chem. B* **1997**, 101 (39), 7717–7722.
35. Augustyn, V.; Come, J.; Lowe, M. A.; Kim, J. W.; Taberna, P. L.; Tolbert, S. H.; Abruna, H. D.; Simon, P.; Dunn, B. *Nat. Mater.* **2013**, 12 (6), 518–522.

3.2. UV–ozone engineered MoS₂ synthesized by MOCVD for improved hydrogen evolution

3.2.1. Introduction

The development of renewable and sustainable green energy is a crucial issue to overcome current energy crisis such as carbon dioxide emission and limited resources brought about by traditional fossil fuels.¹⁻⁴ Among the possible alternative energy resources, hydrogen holds tremendous promise because of its high mass energy density and environment friendliness.⁵⁻⁹ Water splitting is one of the most convenient and promising methods for hydrogen production.¹⁰ In general, precious metals such as platinum, rhodium and palladium exhibit have been used as catalysts for excellent hydrogen evolution reaction (HER); however, the scarcity and high cost of precious metals largely limit their applications compared with other environmentally sustainable energy sources.¹¹⁻¹³ Therefore, essential requirements for outstanding catalysts are not only earth–abundant materials

to replace noble metals but also the abilities to increase the efficiency of electrochemical reaction.

Among all these alternatives, molybdenum disulfide (MoS_2), a hexagonally packed layered structure of transition metal dichalcogenide (TMDC) with weak van der Waals interactions, has received tremendous attention in recent years because of the nontoxicity and earth-abundant amount.^{14,15} In addition, good stability and high reactivity of MoS_2 have led it to HER application as a catalyst to replace Pt.^{16,17} Although bulk MoS_2 has poor activity, nanostructured MoS_2 has showed significant enhancement of HER performance due to the edge sites of 2H- MoS_2 , which were theoretically predicted and experimentally demonstrated.¹⁸⁻²¹ Since then, subsequent challenges including phase and structure engineering have been carried out to maximally expose edge sites.^{22,23} Compared to 2H-phase, 1T-phase shows more efficient HER activity in both basal plane and edge, but the stability is very poor to apply common electrochemical catalysis.²⁴⁻²⁶ However, except the structural engineering during the synthesis, a few methods

have been explored to enhance the HER in pristine MoS₂. Recently, Zheng X. L. group reported sulfur vacancies in MoS₂ basal plane using elastic tensile strain and electrochemical desulfurization process.^{27,28} Even though they demonstrated outstanding HER efficiency of MoS₂ films, these methods could not overcome the problems of complicated procedures and long time required for the process. In addition, it is difficult to transfer MoS₂ films on other unprocessed substrates holding the high performance. The other method to generate sulfur vacancies in the basal plane is controlled argon plasma exposure and hydrogen annealing to increase catalytic effects.²⁹ In contrast, the stability and conductivity of monolayer MoS₂ decrease dramatically during the plasma treatments. In addition, the number of electrochemical active edge sites in large-area MoS₂ films synthesized by conventional solid source is limited owing to large grain size. To fully utilize vacancies engineered MoS₂ catalysts for commercial applications, distinctive synthesis method and convenient post-process with acceptable mechanisms and reasons are developed.

Here, we demonstrated that metal organic chemical vapor deposition (MOCVD) and post UV–Ozone treatment could introduce more active sites and increased conductivity via the small grain size and oxygen doping, leading to a high density of exposed edge sites and a significant improvement of the hydrogen evolution activity. Pristine MoS₂ bilayers were synthesized by MOCVD. The grain size of MoS₂ synthesized by metal organic sources had very smaller grain size than solid source synthesis, which increased the possibility to exposure many active sites for HER. In previous study, it is suggested that bilayer MoS₂ had increased photoluminescence (PL) intensity and superior stability than monolayer after UV–ozone process.³⁰ Therefore, we synthesized bilayer films and post UV–ozone oxygen doping process to increase the conductivity. The mechanisms of increased electrochemical hydrogen evolution are explained by PL, exciton life time and other discrete atom scale analyses

3.2.2. Experimental

Preparation of UV–ozone Treated Bilayer MoS₂ by MOCVD

Method. Detail synthesis method is recorded in Supporting Information. Molybdenum hexacarbonyl (Mo(CO)₆) (Sigma Aldrich, > 99.9 %) and hydrogen sulfide (H₂S) (diluted in 5 % in argon) were used as the Mo and S precursor, respectively. One hundred sccm argon was used as the carrier gas during growth. The growth substrate was SiO₂ (300 nm)/Si wafer is loaded at the center of the quartz tube vertically with a quartz wafer carrier. The furnace temperature was raised up to 600 °C in 15 min and kept stable at 600 °C for 120 min. After growth, the furnace was left to cool down naturally. The samples were irradiated with UV light source (UV/ozone cleaner, Bioforce) before characterization.

Material Characterization. Optical microscopy was performed by Nikon ECLIPSE LV100ND. The AFM image was measured by a noncontact mode (Park System, XE–100). The Raman spectra were recorded using Renishaw Invia Raman

Microscope with 1mW 514nm Ar laser with the spot size of 2 μm . We measured PL using NA 0.95 objective lens and CCD (iDus 401 BV) with 24 mW 473 nm laser. The microstructures and morphologies were investigated by field-emission scanning electron microscopy (FESEM, AURIGA Carl Zeiss) and tunneling electron microscopy (TEM, JEOL ARM200F). XPS analysis was carried out with a KRATOS AXIS-His model in Research Institute of Advanced materials. We measured fluorescence lifetime using PicoQuant, Micro Time-200 with 470 nm laser excitation.

Electrochemical Measurement. The electrochemical sample was prepared through a PMMA-assisted transfer method. The MoS₂/SiO₂/Si substrate was first spin-coated by a PMMA thin film. Then, 1 M KOH solution at 90 °C was used as the etchant to etch away the SiO₂ layer. After that, the MoS₂ on the PMMA was rinsed with DI water and then transferred onto a clean glassy carbon electrode. Finally, the sample was baked 70 °C in 1 hour and then the PMMA was washed off with acetone and iso-propanol. In case of UV-ozone treatment samples, the UV-ozone irradiated to the samples after all

transfer processes.

All electrochemical experiments were conducted in a three-electrode system. Ag/AgCl/3M NaCl, Pt and glassy carbon covered by MoS₂ film were used as a reference electrode, a counter electrode and a working electrode, respectively. Electrochemical tests were carried out at room temperature using a potentiostat system (CHI 600D, CH instruments). The electrode potential vs Ag/AgCl was converted to the RHE scale, using the following equation: $E(\text{RHE}) = E(\text{Ag/AgCl}) + 0.197 + 0.0592 \cdot \text{pH}$ V. The electrolyte was sulfuric acid with 500 mM ionic strength and scan rate was 50 mV/sec. Additionally, overpotential values were calculated by the difference between the iR-corrected potential ($V = V_{\text{applied}} - iR$) and the thermodynamic potential of hydrogen evolving reaction.

3.2.3. Results and Discussion

The total process is schematically illustrated in Figure 34a. Similar to Park's group previous study, the MoS₂ atomic layers are synthesized via MOCVD method and hydrogen disulfide gas.³¹ The single-layer MoS₂ films synthesized by MOCVD have very smaller triangular shape (~ 250 nm) than conventional solid source synthesis as shown SEM image in Figure 35. This small grain size give a possibility to expose a high density of edges sites for enhanced HER after UV-Ozone treatments. Controlling the pressure and concentration of liquid source, we could synthesize homogeneous bilayer MoS₂ films.

As shown in Figure 34b, the intensity of both A_{1g} and E¹_{2g} modes in Raman spectra represent the typical in-plane and out of plane vibration of MoS₂ molecule.³² The value of peak frequency differences between A_{1g} and E_{2g} modes is 21 cm⁻¹, which evidences the existence of bilayer MoS₂.³³ The atomic force microscopy (AFM) image in Figure 34c shows the

thickness of MoS₂ is about 1.4 nm, suggesting the MOCVD grown MoS₂ is dominantly bilayer. The typical high-resolution transmission electron microscopy (HRTEM) images for the MoS₂ layer is shown in Figure 34d,e. Energy dispersive X-ray spectroscopy (EDX) is investigated to confirm molybdenum and sulfur as composition elements. (Figure 36). The inset of Figure 34d displays the fast Fourier transform (FFT) of the original HRTEM image, and the points arranged in dodecagon suggest that the MoS₂ films is bilayer. Some folding sites were caused by the unavoidable mechanical deformation during the TEM sample preparation. Two layers, where each layer is ~ 0.65 nm thick, are identified at the folding sites in Figure 34e, providing direct evidence that the synthesized films are bilayer MoS₂. X-ray photoemission spectroscopy (XPS) and PL techniques are effective for characterization of the crystal quality for two-dimensional materials. As shown in Figure 37, the XPS scans for the binding between Mo and S confirm the chemical bonding states of the MoS₂ layers.³⁴ The PL spectrum and mapping constructed by plotting the PL peak intensity (650 ~ 700 nm)

in confocal measurements (Figure 38) show typical bilayer MoS₂ emission peak.³⁵ The above results demonstrate the nature of homogenous high quality bilayer MoS₂ films synthesized by our MOCVD methods.

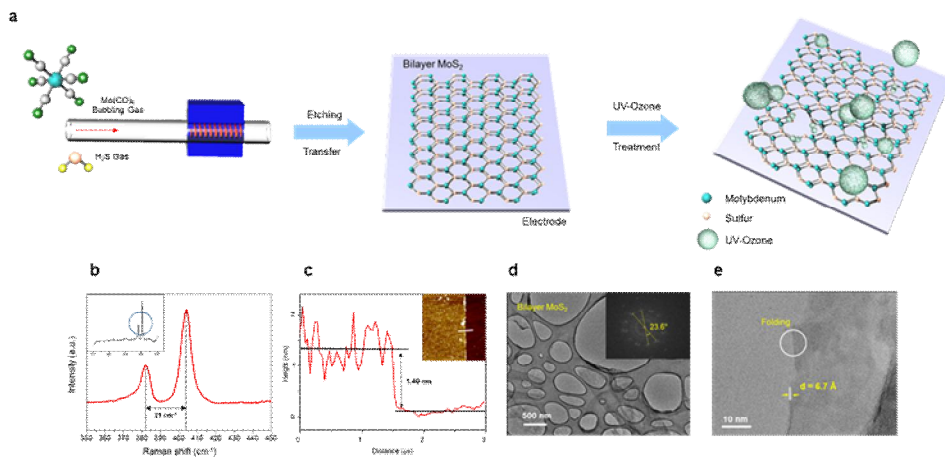


Figure 34. Schematic illustration of the entire process and the bilayer MoS₂ films characterization. (a) Schematic illustration of UV–Ozone engineered bilayer MoS₂ films synthesized by MOCVD. (b) Raman spectra and of the bilayer MoS₂. (c) AFM image of MOCVD grown bilayer MoS₂ with a thickness of ~ 1.4 nm, as measured along the yellow line in inset profile. (d,e) CS–TEM image of the bilayer MoS₂ shows its hexagonal planar lattice: the inset shows a fast Fourier transform (FFT).

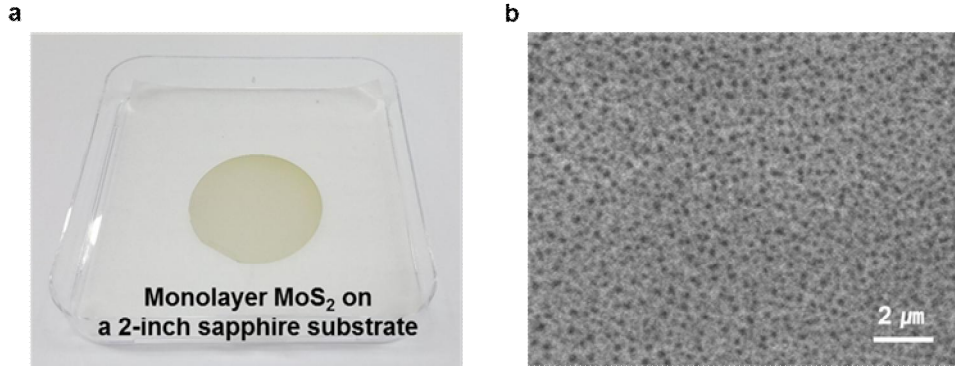


Figure 35. A photograph and SEM image of MOCVD-grown monolayer MoS₂ on a sapphire substrate. Not only SiO₂/Si wafer but also sapphire could be also used as a growth substrate. Triangular crystal shape, which size is below 250 nm, is confirmed at 60 min growth time.

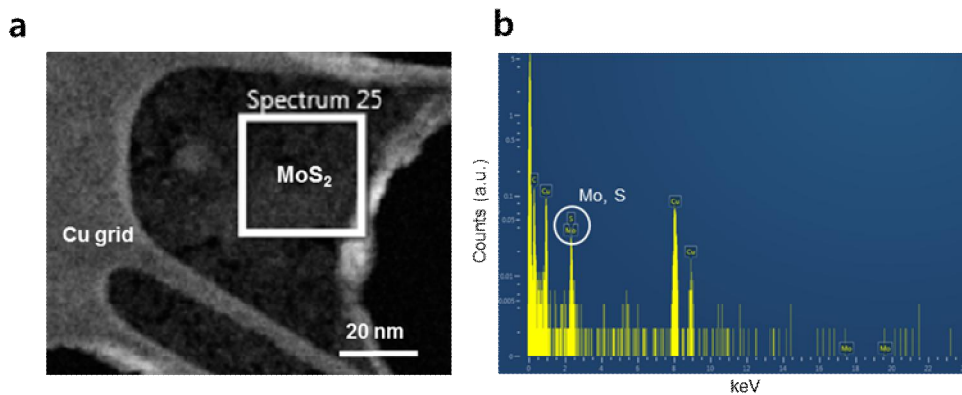


Figure 36. TEM image and EDS spectrum of the pristine bilayer MoS₂ films. (a) TEM image of the bilayer MoS₂ on a conventional lacey copper grid. (b) EDS spectrum of the bilayer MoS₂ films at white square in (a).

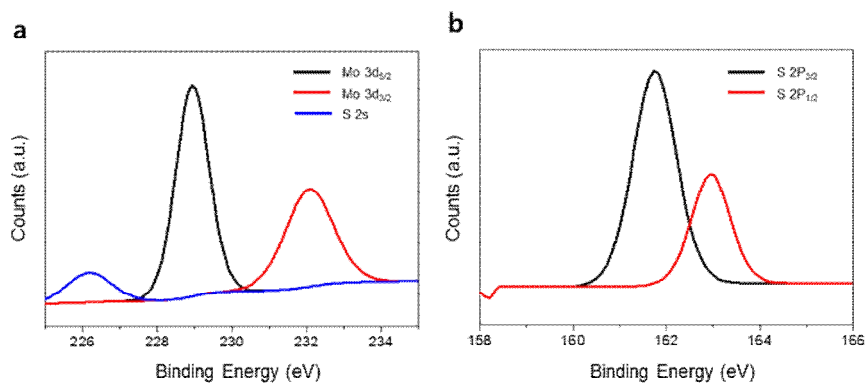


Figure 37. XPS spectra for the MoS₂ bilayer grown by our method. (a) Mo 3d 5/2, 3/2 and S 2s state. (b) S 2p 3/2 and 1/2.

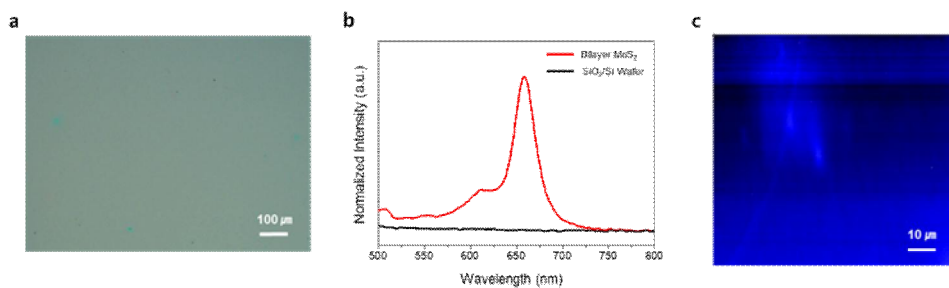


Figure 38. A photograph and PL measurement of the pristine bilayer MoS₂ on SiO₂/Si wafer. (a) Optical microscope image of the bilayer MoS₂ synthesized by our MOCVD on SiO₂/Si wafer. (b) PL spectrum of the bilayer MoS₂ obtained at (a) compared with a bare SiO₂/Si wafer. (c) PL mapping of the bilayer MoS₂ obtained at (a).

Because the edge sites of MoS₂ are active for catalytic effect, while the basal plane is inert, introduction of doping and defects in basal plane is an effective way to enhance the performance as reaction catalysts. Plasma exposure has already been demonstrated as an effective techniques to engineer the bandgap and structure of MoS₂.^{29,36–38} However, the stability and conductivity exposed to plasma are poor due to the lattice structure deformation. UV–ozone treatments also could manipulate opto–electrical properties of MoS₂ with relatively superior conductivity compared to plasma techniques due to weak power intensity and oxygen doping.³⁰ We applied the same process to bilayer MoS₂ synthesized by our MOCVD methods in order to analyze the change of the catalytic activity. While MoS₂ samples were exposed to UV–ozone, the fundamental structure and properties were tuned. First, we measured Raman spectrum depending on UV–ozone exposure. After UV–ozone exposure, in–plane vibration mode E_{2g}¹ is red shifted and out of plane vibration mode A_{1g} is blue

shifted. (Figure 39a) The value of peak frequency differences between A_{1g} and E_{2g} modes changes to 19 cm^{-1} . This Raman spectra changes confirm the lattice distortion caused by oxygen.³⁹ The simple electronic structure of MoS_2 layer shows two exciton transitions known as direct (K point) and indirect transition (Γ point).⁴⁰ The intensity and wavenumber of the PL peak also varied depending on the UV–ozone exposure time, as shown in Figure 39b. During the UV–ozone exposure, the treatment could improve the MoS_2 conductivity by oxygen doping and structural deformation, which results in the increased PL intensity. However, gradually over time, UV–ozone eventually cause lower crystal symmetry and increased lattice distortion, which can be attributed to conductivity degradation as electrochemical catalysts. To analyze more accurate investigation, we measured high–angle annular dark field (HAADF) aberration–corrected scanning transmission electron microscopy (CS–STEM) and electron energy loss spectroscopy (EELS). In Figure 39c, oxygen incorporation is confirmed at the atomic scale based on their image intensity, where the bright and dark areas correspond

to bilayer and monolayer, respectively. Thus, some parts were broken down to monolayer by UV–ozone, resulting in their FFT convert from dodecagonal to hexagonal as shown in Figure 39c inset image. Figure 39d shows the EELS spectrum of MoS₂ films on TEM grid before and after UV–ozone treatment process. There is no oxygen peak in pristine MoS₂, while the appearance of a new peak in UV–ozone treated MoS₂ directly indicates the formation of oxygen bonding. Not limited to a temporary site, but such EELS spectrum can be observed throughout the entire region. (Figure 40) XPS analysis on the pristine and UV–ozone treated MoS₂ is further used to confirm the formation of oxygen bonding in MoS₂ symmetry.

Figure 39e~h show the XPS results of Mo, S, O and C respectively, for the pristine and UV–ozone treated samples. The Mo 3d peak positions at binding energies of 229.8 and 232.5 eV were observed and remained almost unchanged after UV–ozone treatment. Two peaks at binding energies of 162.8 eV and 164.0 eV corresponding to S 2p_{3/2} and 2p_{1/2}, respectively, were observed. The unusual change is that other

peak was generated at 529.8 eV after UV–ozone treatment; it was reported previously that S–O bonding of O 1s.⁴¹ It is also supported by an additional peak at ~165 eV in S 2p spectrum, indicating the oxidation of sulfur.⁴² The oxygen atoms seem to substitute for the Mo atoms or adhere on MoS₂ films, resulting in the S–O bonds. Overall, we demonstrated that UV–ozone could control the opto–electrical properties of MoS₂ and their crystal symmetry.

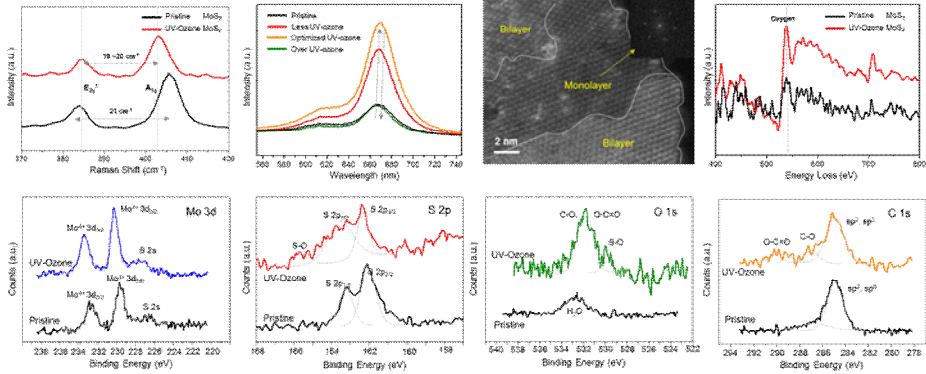


Figure 39. Characterization of the bilayer MoS₂ films after UV-ozone treatments. (a) Raman spectrum of the bilayer MoS₂ films under UV-ozone. (b) PL spectra of the bilayer MoS₂ under UV-ozone. (c) PL peak wavelength as a function of UV-ozone exposure time. (d) CS-STEM HAADF images after UV-ozone: the inset shows a FFT which converts to hexagonal pattern. (e) EELS spectrum of the pristine bilayer MoS₂ and after UV-ozone treatments. (e-h) XPS spectra of the pristine bilayer MoS₂ and after UV-ozone treatments for Mo 3d, S 2p, O 1s and C 1s, separately.

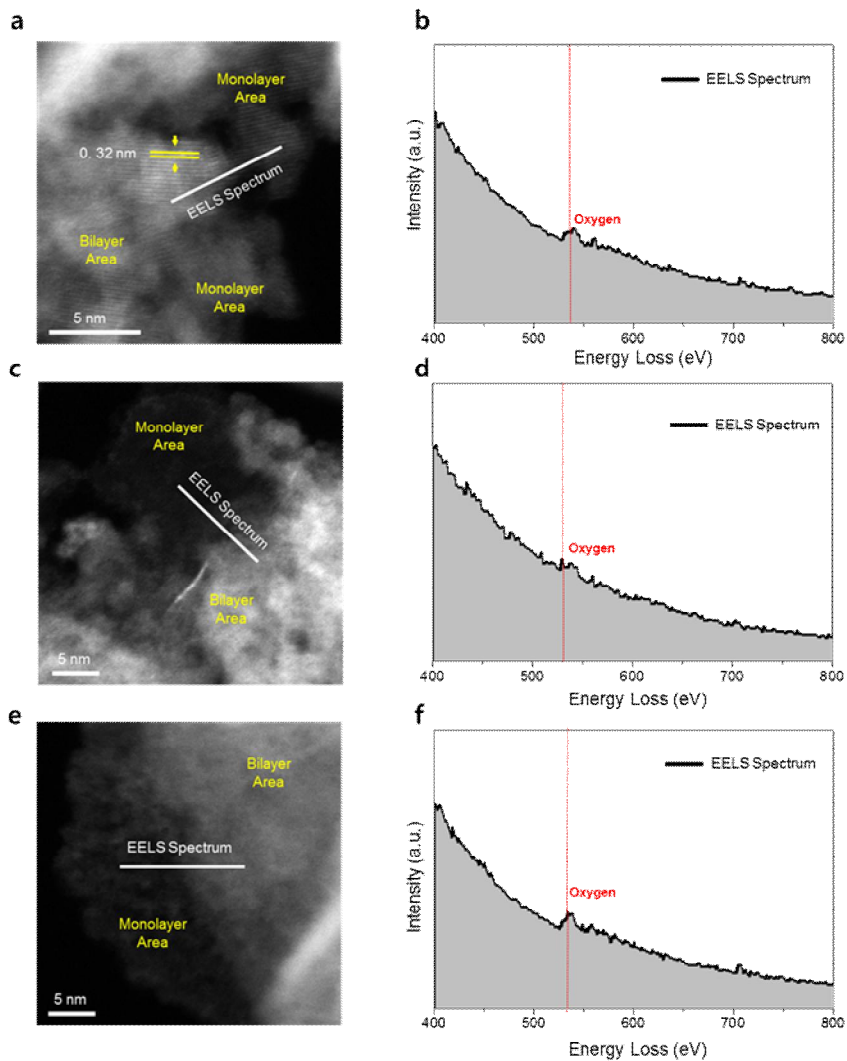


Figure 40. CS-TEM analysis after UV-ozone treatment on the bilayer MoS₂. (a,c,f) CS-STEM HADDF images after UV-ozone treatment at various locations. (b,d,f) EELS spectrum at line profile in (a), (c) and (e), respectively.

We further plotted the PL intensity variation as a function of the applied laser exposure time to investigate oxygen incorporation effect. The UV–ozone treated bilayer MoS₂ produces more excitons when exposed to laser source due to oxygen doping, which are sufficiently more produced than the pristine MoS₂. (Figure 41a,b) To further investigate this dissimilarity, we plotted the ratio of real–time PL intensity to initial PL intensity according to laser exposure time as shown in Figure 41c. In case of pristine MoS₂, the emission ratio of direct and indirect transition looks similar. However, UV–ozone treated MoS₂ shows considerably different ratio for direct (~ 1.38) and indirect (~ 1.02) transition. These time dependent emission intensity ratio may result from defect generation in MoS₂ planes. The intensity increase of direct transition may originate from the generation of defects or oxygen incorporation, which are caused by UV–ozone treatment. In order to apply the generated MoS₂ excitons as electrocatalysts, we measured exciton radiative lifetimes.

Compared with exciton life time of bilayer MoS₂ (~ 1.3 ns) calculated by density functional theory (DFT), the bilayer MoS₂ synthesized by our MOCVD method has similar exciton life time (~ 1.34 ns) at room temperature.⁴³ It is first time that the synthesized MoS₂ exciton life time is comparable that of the computational values. As shown in Figure 41d, the exciton life time of bilayer MoS₂ is continuously extended in proportion to the rise of UV–ozone exposure time. (The detailed life time values are in Table 1.) However, when the MoS₂ symmetry is broken because of the over exposure to UV–ozone, we confirm that the exciton life time is decreased. Through exciton life time measurement, oxygen doping phenomenon and PL intensity variation depending on UV–ozone exposure time are demonstrated. Therefore, we promise that UV–ozone treatment could control the exciton radiative lifetimes of two–dimensional TMDC.

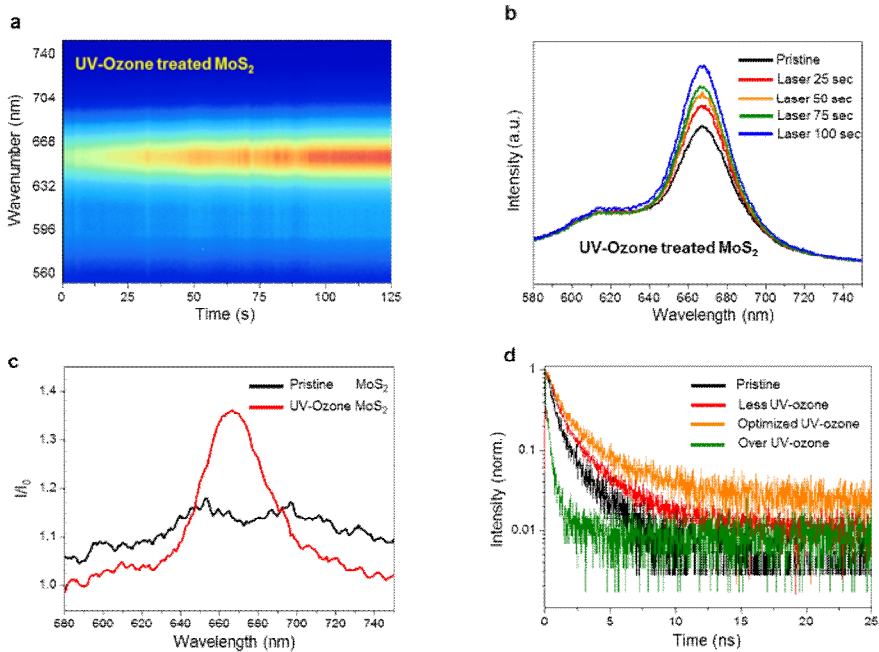


Figure 41. PL intensity variation depending on laser exposure time and exciton life-time measurement. (a,b) PL intensity variation of the UV-ozone treated bilayer MoS₂ depending on 473 nm laser exposure time. (c) The ratio of in-situ PL intensity to initial PL intensity after laser 125 sec exposure. (d) Exciton life-time spectra of the bilayer MoS₂ synthesized by MOCVD depending on UV-ozone process time.

	Pristine	Less exposure	Optimization exposure (5 sec)	Over exposure
Exciton Life - Time (ns)	1.34 (DFT theory : 1.3 Exfoliation : 0.71)	1.83	2.36	0.35

Table 1. Exciton life-time values depending on UV-ozone exposure time. Computational DFT theory and exfoliation experimental values are studied in previously report.^{43,44}

In order to investigate the effects of grain size and oxygen doping on catalytic performance of MoS₂ basal planes, hydrogen evolving activity of bilayer MoS₂ before and after UV–ozone treatment was evaluated by cyclic voltammetry (CV) in 0.5 M sulfuric acid electrolyte using rotating disk electrode (RDE). To diminish the contribution of non-Faradaic current, CV curves were polarization-corrected. Based on PL intensity depending on laser exposure time, we expected that UV–ozone treatment for 5 seconds exhibited the optimal HER performance due to its exciton lifetime and lattice variation characterization. Thus, the catalytic activity of MoS₂ with 5 second UV–ozone process was compared with that of pristine MoS₂. As shown in Figure 42a, current density at -0.4 V vs. RHE was -3.82 and -15.2 mA/cm² for the pristine electrode and UV–ozone treated electrode, respectively. We found that UV–ozone process on bilayer MoS₂ synthesized by MOCVD markedly enhanced HER electrocatalytic activity. The overpotential at the current density of 10 mA/cm² was 362.4 mV. These results represent considerable catalytic activity among pure MoS₂ basal planes

excluding chemically exfoliated MoS₂ combined with other materials and functional groups. (Figure 43 and Table 2) Tafel plots were obtained from the polarized–corrected CV curves (Figure 42b). Tafel slopes for pristine and UV–ozone treated MoS₂ were measured as 231 and 135 mV/dec, respectively. For the electrochemical HER, current–potential relationship was described by Equation 1, where j_0 , α , F and b are the exchange current density, electron transfer coefficient, Faraday constant, overpotential and Tafel slope, respectively. Additionally, Tafel slope was expressed as inverse relation with electron transfer coefficient (Equation 2).

$$j = j_0 \exp\left(-\frac{\alpha F \eta}{RT}\right) \quad (1) \qquad b = \left(\frac{\partial \eta}{\partial \log j}\right) = \frac{2.3 RT}{\alpha F} \quad (2)$$

The lower value of Tafel slope is indicated that the kinetics of electrochemical HER occurs briskly. Based on the electrokinetic study, UV–ozone treated MoS₂ showed lower overpotential and Tafel slope compared to pristine MoS₂ for HER due to defect generation and oxygen doping induced by UV–ozone process. As shown in Figure 42c, negligible

difference can be observed between the current density at the initial cycle and after 3500 sec, suggesting the excellent stability of the MoS₂ films synthesized by our MOCVD methods during long-term cycling. The superior catalytic activity as well as stability of the MOCVD based bilayer MoS₂ catalysts with UV–ozone treatment can be attributed to three aspects, as shown in Figure 42d. First, very small grain size give a possibility of active sites for HER. Second, UV–ozone treatment provides edge sites and oxygen incorporation in MoS₂, which enhances the intrinsic activity of MoS₂ basal planes. Last, UV–ozone treated bilayer MoS₂ has good structural stability and exciton production compared with UV–ozone treated monolayer. In summary, the combined modulations of active sites, electron conductivity and exciton life–time may open a new avenue for improving the catalytic activity of two–dimensional electrocatalysts.

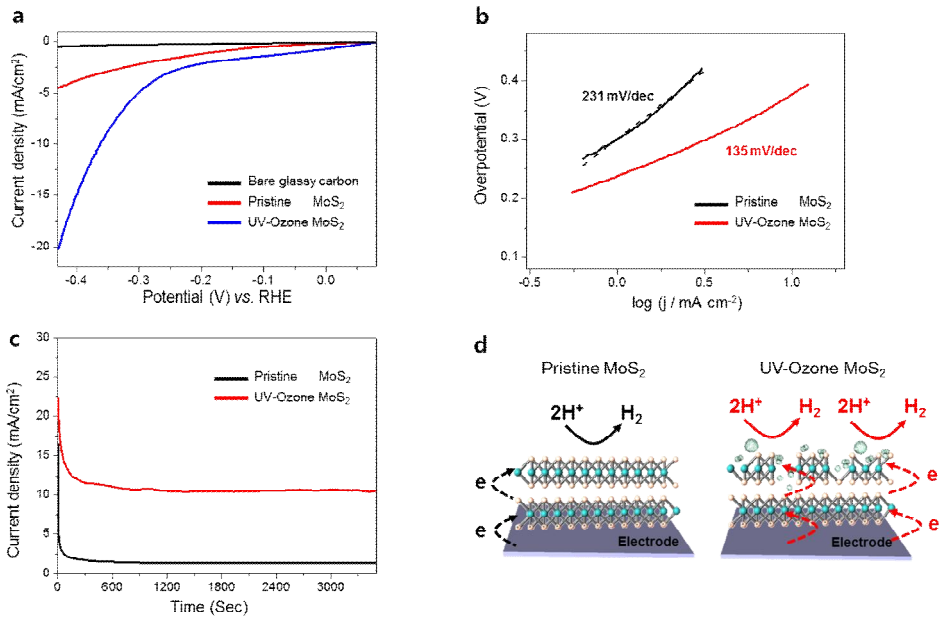


Figure 42. HER properties of the bilayer MoS₂ synthesized by MOCVD before and after UV–ozone treatment. (a) polarized CV curves show the cathodic sweep of the first cycle. Enhanced activity is observed after UV–ozone treatment. (b) Tafel plots show the improved electrochemical activity of the bilayer MoS₂ catalyst with UV–ozone treatment. (c) Stability test for the bilayer MoS₂ on glassy carbon. (d) The mechanism illustration of the UV–ozone treated MoS₂ HER compared of the pristine MoS₂.

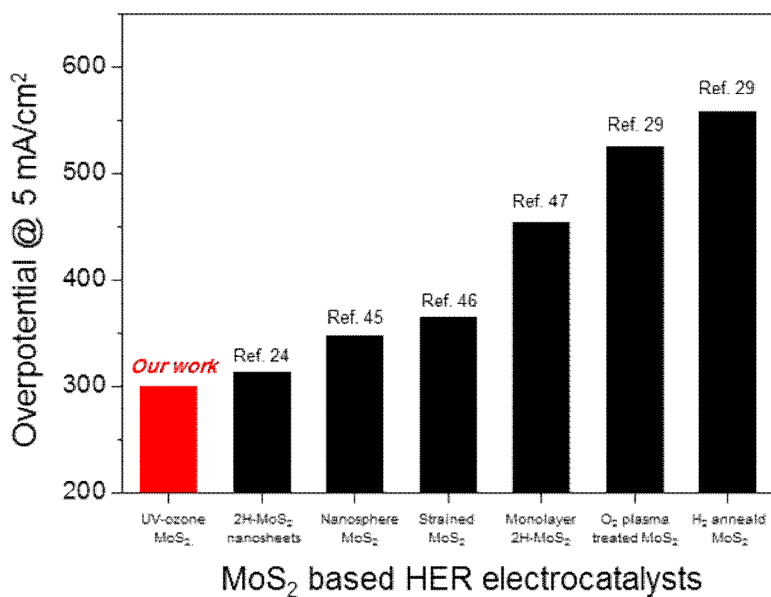


Figure 43. HER overpotential performance comparison. HER overpotential values of MoS₂ electrocatalysts at 5 mA/cm² are compared. References were focused on film types excluding multilayers MoS₂ derived from chemical exfoliation or composites with other materials.

	Overpotential (mV) @ 10 mA/cm ²	Overpotential (mV) @ 5 mA/cm ²	Tafel slope (mV/dec)	Electrode & Electrolyte
Bilayer MoS ₂ by MOCVD (Our work)	N/A	N/A	231	Glassy carbon 0.5 M H ₂ SO ₄
UV-Ozone treated MoS ₂ (Our work)	362.4	300.4	135	Glassy carbon 0.5 M H ₂ SO ₄
2H-MoS ₂ nanosheets ⁴	377	314	75~85	Glassy carbon 0.5 M H ₂ SO ₄
Nanosphere MoS ₂ ⁵	> 400	348	140	Glassy carbon 0.5 M H ₂ SO ₄
Strain-induced MoS ₂ ⁶	405	365	135	Ag electrode 0.5 M H ₂ SO ₄
Monolayer 2H-MoS ₂ ⁷	N/A	454	98	FTO electrode 0.5 M H ₂ SO ₄
Oxygen plasma treated MoS ₂ ⁸	618	526	171	Glassy carbon 0.5 M H ₂ SO ₄
Hydrogen annealed MoS ₂ ⁸	> 600	558	147	Glassy carbon 0.5 M H ₂ SO ₄
Monolayer MoS ₂ (by CVD) ⁸	N/A	N/A	342	Glassy carbon 0.5 M H ₂ SO ₄
Multilayer MoS ₂ @ MWNT ⁹	N/A	>300	92.7	FTO electrode 0.5 M H ₂ SO ₄
Monolayer MoS ₂ @ nanoporous Au ¹⁰	> 400	> 400	46	Nanoporous Au 0.5M H ₂ SO ₄

Table 2. HER performance comparison. References were focused on pure film types excluding chemically exfoliated MoS₂ combined with other materials and functional groups.

3.2.4. Conclusion

In conclusion, we demonstrated that UV–ozone treated bilayer MoS₂ synthesized by MOCVD has high performance of the HER catalytic activities including the onset, current density and Tafel slope. The MoS₂ catalysts synthesized by MOCVD have superior electrochemical activity than conventional solid source synthesis, and cracking sites and oxygen doping by UV–ozone treatment could also increase the HER efficiency. More importantly, the correlation between the microscale structure variations of MoS₂ bilayer and its opto–electrical properties such as PL and exciton lifetimes and the reason why we use bilayer MoS₂ as HER catalysts were established for the first time. Our work provides new insight of fundamental catalyst mechanism of MoS₂ and improved application plans with low cost and short processing time. Since most two–dimensional materials can be developed by MOCVD and simple UV–ozone treatment, our approach can be used directly to further enhance the HER activity of not only MoS₂ but also all catalysts of the two–dimensional planar materials.

3.2.5. References

1. Turner, J. A., *Science* **2004**, *305*(5686), 972–974.
2. Lewis, N. S.; Nocera, D. G. *Proc. Natl. Acad. Sci. U.S.A.* **2006**, *103*(43), 15729–15735.
3. Stolley, R. M.; Helm, M. L. *Nat. Chem.* **2014**, *6*(11), 949–950.
4. Panwar, N. L.; Kaushik, S. C.; Kothari, S. *Renewable Sustainable Energy Rev.* **2011**, *15*(3), 1513–1524.
5. Mallouk, T. E. *Nat. Chem.* **2013**, *5*(5), 362–363.
6. Norskov, J. K.; Christensen, C. H. *Science* **2006**, *312*(5778), 1322–1323.
7. Benck, J. D.; Hellstern, T. R.; Kibsgaard, J.; Chakthranont, P.; Jaramillo, T. F. *ACS Catal.* **2014**, *4*(11), 3957–3971.
8. Yan, Y.; Xia, B. Y.; Xu, Z. C.; Wang, X. *ACS Catal.* **2014**, *4*(6), 1693–1705.
9. Kibler, L.A. *Chemphyschem* **2006**, *7*(5), 985–991.
10. Cook, T. R.; Dogutan, D. K.; Reece, S. Y.; Surendranath, Y.; Teets, T. S.; Nocera, D. G. *Chem. Rev.* **2010**, *110*(11), 6474–6502.

11. Chen, C.; Kang, Y. J.; Huo, Z. Y.; Zhu, Z. W.; Huang, W. Y.; Xin, H. L. L.; Snyder, J. D.; Li, D. G.; Herron, J. A.; Mavrikakis, M.; Chi, M. F.; More, K. L.; Li, Y. D.; Markovic, N. M.; Somorjai, G. A.; Yang, P. D.; Stamenkovic, V. R. *Science* **2014**, *343*(6177), 1339–1343.
12. Fujishima, A.; Honda, K. *Nature* **1972**, *238*(5358), 37–+..
13. Meng, F. K.; Li, J. T.; Hong, Z. L.; Zhi, M. J.; Sakla, A.; Xiang, C. C.; Wu, N. Q. *Catal. Today* **2013**, *199*, 48–52.
14. Rapoport, L.; Fleischer, N.; Tenne, R. *J. Mater. Chem.* **2005**, *15*(18), 1782–1788.
15. Lin, Y. C.; Dumcenco, D. O.; Kosma, H. P.; Niimi, Y.; Krasheninnikov, A. V.; Huang, Y. S.; Suenaga, K. *Adv. Mater.* **2014**, *26*(18), 2857–2861.
16. Li, Y. G.; Wang, H. L.; Xie, L. M.; Liang, Y. Y.; Hong, G. S.; Dai, H. J. *J. Am. Chem. Soc.* **2011**, *133*(19), 7296–7299.
17. Lee, J. K.; Lee, W.; Yoon, T. J.; Park, G. S.; Choy, J. H., A *J. Mater. Chem.* **2002**, *12*(3), 614–618.
18. Tributsch, H.; Bennett, J. C. *J. Electroanal. Chem.* **1977**, *81*(1), 97–111.
19. Hinnemann, B.; Moses, P. G.; Bonde, J.; Jorgensen, K. P.;

- Nielsen, J. H.; Horch, S.; Chorkendorff, I.; Norskov, J. K. *J. Am. Chem. Soc.* **2005**, *127*(15), 5308–5309.
20. Jaramillo, T. F.; Jorgensen, K. P.; Bonde, J.; Nielsen, J. H.; Horch, S.; Chorkendorff, I. *Science* **2007**, *317*(5834), 100–102.
21. Kibsgaard, J.; Chen, Z. B.; Reinecke, B. N.; Jaramillo, T. F., *Nat. Mater.* **2012**, *11*(11), 963–969.
22. Kong, D. S.; Wang, H. T.; Cha, J. J.; Pasta, M.; Koski, K. J.; Yao, J.; Cui, Y. *Nano Lett.* **2013**, *13*(3), 1341–1347.
23. Li, D. J.; Maiti, U. N.; Lim, J.; Choi, D. S.; Lee, W. J.; Oh, Y.; Lee, G. Y.; Kim, S. O. *Nano Lett.* **2014**, *14*(3), 1228–1233.
24. Voiry, D.; Salehi, M; Silva, R.; Fujita, T.; Chen, M. W.; Asefa, T.; Shenoy, V. B.; Eda, G.; Chhowalla, M. *Nano Lett.* **2013**, *13*(12), 6222–6227.
25. Lukowski, M. A.; Daniel, A. S.; Meng F.; Forticaux, A.; Li, L. S.; Jin, S. *J. Am. Chem. Soc.* **2013**, *135*(28), 10274–10277.
26. Wang, H. T.; Lu, Z. Y.; Xu, S. C.; Kong, D. S.; Cha, J. J.; Zheng, G. Y.; Hsu, P. C.; Yan, K.; Bradshaw, D.; Prinz, F.

- B.; Cui, Y. *Proc. Natl. Acad. Sci. USA* **2013**, *110*(49), 19701–19706.
27. Li, H.; Tsai, C.; Koh, A. L.; Cai, L. L.; Contryman, A. W.; Fracapane, A. H.; Zhao, J. H.; Han, H. S.; Manoharan, H. C.; Abild-Pedersen, F.; Norskov, J. K.; Zheng, X. L. *Nat. Mater.* **2016**, *15*(3), 48–56.
28. Tsai, C.; Li, H.; Park, S.; Park, J.; Han, H. S.; Norskov, J. K.; Zheng, X. L.; Abild-Pedersen, F. *Nat. Commun.* **2017**, *8*.
29. Ye, G. L.; Gong, Y. J.; Lin, J. H.; Li, B.; He, Y. M.; Pantelides, S. T.; Zhou, W.; Vajtai, R.; Ajayan, P. M. *Nano Lett.* **2016**, *16*(2), 1097–1103.
30. Su, W. T.; Kumar, N.; Spencer, S. J.; Dai, N.; Roy, D. *Nano Res.* **2015**, *8*(12), 3873–3886.
31. Kang, K.; Xie, S. E.; Huang, L. J.; Han, Y. M.; Huang, P. Y.; Mak, K. F.; Kim, C. J.; Muller, D.; Park, J. *Nature* **2015**, *520*(7549), 656–660.
32. Splendiani, A.; Sun, L.; Zhang, Y. B.; Li, T. S.; Kim, J.; Chim, C. Y.; Galli, G.; Wang, F. *Nano Lett.* **2010**, *10*(4), 1271–1275.

33. Li, H.; Yin, Z. Y.; He, Q. Y.; Li, H.; Huang, X.; Lu, G.; Fam, D. W. H.; Tok, A. I. Y.; Zhang, Q.; Zhang, H. *Small* **2012**, *8*(1), 63–67.
34. Altavilla, C.; Sarno, M. Ciambelli, P. *Chem. Mater.* **2011**, *23*(17), 3879–3885.
35. Matte, H. S. S. R.; Gomathi, A.; Manna, A. k.; Late, D. J.; Datta, R.; Pati, S. K.; Rao, C. N. R. *Angew Chem. Int. Edit.* **2010**, *49*(24), 4059–4062.
36. Azizi, A.; Zou, X. L.; Ercius, P.; Zhang, Z. H.; Elias, A. L.; Perea–Lopez, N.; Stone, G.; Terrones, M.; Yakobson, B. I.; Alem, N. *Nat. Commun.* **2014**, *5*.
37. Mouri, S.; Miyauchi, Y.; Matsuda, K. *Nano Lett.* **2013**, *13*(12), 5944–5948.
38. Nan, H. Y.; Wang, Z. L.; Wang, W. H.; Liang, Z.; Lu, Y.; Chen, Q.; He, D. W.; Tan, P. H.; Miao, F.; Wang, X. R.; Wang, J. L.; Ni, Z. H. *ACS Nano* **2014**, *8*(6), 5738–5745.
39. Kang, N. R.; Paudel, H. P.; Leuenberger, M. N.; Tetard, L.; Khondaker, S. I. *J. Phys. Chem. C* **2014**, *118*(36), 21258–21263.
40. Mak, K. F.; Lee, C.; Hone, J.; Shan, J.; Heinz, T. F. *Phys.*

- Rev. Lett.* 2010, *105*(13).
41. Kim, S.; Choi, M. S.; Qu, D.; Ra, C. H.; Liu, X.; Kim, M.; Song, Y. J.; Yoo, W. J. *2D Mater.* **2016**, *3*(3).
42. Azcatl, A.; McDonnell, S.; Santosh, K. C.; Peng, X.; Dong, H.; Qin, X. Y.; Addou, R.; Mordi, G. I.; Lu, N.; Kim, J.; Kim, M. J.; Cho, K.; Wallace, R. M. *Appl. Phys. Lett.* **2014**, *104*(11).
43. Palummo, M.; Bernardi, M.; Grossman, J. C. *Nano Lett.* **2015**, *15*(5), 2794–2800.
44. Shi, H.; Yan, R.; Bertolazzi, S.; Brivio, J.; Gao, B.; Kis, A.; Jena, D.; Xing, H. G.; Huang, L. *ACS Nano* **2013**, *7*, 1072–1080.
45. Kumar, S. M. S.; Selvakumar, K.; Karthikeyan, J.; Thangamuthu, R.; Karthikeyan, J.; Thangamuthu, R.; Murugan, P.; Rajput, P.; Jha, S. N.; Bhattacharyya, D., Navascues, N.; Irusta, S. *ChemistrySelect* **2017**, *2*(17), 4667–4672.
46. Lee, J. H.; Jang, W. S.; Han, S. W.; Baik, H. K. *Langmuir* **2014**, *30*(32), 9866–9873.
47. Chang, K.; Hai, X.; Pang, H.; Zhang, H. B.; Shi, L.; Liu, G.

G.; Liu, H. M.; Zhao, G. X.; Li, M.; Ye, J. H. *Adv. Mater.* **2016**, *28*(45), 10033–10041.

48. Ahn, E.; Kim, B. S. *ACS Appl. Mater. Interfaces* **2017**, *9*(10), 8688–8695.

49. Tan, Y. W.; Liu, P.; Chen, L. Y.; Cong, W. T.; Ito, Y.; Han, J. H.; Guo, X. W.; Tang, Z.; Fujita, T.; Hirata, A.; Chen, M. W. *Adv. Mater.* **2014**, *26*(47), 8023–+.

초록

화학기상증착법을 이용한 2차원 물질 합성과 스마트 응용

강상민
자연과학대학 화학부
서울대학교 대학원

기계적 박리 방법으로 그래핀이 처음 발견된 이후로 층상 구조로 존재하는 2차원 물질에 관한 연구는 지난 몇 년 동안 폭발적으로 이루어져 왔다. 비록 기계적 박리 방법이 고품질의 2차원 물질을 제공하지만, 마이크로 단위 수준의 결정 크기는 기계적 박리의 산업에서의 응용을 어렵게 만들었다. 화학기상증착법은 대면적의 2차원 물질을 제공하면서 앞서의 한계에 해답을 제공한다. 현재 화학기상증착법을 이용한 2차원 물질의 합성방법 발달은 그들의 산업적 응용에 기반이 되고 있다. 2차원 물질의 아주 얇은 두께와 단위 부피 당 매우 큰 표면적 때문에, 산업적인 응용 분야 중 전자파 차폐와 전기화학적 촉매로서의 응용을 유망케 하였다. 전 세계 연구진들이 화학기상증착법으로 합성한 2차원 물질의 전자파 차폐 및 전기화학적 응용에 관한 연구를 진행하고 있다. 이 논문에서는 전자파 차폐와 전기화학적 응용과 관련된 몇 가지 실험 결과와 새로운 물질을 소개하면서, 2차원 물질의 미래 산업의 주요 재료로서 그 가능성을 제시한다.

먼저, 2차원 물질의 대표적 물질인 그래핀을 저압화학기상증착법을 통해 합성하고, 전자파 흡수를 통한 열

발생 현상을 소개한다. 외부의 전자기장은 그래핀 내부 이동하는 전자들의 오비탈 스핀을 유도하고, 유도된 반자성의 오비탈 스핀은 전자파를 흡수하고 이를 열로 방출한다. 이 경우, 반자성이 전자의 오비탈 스핀에 비례하기 때문에, 그래핀의 전도도 보다 전자의 이동도가 더 중요한 역할을 한다. 이러한 그래핀의 전자파 흡수를 통한 열 발생 현상이 차세대 스마트 창문과 다이아이스/디포그 시스템의 재료로 쓰일 것을 예상한다.

더불어, 그래핀 코팅을 통한 전자파 차폐와 안구건조증 효과를 막을 수 있는 콘택트 렌즈의 플랫폼을 제시한다. 그래핀 렌즈의 전자파 차폐 기능은 전자레인지 내부에서 강한 전자기장이 인가해졌을 때, 달걀 흰자의 변성 여부로 확인한다. 또한, 그래핀 렌즈로 밀봉된 유리병 내부의 실시간 투습율 측정을 통해 안구건조증 효과를 증명한다. 따라서, 그래핀을 코팅을 통한 콘택트 렌즈가 미래 웨어러블 기술의 생체 공학적인 모델로서의 가능성을 제시한다.

다음 장에서는 2차원 물질의 전기화학적 응용에 관한 결과물을 요약한다. 기존의 레이저 프린터 토너를 전구체로 이용하여 그래핀/흑연질 탄소 이중구조를 고안한다. 금속 포일 위에 토너 전구체가 레이저 패터닝되고, 수소 분위기 아래에서 어닐링 공정을 통해 슈퍼캐패시터로 응용 가능한 아주 얇은 그래핀/흑연질 탄소 이중구조를 합성한다. 그래핀/흑연질 탄소 이중구조로 만들어진 전기화학 셀은 기존의 슈퍼캐패시터와 비교하여 높은 에너지 밀도 및 성능을 보인다.

마지막으로, 유기금속화학기상증착법과 자외선 오존 공정을 통하여 이황화몰리브데넘을 합성한다. 기존의 방법과 비교하여 작아진 결정 크기와 산소 도핑을 통해 증가된 전도성은 우수한

수소 방출 반응을 가능케 한다. 향상된 전기화학적 수소 발생은 증가된 인광 측정과 여기자 수명 측정을 통해 분석한다. 앞서의 결과물을 통해 2차원 물질의 촉매효과 및 그 과정을 이해하고, 앞으로의 물 분해 산업에 계속되어 응용 될 것임을 확인한다.

Appendix

List of Publications

7. S. Kang, J. -J. Koo, H. Seo, Q. T. Truong, J. B. Park, S. C. Park, Y. Jung, S. -P. Cho, K. T. Nam, Z. H. Kim, B. H. Hong, “UV–ozone engineered MoS₂ synthesized by MOCVD for improved hydrogen evolution” , *Submitted*, (2017).

6. S. H. Kang,* S. Kang,* S. C. Park, J. B. Park, B. H. Hong, “Silicon germanium photo–blocking layers in a–IGZO based display under light illumination” , *Submitted*, (2017).
(co–first authorship)

5. S. Kang, K. Lim, H. Park, J. B. Park, S. C. Park, S.–P. Cho, K. Kang, B. H. Hong, “Roll–to–roll laser–printed graphene–graphitic carbon electrodes for supercapacitors” , *ACS Appl. Mater. Interfaces*, *Online Published*, (2017).

4. S. Lee,* I. Jo,* S. Kang,* B. Jang, J. Moon, Y. Kim, S. Lee, S. Rho, B. H. Hong, “Smart contact lenses with graphene coating for EMI shielding and dehydration protection” , *ACS Nano* **11**(6), 5318–5324 (2017).
(co–first authorship)

3. S. Kang, H. Choi, S. B. Lee, S. C. Park, Y. Kim, J. B. Park, S. Lee, and B. H. Hong, “Efficient heat generation in

large-area graphene films by electromagnetic wave absorption” , *2D Mater.* **4**, 025037 (2017).

2. J. B. Park, D. Shin, S. Kang, S.-P. Cho, B. H. Hong, “A distortion in two dimensional shapes of merging nanobubbles: An evidence for anisotropic gas flow” , *Langmuir*, **32**(43), 11303–11308 (2016).

1. J. B. Park, Y.-J. Kim, J. M. Yoo, Y. Kim, S.-M. Kim, S. J. Kim, R. Gorbachev, I. I. Barbolina, S. J. Kim, S. Kang, M.-H. Yoon, B. H. Hong, K. S. Novoselov, “Non-destructive electron microscopy imaging and analysis of biological samples with graphene coating” , *2D Mater.* **3**, 045004 (2016).

